Technische Universität Wien

Design, implementation and evaluation of algorithms for the analysis of pulse wave and ECG recordings in mice

MASTER THESIS

by

Irene López Campos

Registration number 11723235

under the supervision of

Univ.Lektor Dr.techn. Christopher Mayer

and

Ao.Univ.Prof. Dipl.Ing. Dr.techn. Eugenijus Kaniusas

Vienna, August 26, 2018

Technische Universität Wien

Entwurf, Implementierung und Evaluierung von Algorithmen zur Pulswellen- und EKG-analyse im Mausmodell

DIPLOMARBEIT

durch

Irene López Campos

Matrikelnummer 11723235

unter der Anleitung von

Univ.Lektor Dr.techn. Christopher Mayer

und

Ao.Univ.Prof. Dipl.Ing. Dr.techn. Eugenijus Kaniusas

Wien, August 26, 2018

Two heads are better than one, not because either is infallible, but because they are unlikely to go wrong in the same direction.

— C. S. Lewis

Acknowledgement

First of all I would like to thank Christopher Mayer, from the Austrian Institute of Technology, for giving me the chance of writing this thesis under his supervision. This thesis means a lot to me for two reasons. First, because it involves a topic I am very interested in, biosignals. And secondly, because it has given me the opportunity to spend more time in Vienna, and enjoy things that I will hardly forget, like cycling along beautiful streets, seeing the Danube frozen, discovering hidden heuriger in the middle of the vineyards, walking along the canal, learning climbing and getting to know better people from this incredible city.

Second of all, I want to express my sincere thanks to my supervisor Professor Eugenijus Kaniusas, for giving me the opportunity to write this thesis in cooperation with the Austrian Institute of Technology.

In addition, I would like to thank Nicole Di Lascio for collaborating with us and for always being willing to answer our questions. Without her contribution the development of this thesis would not have been possible.

I would like to thank as well everyone else I met at the AIT, especially my colleagues from the Biomedical Systems group, who helped me whenever I had questions and who made me feel one more of the team.

Thanks to my mother and father, for all your help and support to get here, and for teaching me to keep trying no matter what. For always trusting me.

Thanks to my grandparents, for always taking care of me and for teaching me so much about life.

To my friends, with whom I have learned to fight together and never give up. Thank you for being always there, for all the many shared experiences, and for teaching me that everything is always better in good company.

Finally, I want to thank my university, Escuela Técnica Superior de Ingenieros de Telecomunicación, to which I owe much of what I am today, and the Technische Universität Wien, for giving me the opportunity to come here and for let me discover a whole new world in biomedical engineering.

Statutory Declaration

I hereby declare that I have independently written the enclosed Master Thesis, that stated otherwise the work contained herein is my own and that collaborative contributions including tables, figures and ideas have been clearly marked and acknowledged.

Irene López Campos

Date

Abstract

Nowadays, mouse models and the analysis of murine biosignals are increasingly employed for the study and the comprehension of cardiovascular diseases (CVD). This master thesis involves the implementation and testing of algorithms in Matlab for the analysis of electrocardiograms (ECG) and pulse waves (PW), and its application to mice. Emphasis is put on approaches already used in cardiovascular research and their implementation.

In a first step, an analysis and a review of the state of the art in mouse models in cardiovascular research has been carried out, focusing on ECG and pulse wave recordings. Approaches have been selected jointly based on literature review and available data. Thereafter, algorithms have been implemented in order to automatically calculate different cardiovascular parameters. Furthermore, algorithms have been evaluated and applied to different groups of mice.

Four datasets of mice containing physiological and pulse wave information have been provided by the clinical partner from the University of Pisa, Department of Clinical and Experimental Medicine. This data cover 13 wild type male mice at the age of 8 and 25 weeks, 10 ApoE mice 16 weeks old, and 9 diabetes mice 13 weeks old. Mice were examined with a non-invasive high resolution ultrasound imaging system.

Implemented algorithms allow to apply four different analysis in order to compare cardiovascular parameters between two groups of mice. These analyses are: (1) a physiological comparison, (2) ECG intervals comparison, (3) wave intensity analysis (WIA) and (4) vascular analysis.

Three different test cases (TC) have been analyzed to test changes due to age (TC1), to study the influence of carotid plaque vulnerability (TC2) and to evaluate differences in various parameters caused by diabetes (TC3). Each test case consists of two different groups of mice. TC1 has been performed between young and old wild type (WT) mice. In TC2, young wild type and atherosclerosis mice have been compared. Lastly, TC3 has been performed between young wild type and diabetes mice.

Exemplarily, in TC1, parameters like W1 or reID are significantly higher in young WT mice than in old WT mice. On the contrary, AIx is higher in old WT mice. These results show that aging causes a reduction in the cardiac performance, indicated by the decrease in magnitude of the forward wave (W1) and the increase of the influence of reflected waves (AIx). Besides, the low distension capability of the artery (reID) in old WT mice shows that the carotid artery dilates with age. Furthermore, although pulse wave velocity (PWV) is similar between young and old WT mice, it increases in mice with atherosclerosis and diabetes. Thus, a connection between arterial stiffening and diabetes is most likely. This behaviour can as well be observed in humans.

In conclusion, this thesis presents an algorithm for the automatic identification of different cardiovascular parameters using murine signals achieved by non-invasive techniques. Despite some limitations, like a small sample size, results are promising and allow further investigations.

Key words — Mice, murine, mouse models, electrocardiogram, wave intensity analysis, pulse wave, pulse wave velocity, casdiovascular disease, blood pressure, augmentation index, heart beat, arterial stiffness.

Contents

List of Figures

List of Tables

Acronyms

μ artery wall thickness. 30

A cross-sectional area. 15, 56

Aβ amyloid β peptide. 49

AβPP amyloid-β precursor protein. 26, 51, 52, 57

AAA abdominal aortic aneurysm. 45, 56

aaPWV abdominal aorta PWV. 36

ACh acetylcholine. 38, 56

AD Alzheimer's disease. viii, 26, 49, 50, 52, 57

AIx augmentation index. iii, vii–ix, 15, 40, 44, 55, 66, 73–76, 98, 99, 108

ANGII angiotensin II. viii, 26, 42, 44, 45, 49–52, 55, 57

ANS autonomic nervous system. 18

AP augmentation pressure. 14

ApoE apolipoprotein E. vii–ix, xi, 24, 34–39, 42, 44–46, 53, 55, 56, 58–60, 76, 77, 87–89, 95–98, 104–109

AV atrioventricular. 7, 19, 55

B baseline coronary blood velocity. viii, 35, 46, 47, 56

BP blood pressure. 13, 35, 55

bpm beats per minute. 10, 18, 96

BW body weight. 47

C compliance. 14, 15

$CaCl_2$ calcium chloride. viii, 48, 57

CBF cerebral blood flow. viii, 42, 48, 52, 55, 57

cBP central blood pressure. 11

CCA common carotid artery. 9

cfPWV applanation tonometry–based carotid–femoral pulse wave velocity. viii, 16, 34, 36, 49, 57

CFR coronary flow reserve. 34, 35, 46, 47, 56

CHD coronary heart disease. 24

CMR cardiovascular magnetic resonance. 33–35, 45

CO cardiac output. 10, 53, 58

CVD cardiovascular disease. iii, 1, 16

D diameter. 10, 35, 55, 56, 70, 74, 75, 77

DBP diastolic blood pressure. 14, 35, 48, 56

Dd diastolic diameter diet. 53, 76

DES desmin protein. 25

dKO double knockout. 24, 39, 40, 55

Dm mean diameter. 53, 76

Ds systolic diameter diet. 53, 76

ECG electrocardiogram. iii, vii–ix, xi, 1, 2, 5, 17–20, 24, 28, 31, 55, 59, 60, 62, 65–67, 79, 80, 82, 83, 86, 87, 90, 91, 94–96, 103–105

ED ejection duration. 99

EDNO endothelial nitric oxide. 38, 56

EM eprosartan mesylate. 52, 57

eNOS endothelial nitric oxide synthase. 25, 36, 49

Fbn1 fibrillin-1. 25, 26

FC functional connectivity. 52, 57

H hyperemic coronary blood velocity. viii, 35, 46, 47, 56

hb heart beat. 103

HDL high density lipoprotein. 24

HFHS high-fat-high-sugar. viii, 47, 48, 56

HPF high pass filter. 67

HR heart rate. 10, 16, 18, 53, 55, 66, 68, 95, 96, 103

HT hypertension. 26, 49, 50, 55, 57

IQR interquartile range. 63

KO knockout. vii, viii, 23–25, 37–39, 44, 45

LDLR low density lipoprotein receptor. viii, 25, 44

lnD natural logarithm of diameter. 32, 34, 53, 69, 70, 106

LoA limits of agreement. 62

LPF low pass filter. 67, 68

LV left ventricle. 17, 40, 53, 97

MAP mean arterial blood pressure. vii, 14, 39, 42, 48, 55

MFS Marfan syndrome. viii, 25, 26, 51, 57

MGP matrix GLA protein. 25

MI myocardial infarction. 24, 55

mmHg millimeters of mercury. 13

MR magnetic resonance. 35, 46

MRI magnetic resonance imaging. 28, 33, 35, 52, 53, 56–58

NA negative area. 17, 53, 58, 97

NaCl sodium chloride. 57

ND normal diet. viii, 47, 48, 56

NO nitric oxide. 25, 37–39, 55

OCT optical coherence tomography. 48, 57

$\mathbf{P}_e$ external pressure. 30

$\mathbf{P}_i$ internal pressure. 30

$\mathbf{P}_t$ transmural pressure. 30

PA arterial pressure. 10

PC phase contrast. 34, 56

PE phenylephrine. vii, 38, 39

PE phenylephrine. 55

PP pulse pressure. 14–16, 23, 40, 48, 55, 56, 73

PS1 presenilin-1. 26, 52

PV venous pressure. 10

PW pulse wave. iii, 11, 34, 59

PWV pulse wave velocity. iii, vii–ix, xi, 10, 11, 16, 23, 27–39, 41, 45–47, 49–51, 53, 55–58, 65, 69–72, 79–81, 83, 91, 96–99, 106, 107

Q blood volume flow. 9, 10

QA flow-area. 28, 31, 33–36, 53, 56, 58

R flow resistance. 10

r artery radius. 30

reID relative distension. iii, 53, 76, 97

RI reflection index. 17, 53, 58, 97

RR respiration rate. 68, 96

S/D systolic-to-diastolic ratio. viii, 47, 56, 74

SA sinoatrial. 7, 19

SBP systolic blood pressure. viii, 13, 35, 48–50, 55–57

SD standard deviation. 62

SMA smooth muscle actin. viii, 24, 42, 45, 55, 99

SNS sympathetic nervous system. 18

SR-BI scavenger receptor class B type I. 24

SV stroke volume. 10, 15

T artery wall tension. 30

TAC transverse aortic constriction. viii, 35, 46, 47, 56

tBP tail-cuff blood pressure. 33

TC test case. iii, 60

TT transit time. 31, 33, 35, 51, 53, 55, 56, 58

US ultrasound. 28, 34–36, 53, 55, 57–59

V blood flow velocity. 10, 32, 34, 35, 53, 55, 56, 69, 70, 106

V_p velocity peak. 53, 58, 76, 97

W1 first positive WIA peak. iii, 17, 53, 58, 72, 97

W2 second WIA positive peak. 17, 53, 58, 72, 97

Wb negative WIA peak. 17, 53, 58, 72, 97, 98

WI wave intensity. 16, 34, 56, 65

WIA wave intensity analysis. iii, xi, 2, 16, 17, 34, 53, 54, 58, 59, 65, 71, 72

WT wild type. iii, vii, viii, 24, 32, 35, 36, 38, 42, 43, 45, 46, 49–53, 55–60, 82, 98

$\mathbf{Z}_C$ characteristic impedance. 14, 31, 41, 55

$\mathbf{Z}_i$ input impedance. 15, 55

CHAPTER 1

Introduction

In this chapter, the motivation and goals of this thesis are briefly introduced. Furthermore, the structure of the thesis is presented.

1.1 Motivation

Cardiovascular and circulatory diseases are recognized as the leading causes of death in the world [1]. Arterial stiffness is an independent marker of cardiovascular disease (CVD) in both healthy and diseased populations. It is caused by the degenerative process affecting the extracellular matrix of elastic arteries, that become narrowed and hardened [2].

Hemodynamic changes in large and medium sized arteries caused by increased arterial stiffness, like early arrival in systole of reflected waves [3], serve as early indicators of cardiovascular diseases. Pulse pressure, pulse wave velocity and the augmentation index are the most common surrogate measures of arterial stiffness [3].

Transgenic and gene-targeted models of mice are commonly used to study cardiovascular disease processes due to their anatomical and physiological similarities with humans. Dissimilarities found between both species are small, for example, concerning heart rate or the ECG shape. Besides, magnitudes and waveforms of blood velocities from both cardiac and peripheral sites are similar in mice and humans [4]. In adition, pressure waveforms in mice are almost indistinguishable from humans' signals recorded at similar sites [5]. Therefore, it is possible to use results obtained in mice to draw conclusions for humans.

In general, cardiovascular parameters are used for assessing the cardiovascular health. This can contribute to the understanding and prevention of cardiovascular diseases which can lead to heart failure. However, the determination of these parameters is not straightforward. Thus, algorithms for their automatic identification are needed.

Wave intensity analysis (WIA), for example, can provide information about the interaction between the vascular and the cardiac system [6]. It is a technique based on the decomposition of the pulse wave into its forward and reflected wave components [7]. Thus, the interaction between the left ventricle work and the mechanical properties of the vascular system is represented by parameters derived from wave intensity analysis [6].

1.2 Aim of the Thesis

The aim of this master thesis is the implementation and testing of algorithms for the analysis of physiological measures as well as parameters derived from ECG, wave intensity, blood flow and diameter signals, and its application to murine signals. Diameter signal from US images were used as non-invasive surrogate for the pulse waves due to their similarity in morphology. Emphasis is put on approaches already used in cardiovascular research which assess biomarkers of cardiovascular risk by means of non-invasive techniques.

Thus, first, the state of the art in mouse models in cardiovascular research is exhaustively analyzed, focusing on ECG and pulse wave recordings. Based thereupon, promising approaches are selected for the implementation of the algorithms.

After their implementation, algorithms are applied to different mice. In particular, four datasets are used in this thesis corresponding to: wild type mice, measured at young and old age, atherosclerosis mice and diabetes mice. Results obtained are compared to values obtained by external methods to validate the implemented algorithms.

Thereafter, three test cases have been analyzed. The first test case is performed between young and old wild type mice to test changes due to age. To study the influence of carotid plaque vulnerability, a second test case compares young wild type mice with atherosclerosis mice. In the third test case, differences in various parameters between young wild type mice and diabetes mice are evaluated to see the influence of this disease.

Lastly, correlations between results and similarities with reported results from literature are discussed and conclusions are drawn.

1.3 Structure of the Thesis

This thesis is composed of six chapters. The first one is an introduction where motivation and the aim of the thesis are presented. Chapter 2 consists of the background needed for understanding the presented work: a short description of the cardiovascular system, the hemodynamic parameters mentioned in this thesis as well as the basics of the electrocardiogram. Chapter 3 introduces the mouse models, techniques and methods commonly used in cardiovascular research

as well as their evolution during the last two decades. In chapter 4, the state of the art regarding mice in cardiovascular research is presented.

The following chapters refer to the technical part of this thesis. In chapter 5, data, test cases and external methods are described, while in chapter 6, the implemented methods are explained in detail. Thereafter, in chapter 7, results of the validation of the algorithms and of the test cases are presented. Chapter 8 includes the interpretation of the results (discussion) and possible future lines of work in the outlook section. Finally, the thesis is completed by the appendices and an exhaustive bibliography.

CHAPTER 2

Background

In the following chapter, an overview of the necessary basic knowledge is established. It is divided in different sections comprising a summary of the heart and the cardiovascular system as well as some hemodynamic parameters. These parameters cover the hemodynamic ones for the assessment of the cardiovascular system and ECG ones for the assessment of the cardiac function.

2.1 The Cardiovascular System

The cardiovascular system consists of the heart and different blood vessels like arteries, veins, and capillaries. Throughout this section, general concepts about the cardiovascular system will be decribed, starting with the anatomy of the heart, specifying similarities and differences between human and mouse anatomy. Further explanations can be found in [8] and [9].

2.1.1 Heart

The heart is an organ that pumps blood throughout the body, supplying oxygen and nutrients to the tissues and removing carbon dioxide and other wastes. The anatomy of the heart consists of a left and right side separated by a wall of muscle called the septum (figure 2.1). Each side has two chambers, the atrium and the ventricle. These compartments are separated by atrioventricular valves: the tricuspid valve on the right side, and the mitral valve on the left side. The semilunar valves, at the bases of the aorta and the pulmonary artery, are the interconnection between the ventricles and the attached blood vessels. The pulmonary valve is allocated between the right ventricle and the pulmonary artery. The aortic valve regulates the blood flow between the left ventricle and the aorta. Pressure differences govern the opening and closing of the valves.

The muscular structure of the heart is formed by two distinct cardiac muscles, called myocardia.

Both, atria and ventricles, are each built by one myocardium leading to a functional separation. The inner tissue layer of the heart is called endocardium, the outer layer epicardium. Special conducting tissue connects electrically the atrium and the ventricle. Only minor differences concerning the heart anatomy are found in veins and atrial morphology between both species [10, 11]. Figures 2.1 and 2.2 show a schematic representation of the human and murine heart and the connected blood vessels.

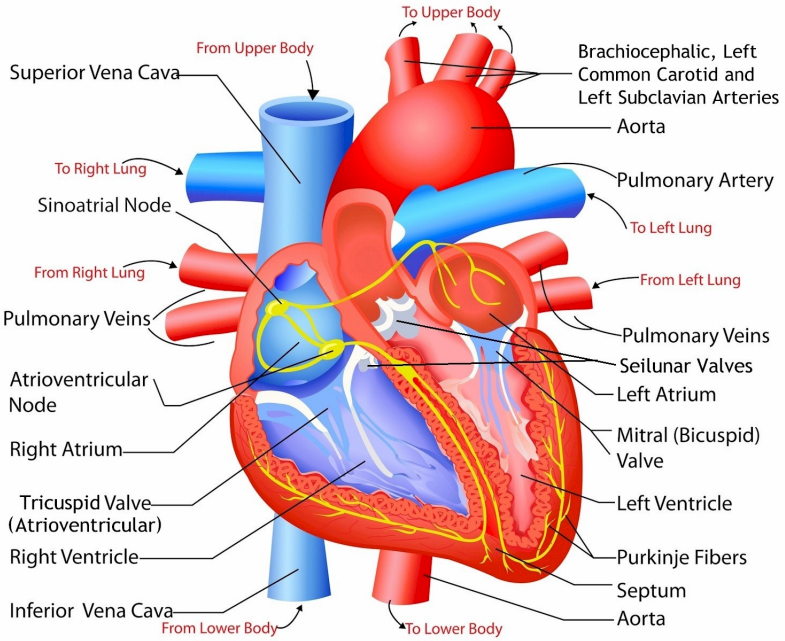

Figure 2.1: *Schematic representation of the human heart and the connected blood vessels. Adapted from [12].*

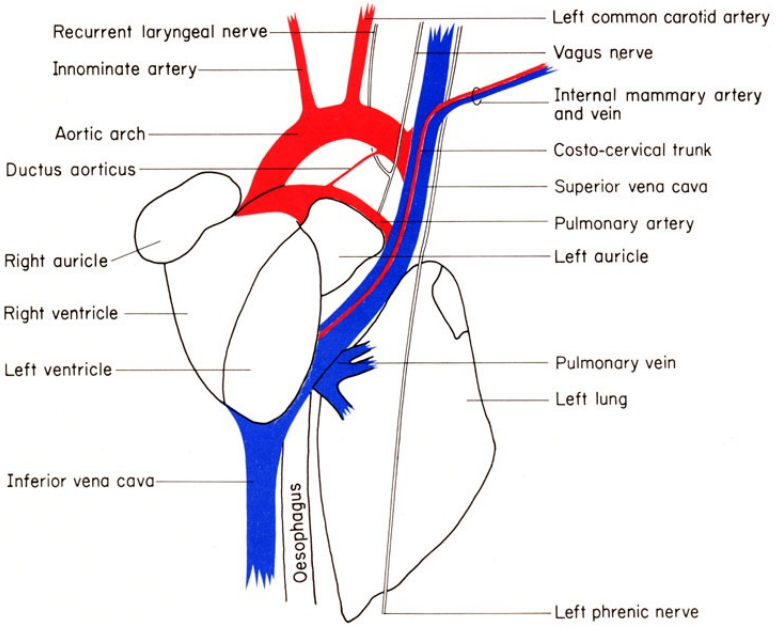

Figure 2.2: *Schematic representation of the murine heart and the connected blood vessels [13].*

In contrast to humans, which present separate pulmonary vein orifices, in mice a pulmonary venous confluence with one orifice enters the left atrium. Besides, in mice the left and right

superior caval veins drain into the sinus venosus, which opens into the right atrium. In humans, on the contrary, both the superior vena cava and the inferior vena cava empty into the right atrium [14].

There are two types of circulation of blood. The pulmonary circulation describes the blood flow from the right ventricle, through the lungs, to the left atrium. Its purpose is the transport of blood with low oxygen and high carbon dioxide concentration to the lungs for oxygenation. The systemic circulation, on the other side, comprises the delivering of oxygenated blood from the left ventricle, through the arteries, to the capillaries. From the tissue capillaries in the body, the deoxygenated blood returns to the right atrium of the heart through a system of veins (figure 2.3).

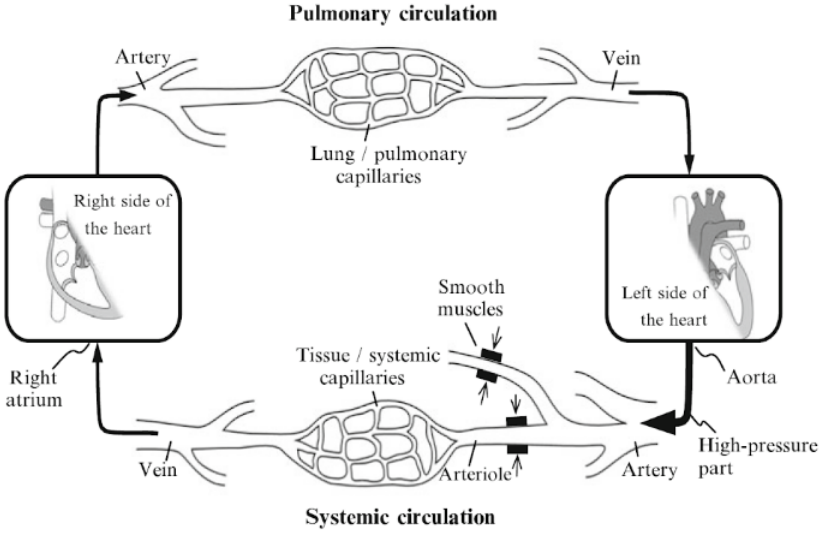

Figure 2.3: *Systemic and pulmonary loop circulation. The thickness of the arrows represents the blood pressure level [8].*

The electrical conduction system is responsible for the contraction of the heart muscle. There are three components acting as pacemakers for the heart at different rates: the sinoatrial (SA) node, the atrioventricular (AV) node and the bundle of His. The primary pacemaker is the SA node. It is a collection of specialized cardiac muscle cells, continuously producing action potentials, setting the rhythm of the heart. In humans, the SA is located in the right atrium. However, in mice it is located in the superior vena cava above the junction with the atrium [15]. The only conducting part between atria and ventricles is the AV node, in the region of the interatrial septum. The electrical signals travel from the AV node through the left and right bundle of His to the respective Purkinje fibers, and finally reach the ventricular epicardium. The connection from the AV node to the bundle branches is similar in both species [15].

The action potential initiated in the SA node stimulates both atria to contract. When the atrial pressure exceeds the ventricular pressure, the atrioventricular valves open. The semilunar valves keep closed while the deoxygenated blood enters the right ventricle and the oxygenated blood the left ventricle. When the ventricles contract, the ventricular pressure increases and, when

it exceeds the pressure of the following arteries, the semilunar valves open. Thus, the blood is pressed from the heart into the arterial vessels. When the ventricular heart muscle begins to relax, the semilunar valves close.

2.1.2 Arterial Tree

An artery is an elastic blood vessel transporting blood away from the heart. There are two main types of arteries: pulmonary arteries and systemic arteries. Pulmonary arteries carry blood from the heart to the lungs where the blood picks up oxygen. This blood returns to the heart via the pulmonary veins. Systemic arteries deliver blood to the rest of the body [16].

The aorta is the main systemic artery and the largest of the body. It starts from the left ventricle at the aortic valve and then curves in the aortic arch, giving off branches to the heart, head, and upper limbs. Later on, it goes down through the diaphragm to the abdomen and divides into the iliac vessels [17]. Major arteries in human are illustrated in figure 2.4.

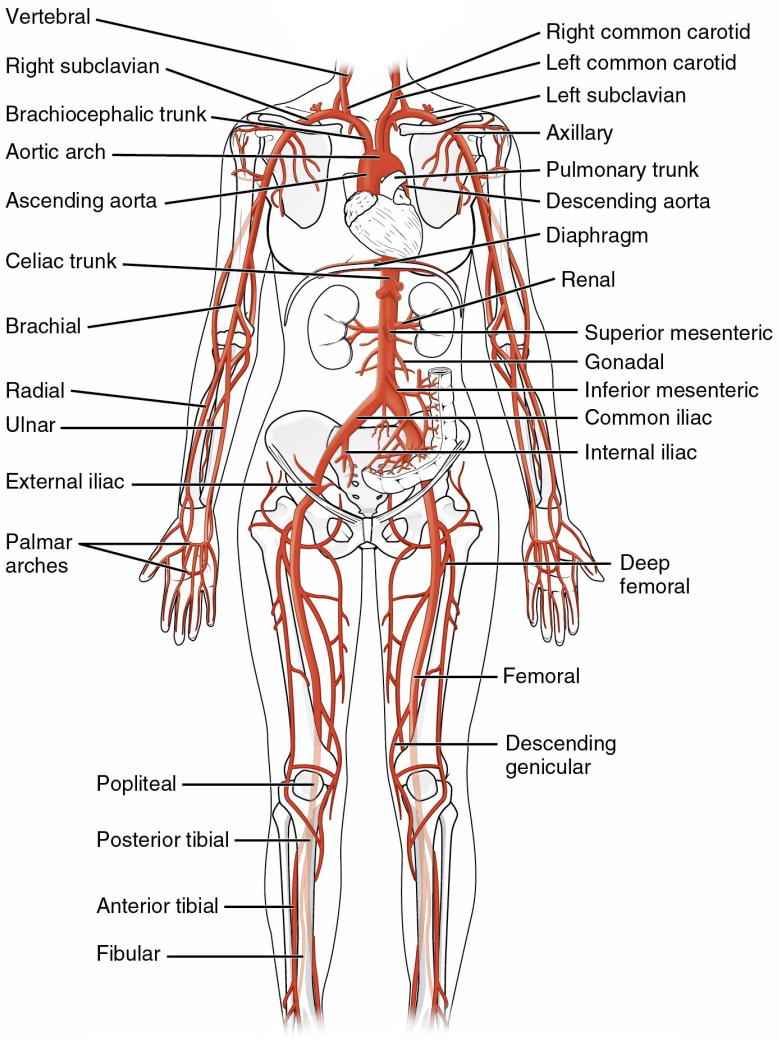

Figure 2.4: *Major arteries in the human body. Diagram adapted from [18].*

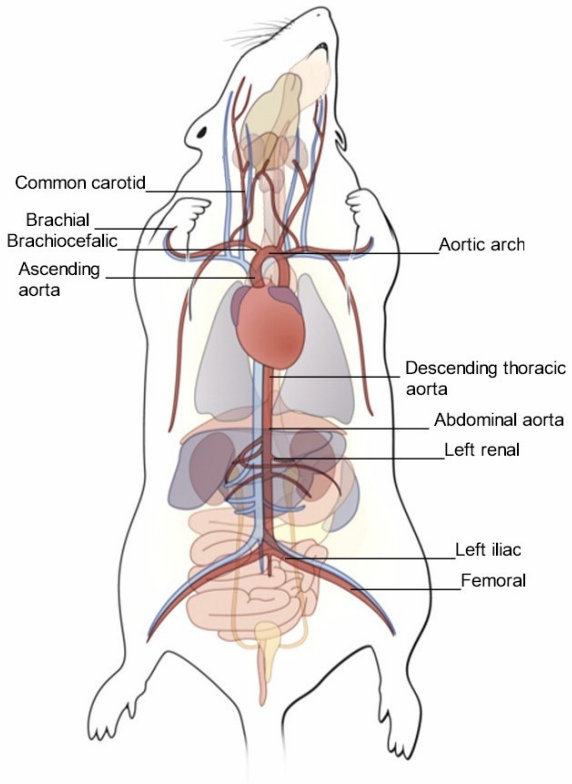

Figure 2.5: *Major branches of the murine arterial tree (adapted from [19]).*

In humans, as well as in mice, there are four main sections in the aorta: the ascending aorta, the aortic arch, the thoracic (descending) aorta and the abdominal aorta. There are three major branches arising from the aortic arch: the brachiocephalic trunk, the left common carotid artery and the left subclavian artery. The brachiocephalic trunk, which suplies the right side of the head and the right upper limb, splits into the right common carotid and right subclavian arteries. The left common carotid artery supplies the left side of the head and neck, and the left subclavian artery the left upper limb [16]. Regarding the arterial system, there are no big differences between human and mice. Main similarities are found in the anatomy of the aortic arches, their vascular branching pattern, and the geometry of the branches [20, 21], as one can obverse comparing figure 2.4 and figure 2.5.

2.1.3 Blood Flow and Velocity

Blood flow (blood volume flow (Q)) refers to the movement of blood through a vessel, tissue, or organ, and is usually expressed in terms of volume of blood, in liters per minute (l/min) [22].

Commonly, the blood flow behaviour can be described by a main forward wave and its reflection. The example in figure 2.6 illustrates the blood flow (in orange) measured at the common carotid artery (CCA), situated in the neck of the subject. The forward wave, in purple, corresponds to the flow from the heart to peripheral vessels. Reflected waves come from the thorax, arm and head towards the heart, in blue, green and red, respectively. As one can see, waves from the thorax and the arm exert a

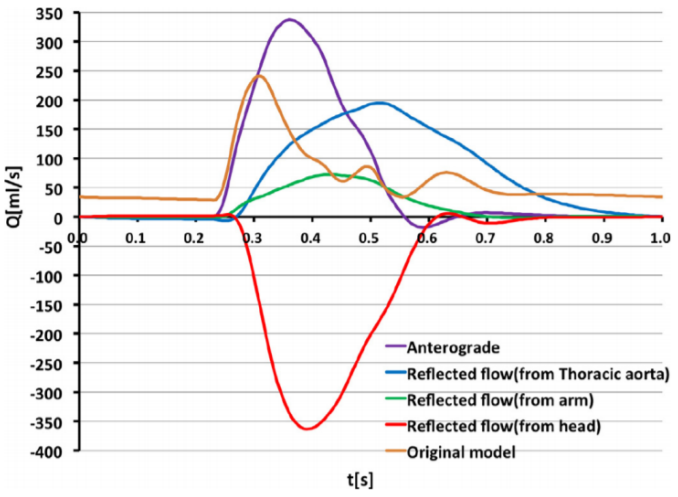

Figure 2.6: *Common carotid artery flow rate waveform in human [23].*

force in the opposite direction of the blood flow, i.e. a resistance to flow, while reflected waves from the head add to the forward wave [23].

The cardiac output CO is the blood flow through the heart. It describes the amount of blood that the heart pumps from each ventricle per minute and it is usually expressed as HR x SV. (HR) is the heart rate, i.e. the number of beats or contractions of the heart per minute (bpm) (see section 2.4.1). The stroke volume (SV) is the amount of blood pumped by the left ventricle of the heart in one contraction. Normally, only about two-thirds of the blood in the ventricle is expelled with each beat [22, 24].

Based on Ohm's Law, Q can also be defined as the relationship between the change in pressure (ΔP) and the resistance to flow (R) offered by the blood vessel. In a blood vessel, ΔP is the pressure difference between any two points along a given length of the vessel. For the blood flow across a heart valve, ΔP is the pressure difference between the two pressures on either side of the valve. For the aortic valve, for example, the pressure difference that drives flow across that valve during ventricular ejection is the intraventricular pressure minus the aortic pressure. In the case of an organ, the pressure difference is generally expressed as the difference between the arterial pressure (PA) and venous pressure (PV) [24].

Blood flow velocity or simply blood velocity (V) is determined by measuring the distance that the blood travels per unit of time, in meters per second (m/s), and is usually calculated from the Doppler shift frequency (Δ_f) using the Doppler equation:

$$V = c * \Delta_f / (2 f_0 * cos(\Theta)) \tag{2.1}$$

where c is the speed of sound in blood (1,500 m/s) and f_0 is the ultrasonic frequency used, 10 or 20 MHz normally [25].

Blood velocity is commonly used together with the diameter (diameter (D)) of the vessels or the pressure to calculate the pulse wave velocity (PWV). Blood velocity can also be described by a forward and a backward component. A good representation of V and its components is shown in section 4, figure 4.16.

2.1.4 Pulse Wave

During systole, the phase of contraction of the heart, blood is ejected from ventricles. The left ventricle contraction causes the blood to move into the aorta, generating a pulse wave travelling through the vessels of the circulatory system and being reflected at bifurcations or discontinuities of the arterial wall, propagating back to the heart. Reflections in the aortic valve and waves reflected inside the ventricle can also be responsible of changes in the pressure wave [26].

If no reflections existed, the shape of pressure and flow waveforms would be identical, travel at

the same velocity and be related by the characteristic impedance of the vessel. However, blood pressure is measured as the sum of forward and backward pressure waves, while the flow is the difference between them. The pressure in the aorta, shown in figure 2.7, is known as central blood pressure (cBP) [16, 27].

The measurement of the pulse wave (PW) describes both, the shape and the speed of the wave, related to the stiffness of the arteries [28]. Pressure rises rapidly in the ventricle at the beginning of systole. When it exceeds the pressure in the aorta, the aortic valve opens and blood is ejected, after what aortic pressure increases. About half way through ejection, there is a notch on the aortic pressure record (the dicrotic notch) which marks the closure of the aortic valve, followed by a fast decrease in ventricular pressure as the heart muscle relaxes. The pressure in the aorta falls much slower. This is because large central arteries, and particularly the aorta, are elastic, and thus act as a reservoir during systole, which is known as windkessel effect, storing some of the ejected blood which is then forced out into the peripheral vessels during diastole [16].

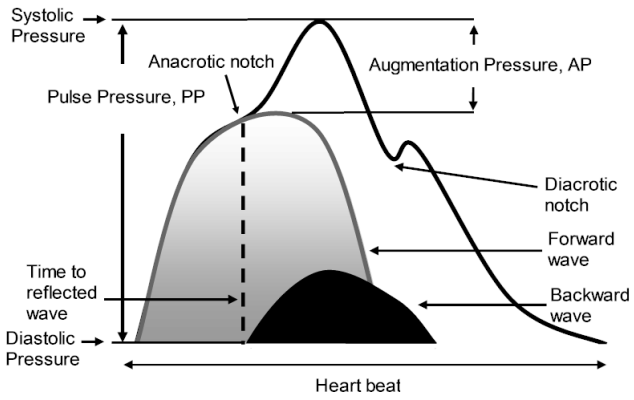

Figure 2.7: *Central pressure waveform (black line). Adapted from [29].*

Since reflections predominate at the sites of arteriolar bifurcations, pressure waveforms increase at points progressively further from the heart. On the contrary, blood flow velocity decreases in peripheral vessels since the reflected wave together with the smaller diameter of the vessels results in an increase of the resistance to flow [16]. This behaviour is shown in figure 2.8.

With age, or due to changes in the arterial wall, vessels become stiffer and the speed at which the pressure wave moves through the system is increased [27]. In young subjects, the reflected waves arrive at the aortic root during diastole. High arterial stiffness results in an increase in PWV, and causes the early arrival of the reflected waves during systolic ejection, rising the systolic blood pressure and widening pulse pressure, as ilustrated in figure 2.9. Thus, the augmentation of the wave also increases [30]. When the pressure waves move faster through the arteries, the reflected waves will also move back quicker [29].

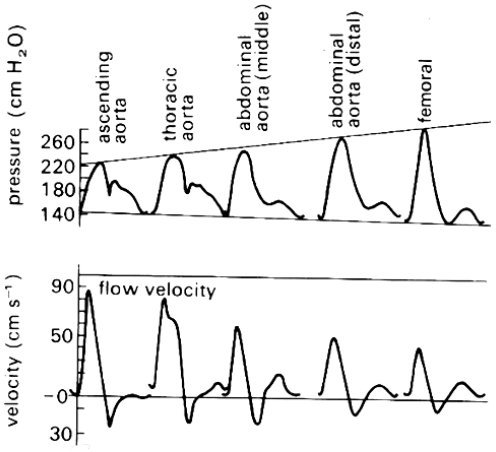

Figure 2.8: *Pressure and flow velocity records along the aorta. Adapted from [17].*

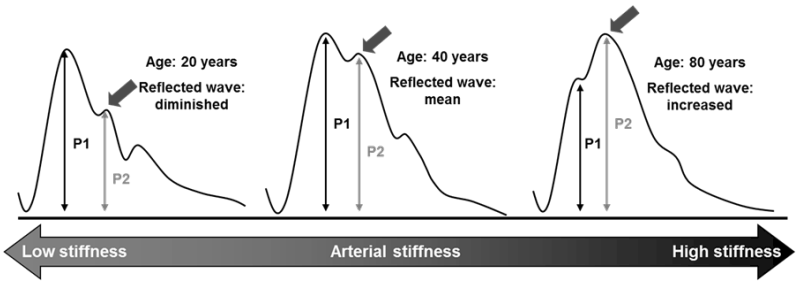

Figure 2.9: *Pressure and flow velocity records at different sites along the aorta. Adapted from [17]).*

2.1.5 Arterial Stiffness

Arterial stiffening is the root cause of a range of cardiovascular complications, including myocardial infarction, left ventricular hypertrophy, stroke, renal failure, dementia, and death, and a hallmark of the aging process. It causes early arrival of wave reflections in systole instead of diastole and, thus, increases systolic afterload and reduces diastolic coronary perfusion pressure [31]. Early arrival of reflected waves causes early aortic valve closure and reduced cardiac output, ending in heart failure [32]. Moreover, as arterial stiffening usually involves mainly the proximal arteries, the stiffness gradient between proximal elastic arteries and more distal muscular arteries decreases [33]. This phenomenon may result in a diminution of the amplitude of wave reflection from the resistance vessels, and consequently, in an increased transmission of pressure to the microcirculation, potentially dangerous for brain and kidney [4].

Arterial stiffness results from a degenerative process affecting mainly the extracellular matrix of elastic arteries [2]. The arteries become narrowed and hardened due to the aggregation of plaque around the artery wall. This accumulation of fats, cholesterol and other substances in the artery walls (plaques) can restrict blood flow. Atherosclerosis is a specific type of arteriosclerosis, a vascular disease that occurs when the blood arteries carrying oxygen and nutrients from the heart to the rest of the body become thick and stiff, sometimes restricting blood flow to organs and tissues. It is related to high blood pressure or hypertension. Although atherosclerosis is often considered a heart problem, it can affect arteries anywhere in the body, since some plaques can burst, triggering a blood clot [34].

When a vessel is blocked or obstructed, aneurysms can appear as bulges filled with blood before the obstruction. Some common aneurysms are aortic and cerebral aneurysms. If one of them bursts, it can result in brain damage. A stroke occurs when blood supply to the brain is disrupted. It usually happens when a blood clot blocks one of the veins in the brain. Without oxygen, brain cells begin to die, and cognitive functions in that specific area of the brain can be compromised, which could include motor control, memory, language, etc. Strokes by a blood clot are called ischemic attacks. Another type of stroke is caused by blood flowing out of the veins uncontrollably (hemorrhagic). Although aneurysms can have a genetic component the direct causes are the hardening of the arteries (atherosclerosis) and aging.

Arterial stiffness is generally considered an independent predictor of cardiovascular and cerebrovascular diseases [35]. In recent years, it has been demonstrated that parameters as pulse wave velocity (section 2.2.6), used to quantify arterial stiffness, can predict a poor cognitive performance and a steeper cognitive decline [36]. However, the relationship between cognitive impairment and other parameters as pulse pressure remains controversial [37], since some studies have found that pulse pressure could not predict declines in working memory, power of attention and continuity of attention.

Cerebral small vessel disease, the most common vascular cause of dementia, presents a risk for cerebrovascular disease and cognitive impairment due to arterial stiffness, presented as microvessel arteriosclerosis with vascular endothelial dysfunction [38]. In 2001, the group of Roher et al., from the center for molecular biology and genetics in sun city (Arizona), reported that vascular narrowing due to atherosclerosis of the circle of Willis is greater in Alzheimer's patients than in non-demented controls [39]. Atherosclerotic lesions of cerebral blood vessels constitute a major feature of Alzheimer's neuropathology, perhaps, as prominent as amyloid plaques or neurofibrillary tangles, the traditional pathological hallmarks of the disease [40].

2.2 Hemodynamic Parameters

Hemodynamics is an important part of cardiovascular physiology dealing with the forces the heart uses to circulate blood through the cardiovascular system. Most of the cardiovascular diseases are related to systemic hemodynamic dysfunction [24]. In the following, hemodynamic parameters to describe the cardiovascular system are introduced.

2.2.1 Blood Pressure

The force with which blood pushes against artery walls as it flows throughout the body is known as blood pressure (BP) and is normally expressed as two numbers (i.e. minimum and maximum) measured in millimeters of mercury (millimeters of mercury (mmHg)). Although less commonly used, it can also be expressed in centimetre of water (cm H_2O), being 1 cm H_2O = 0.736 mmHg. The two numbers correspond to the systolic pressure and the diastolic pressure [22, 24]. The accurate determination of arterial pressure is important for studying pathological conditions such as hypertension, as well as for determining the effects of pharmacological intervention.

Systolic and diastolic blood pressure

In the top of the figure of the pressure waveform (figure 2.7), the maximum blood pressure corresponds to the squeezing of the heart pushing the blood around the body. It is called systolic blood pressure (systolic blood pressure (SBP)). In humans, a normal SBP is 120 mmHg or below.

At the minimum, the diastolic blood pressure (diastolic blood pressure (DBP)) indicates the pressure in the arteries when the heart rests between beats. A normal diastolic blood pressure is 80 mmHg or less in humans. Both parameters are similar to those found in mice [41]. The murine blood pressure response to a variety of vasoactive drugs and is qualitatively similar to that in humans, another reason to use this animals as models of human diseases related to blood pressure [42].

Pulse Pressure

Pulse pressure (PP) is the difference between the systolic and diastolic pressure readings. It is also normally measured in millimeters of mercury. It represents the force that the heart generates each time it contracts. During the systole, the pressure exerted on the walls of the blood vessels or arteries is lower if the blood vessels are of high compliance or low stiffness [43].

Mean Arterial Pressure

Mean arterial blood pressure (MAP) represents the average force driving blood from arteries into vessels that serve the tissues. It can, for example, be approximated by adding the diastolic pressure to one-third of the pulse pressure or systolic pressure minus the diastolic pressure [43]:

$$MAP = P_D + \frac{P_S - P_D}{3} \tag{2.2}$$

Augmentation Pressure

The augmentation pressure (AP) is the increase in pressure due to backward components. It is measured from the inflection point or anacrotic notch, in the pulse wave, till the systolic pressure, see figure 2.7 in section 2.1.4.

2.2.2 Vascular Impedance

The blood pressure and flow pulsations propagate as waves through the arterial tree. Thus, the arterial tree can be considered as a transmission line model, since waves are reflected at transitions in arterial geometry and elasticity [44]. According to the electrical transmission line theory, the relationship between voltage and current gives the impedance. Similarly, to calculate the vascular impedance, pulse pressure is considered as voltage and blood flow as current [44].

Input impedance (Z_i) is defined as the ratio of the pulsatile components of pressure and flow [45]. This parameter is not restricted to unidirectional waves. Thus, it is a complex number which includes the influence of reflected waves. It allows characterizing the wave transmission

and reflection properties in a blood vessel in the frequency domain as follows [45]:

$$Z_i = \frac{P(w)}{Q(w)} \tag{2.3}$$

Characteristic impedance (Z_C), also known as aortic impedance, is calculated as the ratio of the forward propagating pressure and the forward propagating flow in a certain instance of time in the absence of reflections [22]. Thus, it represents a local characteristic property of the vessel wall [45]. This parameter varies within the contraction cycle and it increases with peripheral vasoconstriction while decreases with aortic compliance (C) [46]. Under certain simplifying assumptions, characteristic impedance can be approximated as the following real number:

$$Z_c = \frac{\rho \cdot c}{A} \tag{2.4}$$

where c represents the wave speed, ρ the fluid density, and A the cross-sectional area of the vessel.

2.2.3 Peripheral Resistance

The peripheral resistance is the effect of the vessels resisting flow. It is primarily a function of vessel diameter, so it is dependent on both the cross-sectional area (A) and the elasticity of the arterial segment. As the arteries constrict, the resistance increases and as they dilate, resistance decreases. It is determined by autonomic activity (sympathetic activity constricts peripheral arteries), pharmacologic agents (vasoconstrictor versus vasodilator drugs) and blood viscosity (high viscosity increases resistance) [47].

2.2.4 Compliance

The systemic compliance (C) is the compliance of the heart and large arteries, a parameter developed to assess the elasticity or rigidity of the heart and arteries, measured as the change in volume of the heart (SV) divided by the change in pressure within the heart, the pulse pressure (PP) [ml/mmHg] [22].

Arterial compliance mostly depends on arterial intrinsic elastic properties, and is a determinant of the propagation speed of the pulse pressure wave. Decreased arterial compliance is responsible for both, an increase in the incident pressure wave and the higher effect of reflected pressure waves. This increases systolic pressure and ventricular afterload, and generates left ventricular hypertrophy [48].

2.2.5 Augmentation Index

The augmentation index (AIx) is a parameter of arterial stiffness. It is a measure of wave reflection describing the amount of pressure added to the systolic pressure peak based on the reflected wave. Dividing the augmentation pressure by the pulse pressure gives the AIx. The greater the reflected wave, the higher the augmentation index (AIx). This parameter increases with the advance of age [29, 49].

2.2.6 Pulse Wave Velocity

Pulse wave velocity (PWV) is the standard clinical surrogate for regional arterial stiffness and predicts CVD [50]. It represents the speed with which the pulse wave travels down the vessels through the circulatory system. PWV can be used as an indicator of structural changes of the aorta and large vessels, since it increases with increasing arterial stiffness. Clinically, carotid–femoral PWV (cfPWV) is considered the gold standard for the assessment of central arterial stiffness and a surrogate marker for cardiovascular morbidity and mortality, independent of atherosclerosis or brachial blood pressure [51].

Together with pulse pressure (PP), pulse wave velocity (PWV) is one of the main markers of cardiovascular risk. It can be measured directly, as a ratio of distance between two measurement points divided by the time required for the pulse wave to travel this distance [2] and is typically performed non-invasively using ultrasound [25, 52, 53].

Some cardiovascular risk factors, such as age and blood pressure, are known to have a strong association with PWV. However, the association between heart rate (HR) and PWV has always been controversial. Experimental investigations have established that the stiffness of large arteries has a dependency on acute heart rate changes [54]. HR may be an important confounding factor in PWV measurements and, thus, should be incorporated when analyzing PWV to measure arterial stiffness [55].

The stiffer the vessel, the faster the pulse wave moves along the aorta. Thus, PWV is an accepted parameter for estimating elasticity and compliance of large vessels in humans [56], nonhuman primates [57], dogs [58], rabbits [59], rats [60] and mice [25].

2.3 Wave Intensity Analysis

Wave intensity analysis (WIA) is a technique developed by Parker and Jones (1990), based on the decomposition of pulsatile flow into its wave components to study the cardiovascular dynamics [7]. It is considered an alternative to the traditional Fourier methods of analysis commonly used in this field. The net wave intensity (WI) measures the flux of energy per unit area carried by

the wavefronts from the heart throughout the arterial tree [7].

Using the local PWV value, WIA can identify forward waves originating from the heart and backward waves arising from the peripheral vasculature, by analysing the compression and expansion of the vessels due to changes in pressure and flow velocity [6]. Forward and backward waves are identified by positive and negative WI values respectively. Traditionally, the wave intensity signal has been obtained using invasive techniques [61].

The shape of the WI signal is usually characterized by three peaks, as shown in figure 2.10, where WIA has been performed in the carotid artery of a mouse. The first positive and predominant peak (W1) corresponds to the fordward compresion wave. It is produced by the simultaneous increase of pressure and flow velocity as a consequence of left ventricle (LV) ejection that occurs in early systole [62]. This peak is followed by a smaller negative one (Wb, local minimum) which represents a backward compression wave generated by the reflection of the forward compression front from distal points. At the end of the systolic phase, a second smaller positive peak occurs (W2, second local maxima), which reflects a forward expansion wave, generated by a simultaneous decrease of pressure and flow velocity.

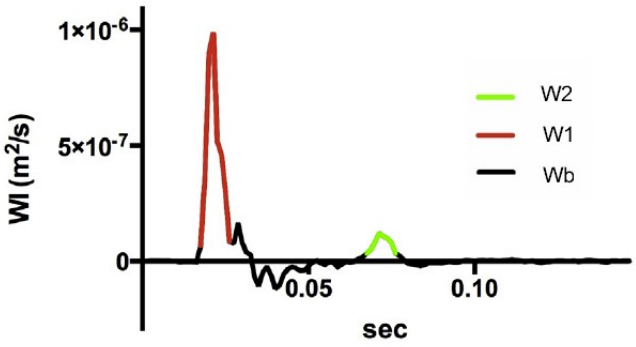

Figure 2.10: *WIA performed in mice. Adapted from [63].*

Once the wave intensity signal has been calculated, other WIA-derived parameters can be determined. These parameters are the negative area (NA) and the reflection index (RI). The negative area, delimited by negative intensity values, indicates the effects of reflected waves. The reflection index, the ratio between the backward WIA peak and the forward peak (Wb/W1), allows to predict cardiovascular events [6].

2.4 Electrocardiogram

The electrocardiogram (ECG) is used in clinical practice as a reliable, accessible and inexpensive method to detect certain cardiac abnormalities. This electrophysiological monitoring method allows recording of electrical signals or action potentials, triggered by temporal ionic flow across the membrane of excitable cells. These signals transport physiological information within the body related to the cardiac contractions. The depolarization or activation of one cell leads to

the excitation of the adjacent cells. The resulting wave front propagates through the heart. The orientation of the resulting dipole follows the direction of the depolarization propagation. Repolarization or relaxation occurs as soon as the action potential is over [8].

Resulting potential differences are recorded by placing electrodes on the body surface. For humans, the Einthoven leads I, II, III are measured using electrodes on the right arm, the left arm and the left foot. Similarly, in mice, the three limb electrodes are usually placed in the left and right armpit and the left groin [64]. Commonly, the representation of the heart's electrical activity uses the standard 12-lead ECG system, where a lead represents a particular orientation in space. It is based on the three Einthoven leads, the three Goldberg leads and the Wilson leads V1 - V6 [8]. A more detailed explanation can be found in [9].

2.4.1 Heart Rate

The ECG signal can be used for the estimation of the cardiac contractions' frequency. This parameter is known as heart rate (HR) and is measured in beats per minute (bpm). The normal HR in mice is between 500 to 600 bpm [65, 66], between 260 and 450 bpm in rats [67], and between 60 and 100 bpm in humans [68]. It is regulated by the autonomic nervous system (ANS). The sympathetic nervous system (SNS) releases the hormones (catecholamines: epinephrine and norepinephrine) to accelerate the heart rate. On the other hand, the parasympathetic nervous system (PNS) releases the hormone acetylcholine to slow down the heart rate. Factors such as stress, caffeine, and excitement may temporarily accelerate your heart rate, while meditating or taking slow, deep breaths may help to slow your heart rate down [69].

2.4.2 ECG Intervals

On the ECG signal, different deflections are recorded as a series of positive and negative waves. In the human ECG (see figure 2.11.a), the first deflection of the heart beat is the small upward P-wave. It indicates atrial depolarisation. A fraction of a second after the P-wave begins, the atria contracts. When visible, the Q-wave is any initial downward deflection after the P-wave. In general, the QRS-complex reflects the depolarization of the ventricles. The normal Q-wave represents septal depolarisation. On a standard electrocardiogram (ECG), the maximum upwards deflection of a normal QRS-complex is at the peak of the R-wave, which represents early ventricular depolarisation. The T-wave represents repolarisation of the ventricles [8, 70].

Some of these ECG parameters can be associated with cardiovascular mortality in particular conditions. These parameters are, for example: a P-wave with deep terminal negativity, prolonged QT-interval ang T-peak to T-offset segment, QRS duration and fragmentation, bundle branch block, ST-segment depression and elevation, T-waves (inverted, T-wave axes), spatial angles between QRS and T vectors, premature ventricular contractions, and ECG hypertrophy

criteria [70, 71].

While atria activation and relaxation hardly differs between human and mouse, there are clear dissimilarities between shapes of ventricular action potentials, described in the following subsections. However, further detailed explanations can be found in [9]. Figure 2.11 shows a schematic representation of the ECG signal and its features in human 2.11.a and mice 2.11.b. The isoelectric or baseline line for mouse ECG is the segment between the end of T-wave and the beggining P-wave [72].

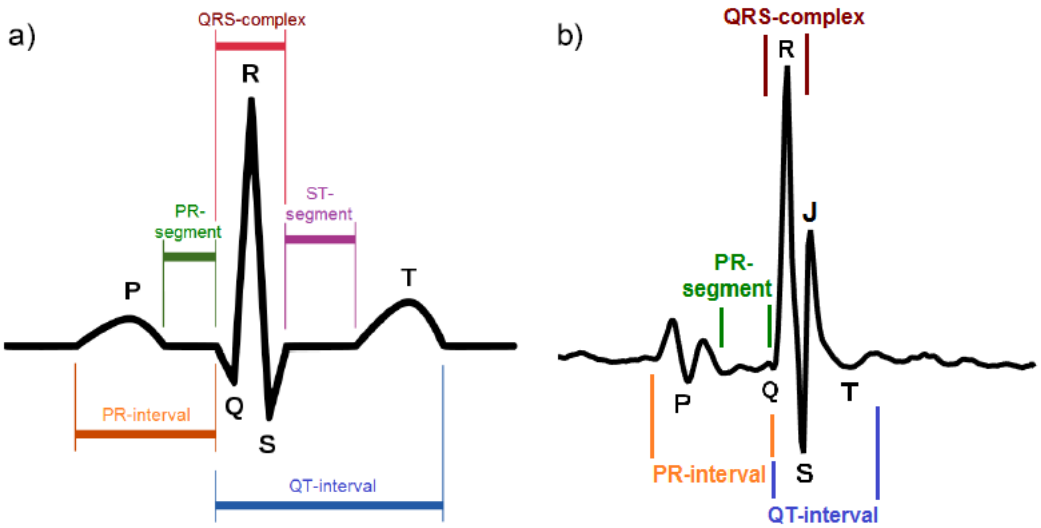

Figure 2.11: *Schematic representation of a human (a) and murine (b) ECG signal and its features. Adapted from [9].*

P-wave

In mice as well as in humans, the activation of atria starts around the SA node and spreads to the left and right atrium. The spread of activation is similar in both species. However, it is not clear if mice have the conduction pathway between the two atria. The P-wave describes the atrial depolarization towards the apex (the tip). The maximum of the P-wave is reached when half of the atria are depolarized [73].

PR-interval

The PR-interval represents the traveling time of the impulse from the SN node trough the AV node, spreading from the right atria to the left atria and entering the ventricles [74]. The impulse is conducted from the AV node to the bundle of His (figure 2.1) during the flat part of the PR-interval (the PR-segment), corresponding to the full depolarization of the atria in humans. Murine ECG signals are characterized by a small deflection that follows the P-wave. According to Boukens et al. [64], this deflection could represent the atrial repolarization. In humans,

however, atrial repolarization happens during the QRS-complex [73]. Another possibility is that this deflection emerges when the electrodes are positioned in a way that atria are not in the middle [64].

QRS-complex

In humans, ventricular depolarization takes place in the interventricular septum located on the left ventricular side. It then spread towards the right ventricle [75]. There are two ways in which ventricular depolarization starts in mice. One is by defined breakthroughs in the right ventricle followed by propagation into the left ventricular part. The other one starts in the left ventricular apex with shortly following breakthroughs in the right ventricle [73]. Besides, the activation in humans goes from the apex to the base of the heart [75]. In mice, on the contrary, the interventricular septum is excited from base to apex [73]. In both cases, the endocardium is earlier activated than the epicardium [76]. Nonetheless, the QRS-complex have a similar shape in both species.

ST-segment and J-wave

Goldbarg et al. [77] noticed that adding the J-wave to the QRS-complex duration would overestimate the complete activation time. They published the first detailed study of different electrocardiographic variables and the repolarization mechanism of mice.

The ST-segment in humans describes the phase when both ventricles are fully activated. It is represented by a plateau phase which separates the depolarization (QRS-complex) from the repolarization (T-wave) [64]. In mice, due to the lack of a distinct plateau phase, depolarization and repolarization waveform overlap, i.e. a significant part of the repolarization happens before the entire activation is completed. The rapid initial repolarization in murine ECG signals is the source of the J-wave. It follows immediately after the S-wave (see figure 2.11.b). J-wave and T-wave, both belong to the repolarization of the ventricle in mice. The end of right ventricular repolarization correspond to the J-wave offset [64].

T-wave

The T-wave represents ventricular repolarization, although there are some noticeable differences depending on the specie. The origin of the murine T-wave is the difference in ventricular repolarization between the left and right part. In humans, the T-wave is a deflection easy to distinguish, since the ST-segment is a clear boundary for depolarization and repolarization [64].

While in humans the last activation moment detected takes place in the left and right ventricular

base [75], it occurs in the right ventricular base in a mouse heart, since the activation is faster in the left ventricle [64]. Repolarization spreads from the right ventricular base to the right ventricular apex. The sequence of relaxation is the opposite of activation [76], from apex to base [73]. The low amplitude of this wave is due to the weak electrical forces generated by the slow gradual time course for relaxation [78]. It is a positive or negative deflection depending on the placement of the electrodes or leads [72].

QT-interval

The T-wave offset concurs with the left ventricular repolarization in humans [64]. However, in mice, neither the QJ nor the QT-interval correspond to the complete ventricular depolarization and repolarization [72]. In the case of humans, the QT-interval does reflect the complete depolarization and repolarization phase of ventricles [8].

The QT-interval in humans depends on the heart rate. A possible correction formula was announced by Bazett [79] :

$$QT_c = QT/\sqrt{RR} \tag{2.5}$$

This formula was adapted by Mitchell et al. [80] for its use in mice, where an average duration of an RR-interval of 100 ms was used to normalize the RR-intervals:

$$QT_c = QT/\sqrt{(RR/100)} \tag{2.6}$$

However, a heart rate correction should not be done in anesthetized mice according to Speerschneideret al. [72], since anesthetics can change cardiac repolarization.

CHAPTER 3

Mouse Models, Techniques and Methods

With the growth of genetic engineering, mice have become increasingly common as models of human diseases, and this has stimulated the development of techniques to assess the murine cardiovascular system. At the same time, the rising interest of non-invasively measuring parameters related to cardiovascular diseases has induced the development of new techniques to determine biomarkers of cardiovascular risk such as PWV and pulse pressure (PP), which represent arterial stiffness and wave reflection behaviour [4]. In the following, important mouse models and measurements methods and techniques for cardiovascular research are introduced.

3.1 Mouse Models

There are three main types of mouse models of human diseases that have been developed: knockout (KO), transgenic, and knockin models. The “first generation” mouse models, which resulted from gene targeting, were the so-called knockouts. In these genetically modified mice, researchers have inactivated, or "knocked out", an existing gene by replacing it or disrupting it with an artificial piece of DNA. In transgenic models the desired gene is randomly integrated in the host genome. Knockin refers to those that have been genetically modified by the substitution of a DNA sequence information in a certain genetic position or the insertion, or gene "knock in", of new sequence information previously not found in that specific location [81].

The most widely genetically modified strain of mice for the generation and analysis of transgenic and knockout types, is the C57BL/6, often referred to as "C57 black 6", "C57" or "black 6" [34, 82, 83], illustrated in figure 3.1. If not specified a transgenic type, when referring to a group of C57BL/6 mice, they are considered as wild type controls. In the following, several mouse models genetically modified are described.

Figure 3.1: *Mouse strain C57BL/6 [84].*

ApoE-KO

Apolipoprotein E deficient, also known as ApoE-KO or just ApoE mice, is probably the most common mouse model in cardiovascular research [4, 82]. Apolipoprotein is an important mediator for hepatic metabolic clearance of circulating cholesterol [85]. This atherosclerosis mouse model displays poor lipoprotein clearance and the subsequent accumulation of cholesterol particles in the blood, which promotes the development of atherosclerotic plaques [86].

dKO

The double (SR-BI/ApoE) knockout (dKO) mouse is a kind of ApoE model with mutations in the genes for the high density lipoprotein (HDL) receptor SR-BI and ApoE. This receptor, called scavenger receptor class B type I, is responsible for regulating lipoprotein metabolism and cholesterol transport to steroidogenic tissues and to the liver for biliary secretion [87]. These mouse models exhibit morphological and functional defects with similarities to those seen in humans with coronary heart diseases (CHD) [88]. Some of the CHD developed by dKO mice are hypercholesterolemia and dramatically accelerated atherosclerosis. These diseases could lead to severe occlusive coronary arterial lesions, probable ischemia, multiple myocardial infarctions (MI), enlarged hearts, and cardiac dysfunction (ECG abnormalities) in very young mice [88].

Eln mouse

Eln mice, with elastin gene mutations, have high blood pressure and reduced aortic compliance, but no evidence of elastic fiber fragmentation. This kind of mouse is used to determine the effects of altered vessel elasticity on cardiovascular development [89].

α-SMA$^{(-/-)}$

Smooth muscle actin (SMA) knockout (α-SMA$^{(-/-)}$) mice, or simple αSMA mice, have also been used in the study of arterial stiffness showing a different blood velocity behaviour compared with wild type (WT) mice, affected by the lack of smooth muscle α-actin or vascular tone [90]. Since

smooth muscle α-actin has a central role in regulating vascular contractility and blood pressure homeostasis, these mice have more compliant vessels than normal ones [90, 91].

DES-KO

Desmin knockout mice (DES-KO) or simply DES mice, are deficient in desmin protein, which is the main component of the intermediate filaments of smooth muscles. These mice have myopathies in skeletal and cardiac muscle tissue. For this reason, DES mice are used to assess the viscoelastic properties, the mechanical strength and the structure of the carotid artery [92].

LDLR$^{(-/-)}$

The LDLR$^{(-/-)}$ mouse represents a model of familial hypercholesterolemia due to one of the mutations affecting the low density lipoprotein receptor (LDLR) gene. Mice genetically deficient in LDLR exhibit a moderate increase of plasma cholesterol level and slowly develop atherosclerosis on normal diet. Nonetheless, the severity of the hypercholesterolemia and atherosclerotic lesions in LDLR$^{(-/-)}$ mice can be accelerated by feeding a high-fat, high-cholesterol diet [93, 94].

MGP-KO or Matrix GLA protein-KO

Matrix GLA protein (MGP) is an inhibitor of calcification in the arterial wall. It plays a key role in the formation of atherosclerotic plaques and vascular calcification. Calcified arteries result in higher arterial stiffness and systolic blood pressure [95]. MGP deficiency in mice results in premature calcification in bone, calcification of normally non-calcifying cartilage, such as the trachea, and severe vascular calcification leading to premature death [95].

eNOS$^{(-/-)}$

Endothelial nitric oxide synthase knockout mice or eNOS$^{(-/-)}$, also known as nitric oxide synthase 3 (NOS3) or symply eNOS, is another model known to have elevated blood pressure and increased arterial stiffness. Besides, reduced availability of nitric oxide (NO) leads to hypertrophy in these animals [66].

Fbn1$^{C1039G/+}$ MFS

Marfan syndrome (MFS) is a disease of connective tissue caused by mutations in the gene encoding fibrillin-1 (Fbn1) [96]. This syndrome causes defective microfibrillar deposition, emphysema, deterioration of aortic wall and kyphosis. It involves a high risk of mortality due to

aortic dissection and rupture [97]. Fbn1$^{C1039G/+}$ MFS mice or simply MFS are mouse models of Marfan syndrome. They present anomalies of Marfan syndrome like significant aortic dilation, central aortic stiffness, and left ventricular systolic and diastolic dysfunction.

HT

Hypertensive or HT mice are not genetically modified. Instead, they are administrated an infusion of angiotensin II (ANGII), a peptide that plays a central role in the mechanisms of hypertension. In systemic vessels, ANGII acts as a potent vasoconstrictor, producing endothelial dysfunction and smooth muscle proliferation. In the cerebral circulation, on the contrary, ANGII acts as a vasoconstrictor, affecting cerebrovascular autoregulation [98].

AβPP/PS1 or APPPS1 or AD

Alzheimer's disease (AD) is a neurodegenerative disorder characterized by progressive loss of memory and cognitive function [99]. AβPP/PS1 mice are also known as APPPS1 or simply AD mice. They are transgenic mice expressing mutant forms of amyloid-β precursor protein (AβPP) and presenilin-1 (PS1) that recapitulate several aspects of this disease [100]. They present amyloid β peptide (Aβ) plaque deposition in the neocortex, the hippocampus, thalamus and brainstem.

AD&HT

AD&HT or ANGII-APPPS1 is a mouse model of Alzheimer's disease (AD) combined with hypertension (HT). AD mice are administrated infusion of hypertensive doses of angiotensin II (ANGII). This treatment results in a raise in systolic arterial pressure (170 mmHg against 110 mmHg in normotensive mice). Unlike normal AD mice, AD&HT present a spectrum of cerebrovascular dysfunction closer to that found in humans. For this reason, this model represents the human AD pathology better [101].

db/db

Diabetic or db/db mice are obese leptin receptor-deficient mice [102]. These mice, commonly used to model diabetes type II and obesity, develop obesity and diabetes similar to non-insulin-dependent diabetes mellitus in humans. At the age of 5 weeks, obesity, hyperglycemia, and hyperinsulinemia become evident [102, 103].

3.2 Measurement Techniques

In order to study the mechanical properties of the vessels, many practical experiments have been carried out in mice. Within the years, new techniques to assess biomarkers of cardiovascular risk have been developed [33]. Some of these parameters are blood pressure [104], blood flow velocity [4, 52], PWV [105–107] and pulse pressure, most of them increased as a consequence of progressive large artery stiffening [108]. In the following, a short overview of selected measurement techniques for the assessment of the cardiovascular system in mice is given.

3.2.1 Invasive Techniques

First approaches to measure blood pressure in mice were invasive surgical procedures. The arterial blood pressure is directly measured with the aid of a sensor or transducer inserted into the arterial system. Some of the most common invasive blood pressure techniques are based on fluid-filled catheters, radiotelemetry systems, and transducer-tipped catheters [109].

Nowadays, direct blood pressure measurements are commonly used for evaluating the accuracy of new non-invasive blood pressure technologies. Blood pressure is usually measured on the rodent's carotid artery as shown in figure 3.2 [110].

Radiotelemetry is a very reliable blood pressure technology and is also used as a comparison method to determine the accuracy of non-invasive blood pressure technologies. It is a highly invasive surgical procedure, since it involves implanting radio transmitters into the rodent's body. It allows to measure blood pressure continuously in free-moving laboratory animals, but enhances morbidity and high stress levels [111].

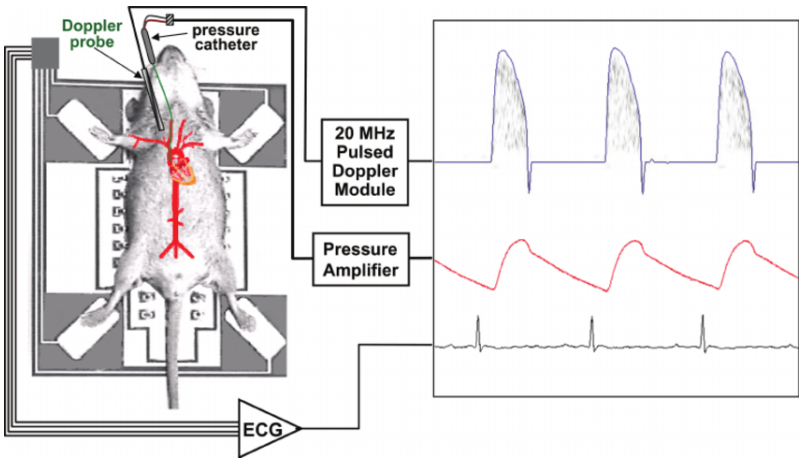

Figure 3.2: *Experimental setup to measure aortic blood flow velocity, aortic blood pressure, and ECG in mice [110].*

3.2.2 Doppler Ultrasound

Doppler ultrasound (US) instruments measure blood velocity by detecting the difference in frequency between an emitted burst of ultrasound and the returning echoes from moving blood. However, mouse heart rates are higher than human's and thus, higher ultrasonic frequencies than for humans have to be used: 10-20 MHz ([4]) instead of 5–13 MHz ([112]).

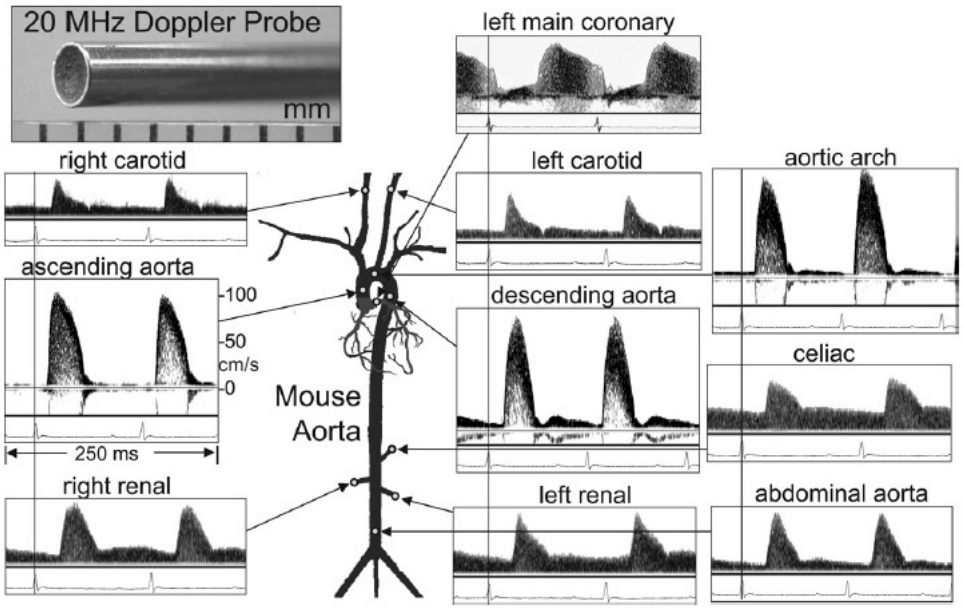

Figure 3.3: *Doppler velocity signals from peripheral arterial sites in mice [4].*

Figure 3.3 illustrates Doppler velocity signals from different peripheral arterial sites in an anesthetized mouse using a 2 mm diameter 20 MHz probe. The vertical lines correspond to the R-wave of the ECG, used to measure pulse arrival times for the calculation of the pulse wave velocity (PWV).

3.2.3 Magnetic Resonance Imaging

Image screening tools such as magnetic resonance imaging (MRI) can also enhance the quality of investigating the cardiovascular function in mice [83] and be used for measuring the diameter of vessels. A strong magnetic field produced by powerful magnets forces protons in the body to align with it. Then, a radiofrequency current is pulsed through the mouse and protons spin out of equilibrium, straining against the pull of the magnetic field. When the radiofrequency field is turned off, sensors detect the energy released as the protons realign with the magnetic field and the time it takes, allowing to distinguish between various types of tissues based on these magnetic properties [113].

Figure 3.4.a shows the slice positioning for the local PWV measurements using the QA method (see section 3.3.2). Areas are approximated by measuring the diameter of the ascending aorta

in 3.4.b and the abdominal aorta in 3.4.c.

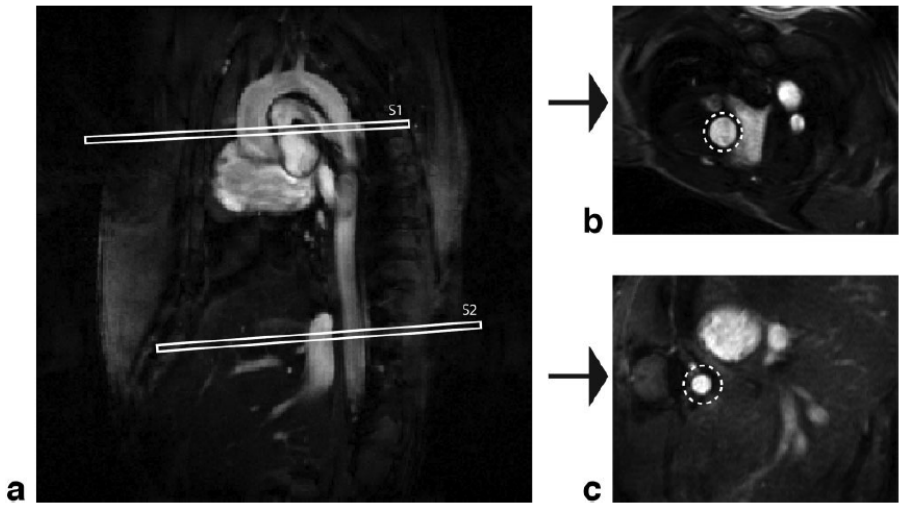

Figure 3.4: *Slice positioning for the local PWV measurements in a. b: Ascending aorta. c: Abdominal aorta [34].*

3.2.4 The Tail-cuff Method

Probably the most commonly used non-invasive technique to detect changes in volume of tail flow is the tail-cuff method. In the past, tail-cuff method used sensors that only allow the measurement of systolic blood pressure [114].

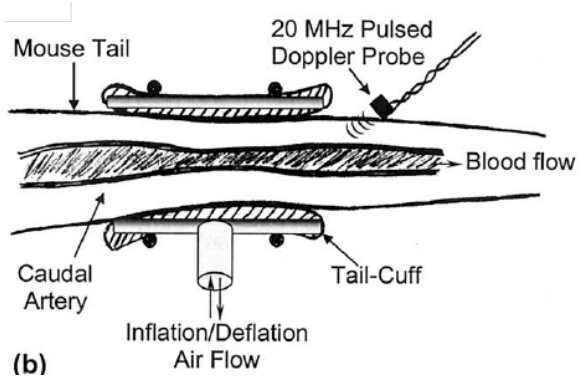

Figure 3.5: *Longitudinal view of the tail artery with the tail-cuff and the Doppler sensor placement [52].*

In more recent studies, the tail-cuff method was as well used to identify the diastolic pressure. The tail-cuff pressure signal (black decreasing line) is compared to the catheter pressure waveform in figure 3.5. The cuff is pressurized to the suprasystolic level to completely occlude the tail artery and then released gradually. As one can see in figure 3.6, the pressure at which the tail flow reappears is recorded as systolic and the pressure at which the tail flow becomes continuous is recorded as diastolic blood pressure [52].

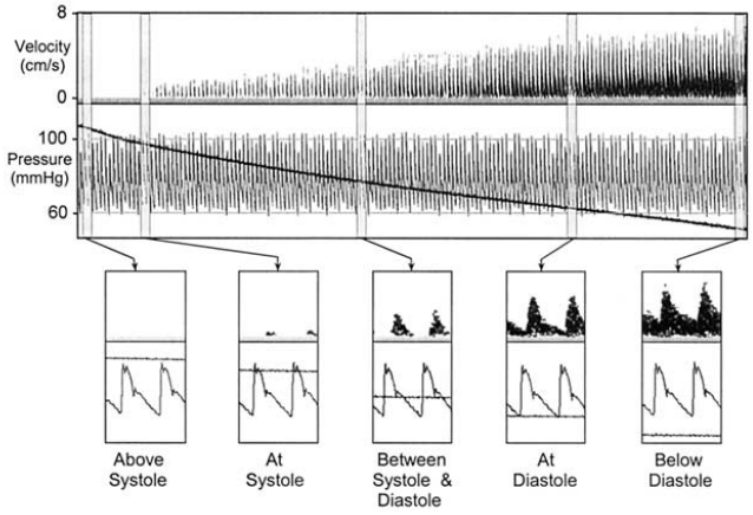

Figure 3.6: *Catheter BP and reappearance of V in the mouse tail artery with release of pressure in the tail-cuff [52].*

3.2.5 Applanation Tonometry

Using ultrasound is fast and accurate, but the required tools are expensive and technically complex. Applanation tonometry is a new and simple technique based on Laplace's law and the use of pressure sensors [115, 116]. It has recently become available to detect new and several hemodynamic parameters. Furthermore, it is considered the gold standard technique for measuring PWV non-invasively by the assessment of arterial pressure wave forms [66]. Figure 3.7 shows the relationship between the wall tension (T), the transmural pressure (P_t) and the radius (r) of a cylindrical tube with low wall thickness (μ). When a pressure sensor applanates a tube wall (in this case the artery wall) by external pressure (P_e), P_e is identical to internal pressure (P_i) so that the sensor output exactly reflects P_i [115].

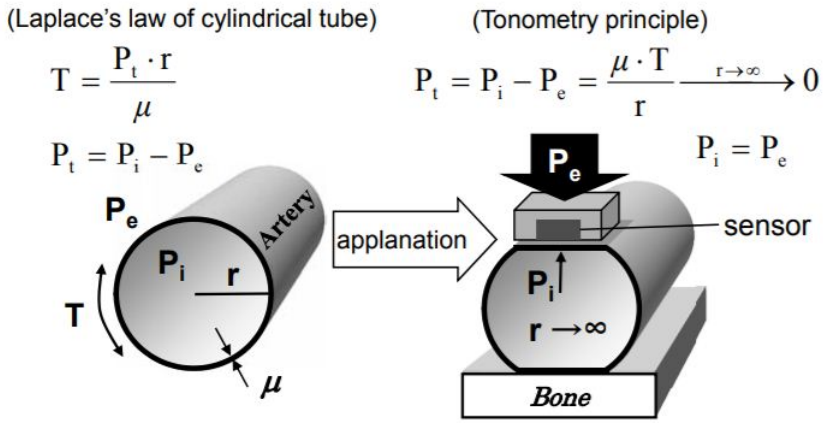

Figure 3.7: *Principle of arterial applanation tonometry. P_e = external pressure; P_i = internal pressure; P_t = transmural pressure; r = radius of wall curvature; T = wall tension; μ = wall thickness [115].*

3.3 Methods Used to Calculate PWV in Mice

Different methods are used to assess PWV. While some measure the blood flow velocity wave [53, 56, 117], others determine the velocity of the pressure wave in the aortic wall [34, 82].

3.3.1 The Transit Time Method

PWV is usually assessed by measuring pressure signals at two different arterial sites and dividing the distance between the two measurement sites (Δz) by the difference in arrival times of the velocity pulse timed with respect to the R-peak of the ECG (Δt). This method is known as transit time method (TT) (figure 3.8) [118].

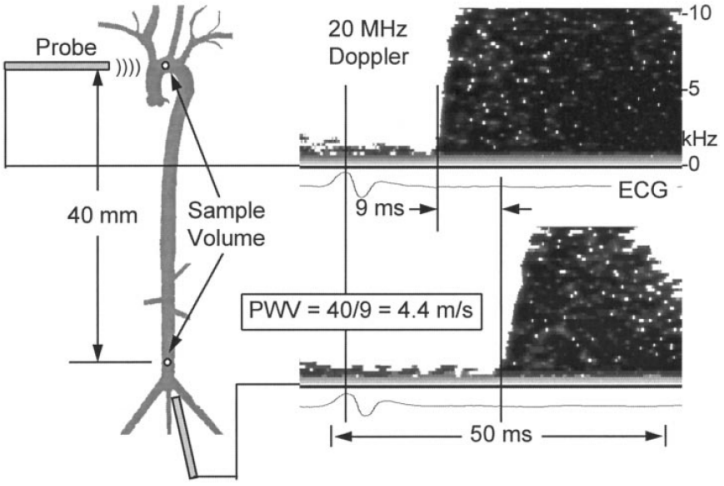

Figure 3.8: *Determination of aortic PWV in mice using the transit time method: 40 mm from aortic arch to descending aorta [25].*

The TT method is also known as foot-to-foot method since the foot of the velocity wave is measured at each site with respect to the R-wave of the ECG and then PWV is calculated dividing the separation distance by the difference in R-foot times [119].

Doppler ultrasound-based TT methods have been applied to mice and have provided first results of an average PWV over the propagation pathway, giving information about the vessel wall thickness, the vessel diameter and the local elastic modulus [34]. Previous studies have also reported PWV assessments in mice obtained by applying TT method on velocity-encoded magnetic resonance imaging data [83].

3.3.2 The QA Method

PWV can also be achieved using the QA method [107], although this method is usually complex since it requires angle correction of the Doppler velocity and needs careful imaging of the aorta [34, 120]. Local area compliance is indirectly related to the characteristic impedance Z_C, the

ratio between pressure variation (ΔP) and flow variation (ΔQ). This fact implies that it is also directly related to PWV. As result, local PWV can be calculated as the aortic Doppler flow divided by the aortic area change (ΔQ/ΔA) as shown in figure 3.9 [120].

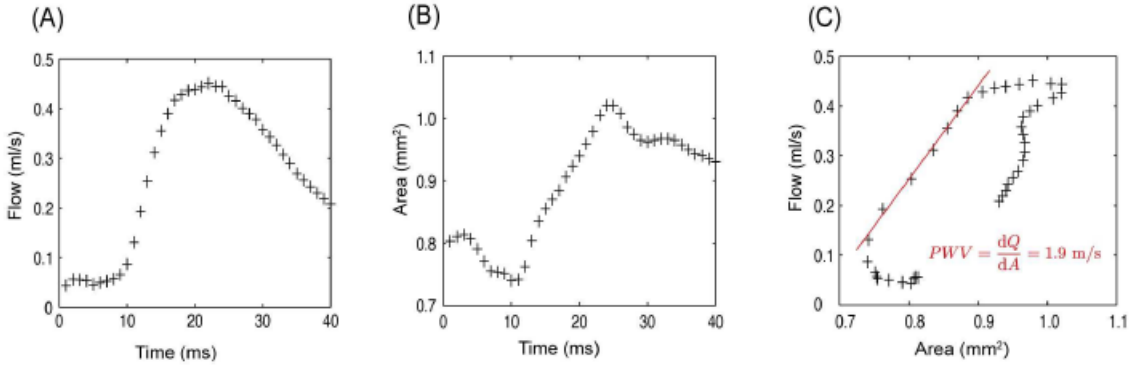

Figure 3.9: *Local determination of PWV in a WT mouse using the QA method, by simultaneously recording flow (A) and cross-sectional area (B) through an imaging slice perpendicular to the upper abdominal. The slope of the flow/area plot (C) represents the local PWV at the examined location [121].*

3.3.3 The LnD-V Loop Method

This method was first introduced by Khir et al. to be used in humans [122]. It is based on the hypothesis that, in the absence of wave reflections, the relationship between the natural logarithm of diameter (lnD) and blood flow velocity (V) should be linear. When plotting lnD against velocity, a loop is created as illustrated in figure 3.10, denoted as lnD-V loop.

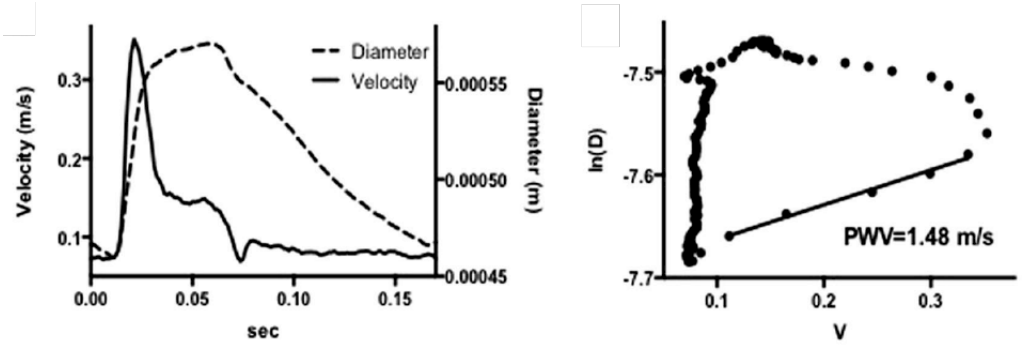

Figure 3.10: *Determination of local PWV in ice using the lnD-V loop method. Left: diameter and mean velocity curves. Right: calculus of PWV by means of the lnD-V loop [6].*

The slope of the initial linear portion of the created loop is directly related to the speed of the wave. Thus, PWV can be calculated using the following formula:

$$PWV = \frac{dV}{2 * dlnD} \tag{3.1}$$

Further explanations about this method can be found in section 6.4.

3.4 Evolution of Methods and Techniques

In 1997, G. F. Mitchell et al. carried out the first study comparing various methods for measuring PWV in rats (e.g. the foot-to-foot technique and methods based on the pressure transfer function) [108]. These techniques vary in the way of determining the time delay between simultaneously recorded waveforms using catheter-tip pressure transducers. The goal was to establish a robust method to assess the regional variability in PWV along the aorta in small-animal models such as rats. As conclusion, they demonstrated that foot-to-foot techniques were more reliable for assessing PWV rather than assessing the entire pressure waveform [108].

Also in 1997, C. J. Hartley and A. K. Reddy et al., from the Department of Medicine in the Baylor College of Medicine in Houston (Texas), developed a non-invasive Doppler ultrasound technique to determine the arterial PWV, based on the TT method in anesthetized mice (nembutal). They used their own 20 MHz pulsed Doppler instrument to measured flow velocity signals from the aortic arch and the abdominal aorta, as shown in figure 3.8 [25]. The results were compared to simultaneous invasive tonometry measurements. This study concluded that PWV could be determined non-invasively in mice [119].

In 2003, C. J. Hartley and his group designed a non-invasive method for measuring blood pressure in mice, including diastolic blood pressure, using a 20 MHz pulsed Doppler tail flow velocity sensor. The method combined the tail-cuff method with a 20 MHz pulsed Doppler tail flow sensor, illustrated in figure 3.5. The method was validated comparing the tail-cuff measurements with the pressure signals obtained simultaneously from a fluid-filled arterial catheter. Thus, comparing the tail-cuff blood pressure (tBP) with the catheter blood pressure (tBP) [52].

In 2009, the team of V. Herold and M. Parczyk et al., from the Julius-Maximilians Universität in Würzburg (Germany), designed a non-invasive high field MRI method at 17.6 T to assess local aortic PWV in mice. The aim of the study was the detection of atherosclerotis in the descending aortas. PWV was calculated using the QA method, based on the flow area relation during early systole. The feasibility of the presented high field MRI technique was demonstrated since the results obtained corresponded to reported data [34].

In 2010, the group from Würzburg developed a high field cardiovascular magnetic resonance (CMR) protocol in order to distinguish groups of healthy and atherosclerotic mice by means of the PWV in the descending aortas using the TT method. The CMR method was validated by pressure waveform measurements on a pulsatile elastic vessel phantom that proved its accuracy, since the values were similar to those obtained with a catheter [83].

In 2011, A. K. Hartley et al. developed a non-invasive and non-imaging Doppler technique for measuring blood velocity in the large and small peripheral arteries of anesthetized mice, by adapting technology originally for humans to be used in mice [4]. This allows measuring cardiac filling and ejection velocities in order to determine parameters like PWV, peripheral blood

velocity and vessel wall motion waveforms for the calculation of the pressure drop across stenoses, as well as the left main coronary velocity for the estimation of coronary flow reserve (CFR). The agreement between measured and calculated pressure drops demonstrates the validity of the method [4].

In contrast to the US Doppler techniques developed by the team of C. J. Hartley and A. K. Reddy et al. to achieve the PWV value from arteries of mice, Arthur Leloup et al., from the University of Antwerp (Belgium), developed in 2014 a novel non-invasive technique based on applanation tonometry for the pharmacological alteration assessment of the carotid–femoral PWV (cfPWV) [66]. Carotid–femoral transit time (Δt) was determined using the time difference between the foot of carotid and femoral artery pressure pulses (foot-to-foot method). Applanation tonometry was validated comparing the results with echo Doppler velocimetry observations.

Also in 2014, N. D. Lascio et. al. presented an US-based WIA technique for assessing arterial PWV in mice non-invasively, using only ultrasound images [63]. Diameter and flow velocity values were obtained from abdominal aorta using B-mode and PW-Doppler, respectively. B-mode images were obtained with an US probe working at 21 MHz. PWV values were obtained from the slope of the corresponding linear parts of the velocity-diameter (lnD-V) loop, in the early systolic phase (figure 3.10). The group sustained that different PWV values allow discrimination between age groups and evaluation of local vascular stiffness in wild type mice. The resulting WI signal had different units but was similar in shape to that obtained by means of standard invasive WIA. However, the method had some important limitations, like the lack of comparison to an invasive local stiffness evaluation technique.

In 2017, V. Herold and his team developed a new accelerated QA method to quantify local aortic stiffness (PWV) in the abdominal aorta in mice [123]. Phase-contrast cardiovascular magnetic resonance imaging (PC-CMR) at 17.6 T was used for the evaluation of local temporal changes in blood flow and vessel cross-sectional area. To speed up post-processing and to eliminate operator bias, they introduced a new accelerated and semi-automatic segmentation algorithm to quantify cross-sectional areas of the aortic vessel, the K-t BLAST acceleration. It allows data acquisition 6 times faster than with fully sampled data, although with a reduced temporal resolution after reconstruction due to undersampling [123]. It was applied in 10 eight month old mice (4 C57BL/6 mice and 6 ApoE$^{(-/-)}$-mice) at 12 adjacent locations along the abdominal aorta. As expected, the method delivered reliable measures for the local PWV compared to PWV measures obtained by means of manual segmentation of the vessel cross-section (QA method [34]).

The evolution of methods and techniques in cardiovascular research in mice is summarized in table 3.1.

Author Year (Ref.)	Study design	Animal	Animal model	Sample Size/- Sex/Age	Technology	Parameters (method)	Main result	Conclusion
Mitchell et al. 1997 [108]	CS	Rats	Hypertensive	n:7/M/18m	Catheter	PWV (TT)	Accuracy and reproducibility are comparable to more complex methods.	PWV can be reliably measured in rodents using foot to foot methods.
Hartley et al. 1997 [119]	CS	Mice	-	n:82/-/-	Doppler US	PWV (TT)	Using Doppler to non-invasively measure PWV in mice produces similar results with invasive tonometry.	Non-invasive Doppler ultrasound technique can be used to determine PWV in mice.
Reddy et al. 2003 [52]	CS	Mice	WT	n_1:16/-/13-30w, n_2:20/-/13-30w	Doppler-US	SBP, DBP	Linear relationship between central and tail BP for systolic and diastolic pressure.	First non-invasive approach of tail-cuff method in mice to acquire DBP.
Herold et al. 2009 [34]	CS	Mice	G1:WT, G2:ApoE	n_1:5/-/8m, n_2:9/-/8m	MRI	Local aortic PWV (QA)	QA measurements show high similarities with reported data, confirming the feasibility of the technique.	High resolution MRI methods allow a higher image quality and more accurate determination of area than US techniques.
Parczyk et al. 2010 [83]	CS	Mice	G1:ApoE (western diet, 10w), G2:WT	n_1:5/F/8m, n_2:4/-/8m	CMR	Regional PWV (TT)	Accuracy of the MR method to assess PWV on a vessel phantom.	MR methods can be used to distinguish healthy from atherosclerotic mice.
Hartley et al. 2011 [4]	L: 21d after TAC	Mice	Stenosis	n:5/-/-	Doppler US	PWV (TT), CFR (H/B), S/D, V, D.	Agreement between the measured and calculated pressure drops when cannulating both carotid arteries after TAC in mice.	The method allows the high-resolution measurement of V and D in large and small peripheral vessels in mice.

Author Year (Ref.)	Study design	Animal	Animal model	Sample Size/- Sex/Age	Technology	Parameters (method)	Main result	Conclusion
Leloup et al. 2014 [66]	L: perindo-pril (12d, G1), ethanol (12d, G1)	Mice	G1:eNOS (sevo. anes.) G2:WT (sevo., nembu.)	n_1:22/-/-, n_2:33/-/-	Applanation tonometry	cfPWV	High fidelity and reproducibility of the non-invasive method to asses PWV, validated with Doppler echo.	Powerful tool for the non-invasive assessment of cfPWV in mice, useful for the study of large arterial stiffness.
Lascio et al. 2014 [63]	CS	Mice	G1:WT G2:WT	n_1:10/M/5.5m, n_2:9/M/15.5m	Doppler US	aaPWV, reID	Assessment of age-associated changes in abdominal aorta PWV, although lack of comparison to an invasive technique.	The system allows the non-invasive evaluation of local vascular stiffness in the murine abdominal aorta.
Herold et al. 2017 [123]	CS	Mice	G1:ApoE, G2:WT	n_1:6/-/ 8m, n_2:4/-/8m	k-t BLAST PC-CMR	Local PWV (QA)	Agreement between fully sampled local PWV and the k-t BLAST acceleration (x6 faster).	Reliable accelerated data acquisition to calculate local PWV including semi-automatic post-processing.

Terminology:
* L = longitudinal study design (T0, T1)
* CS = cross-sectional study design
* w = weeks, m = months
* G = group
* F = female; M = male;

Table 3.1: *Evolution of methods and techniques in cardiovascular research in mice.*

CHAPTER 4

Cardiovascular Research in Mice

A wide range of studies have been accomplished in mice in the past two decades in order to understand the incidence of arterial stiffness in the development of vascular diseases. It is known that increased aortic stiffness is associated with atherosclerosis and can be used as a predictive value for cardiovascular events [33, 82, 124].

The first study in revealing an increase in aortic stiffness measuring PWV in old ApoE-KO mice compared to controls was carried out by the team of Y.-X. Wang and R. M. Fitch et al., from the Department of Pharmacology at Berlex Biosciences, in Richmond (California) in 2000 [82].

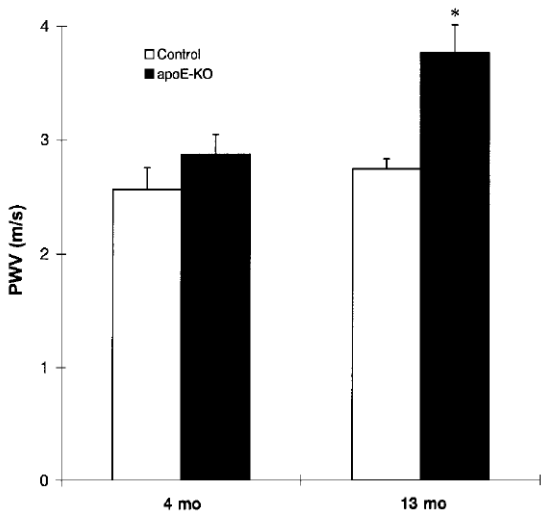

Figure 4.1: *PWV in ApoE-KO versus control mice [82].*

The study proved that PWV of the 13 month old ApoE-KO mice was significantly higher compared to 4 month old ApoE-KO and age-matched controls (figure 4.1). They demonstrated that PWV, which was measured invasively, could be used as a surrogate endpoint or marker for estimating the progression of atherosclerosis, since it increased with increasing arterial stiffness [82].

Furthermore, they examined whether endogenous nitric oxide (NO) was involved in the regulation of vascular stiffness. The molecule NO is very important in this area since a deficiency is a main feature of atherosclerosis, intimal hyperplasia, thrombosis, and aneurysm formation [125]. They demonstrated that NO modulates vascular compliance independent of blood pressure changes in mice [82] and rats [60], which means that a good endogenous NO system is required to maintain

normal vascular compliance.

Histological evaluation revealed focal fragmentation of the elastic laminae in the aortic walls of oldest ApoE-KO mice with extensive atherosclerotic lesions in the aorta. Endothelial nitric oxide (EDNO)-mediated vasorelaxation in response to acetylcholine (ACh) was markedly diminished in the aortic rings isolated from these mice compared to age-matched controls. This would demonstrate that the lack of EDNO is involved in the development of atherosclerosis, since it contributes to the decrease in vascular elasticity, provoking endothelial dysfunction [82].

In 2000, Y.-X. Wang and R. M. Fitch et al. collaborated with the group of C. J. Hartley and A. K. Reddy et al. to apply non-invasive techniques to measure PWV in ApoE-KO mice. The study determined an increase in PWV in ApoE mice, this time measured non-invasively [25].

Together, both groups observed a significant alteration (figure 4.2) in the magnitude and shape of the aortic arch velocity signal in ApoE mice. This change is indicated by the A2/A1 ratio, where A1 and A2 designated the two phases in which the acceleration in the aortic arch occurred. Neither blood pressure nor heart rate were statistically different in ApoE-KO versus WT mice, as one can see in table 4.1, together with some other physical and cardiac parameters [25].

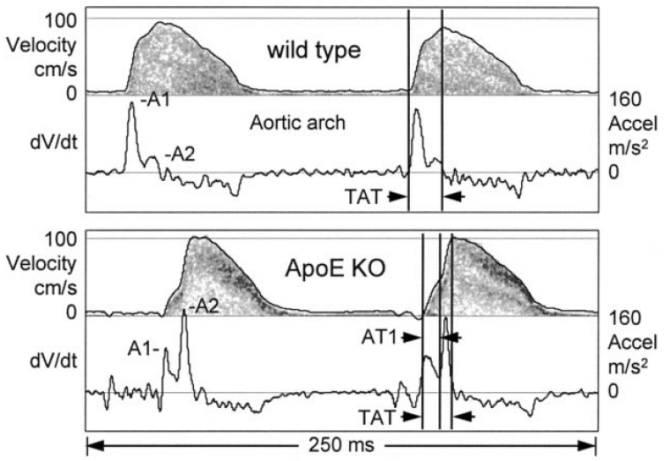

Figure 4.2: *Velocity and acceleration curves from the aortic arch of a WT and an ApoE mouse [25]. The acceleration in the ApoE mouse occurs in 2 phases with the second peak (A2) being higher than the first peak (A1). AT1 = early acceleration time, TAT = total acceleration time.*

The most logical explanation is an alteration in vascular impedance that changes the magnitude and timing of peripheral wave reflections. In the carotid artery, the reflected wave travels opposite to the direction of flow suppressing velocity, whereas in the aortic arch, the reflected wave from the carotid travels in the direction of flow and enhances velocity after entering the aorta [25].

In 2001, the group of R. M. Fitch et al. studied the administration of a bolus injection of a NO synthase inhibitor (L-NAME) in a group of rats. This would also increase the blood pressure, which has been known to affect PWV [5]. In order to standardize the blood pressure, they administered phenylephrine (PE) to mimic the blood pressure changes induced by L-NAME,

Parameters	WT (n)	ApoE-KO (n)	KO/WT	P value
Physical and general data				
Systolic blood pressure (conscious), mmHg	136 ± 7.4(10)	140 ± 7.6(10)	1.03	NS
Heart rate (conscious), beats/min	678 ± 12.5(10)	712 ± 10(10)	1.05	NS*
Cardiac Doppler data				
Heart rate (anesthetized), beats/min	439 ± 10.4(10)	488 ± 10.3(10)	1.11	NS*
Peak aortic velocity, cm/s	89.2 ± 5.8(10)	133.4 ± 7.8(10)	1.50	<0.01
Mean aortic velocity, cm/s	22 ± 1.6(10)	35.9 ± 2.7(10)	1.60	<0.001
Stroke distance, cm	3.1 ± 0.2(10)	4.5 ± 0.3(10)	1.45	<0.001
Ejection time, ms	52.9 ± 1.2(10)	47.4 ± 1.0(10)	0.90	NS*
Peak aortic acceleration, m/s^2	100 ± 12(10)	118 ± 7.8(10)	1.18	NS*
Peak mitral velocity, cm/s	47.2 ± 5.3(10)	92 ± 7.2(10)	1.95	<0.001
Mean mitral velocity, cm/s	11.4 ± 1.3(10)	20.6 ± 1.7(10)	1.81	<0.001
Aortic Doppler data				
Pulse-wave velocity, cm/s	379 ± 10.1(10)	428 ± 14.5(10)	1.13	<0.05
Aortic arch A_1, m/s^2	129 ± 14(10)	86 ± 8.7(10)	0.67	<0.001
Aortic arch acceleration time 1, ms	8.8 ± 0.6(7)	8.6 ± 0.4(10)	0.98	NS
Aortic arch A_2, m/s^2	53 ± 11(10)	152 ± 18.1(10)	2.87	<0.001
Aortic arch A_2-to-arch A_1 ratio	0.46 ± 0.14(10)	2.1 ± 0.4(10)	4.57	<0.001
Total aortic arch acceleration time, ms	15.8 ± 1.2(10)	15.2 ± 0.8(10)	0.96	NS

Table 4.1: *Statistical comparison between wild type and ApoE mice physical and cardiovascular parameters. Modified from [25].*

compensating the pressure-dependent component of the PWV changes (figure 4.3) [60]. PWV was significantly higher with L-NAME than with PE treatment (figure 4.4, *p $<$ 0.05, † p $<$ 0.01). This suggested that an acute lack of endogenous NO increases arterial stiffness independent of changes in MAP. However, PWV was even higher in rats chronically treated with L-NAME. This additional decrease in aortic compliance might be due to the remodeling of the vascular wall, caused by the chronic NO synthase inhibition and hypertension [60].

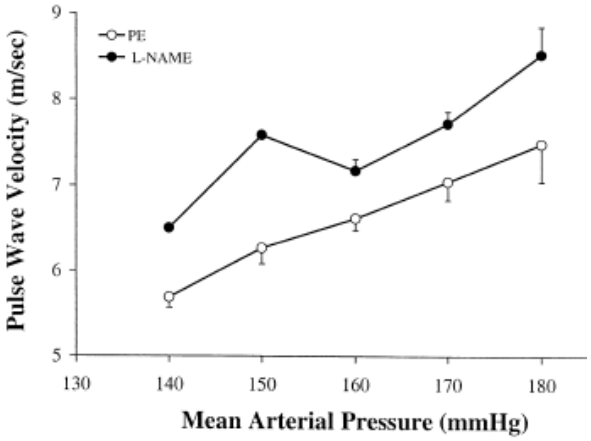

Figure 4.3: *Pulse wave velocity versus mean arterial blood pressure [60].*

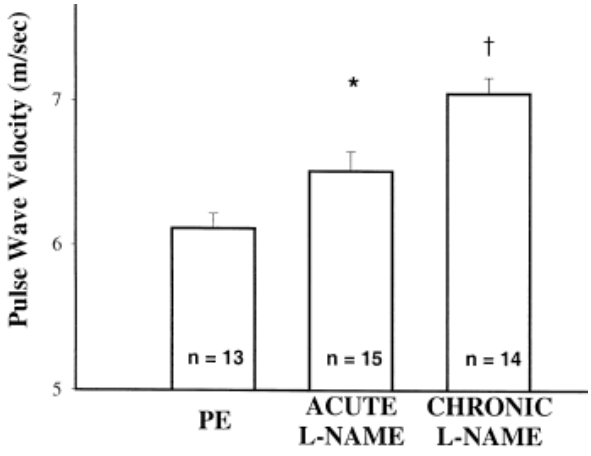

Figure 4.4: *Effect of phenylephrine (PE) and acute or chronic L-NAME treatment on pulse wave velocity when mean arterial blood pressure was normalized (at MAP 150 mmHg) [60].*

In 2002, A. Braun et al., from the Department of Biology at the Massachusetts Institute of Technology (Cambridge), carried out a hemodynamic analysis (catheter) in ApoE-KO (n=15, 6 weeks old) and dKO (n=13, 5 weeks old) mice. As expected, all of the dKO mice died by 8 weeks of age (50% mortality at 6 weeks) [88].

The study revealed that aortic systolic blood pressure and heart rate (HR) were significantly lower in dKO than in control mice. Besides, dKO mice showed LV systolic dysfunction, due to the lower LV systolic pressure and contractility (+dP/dt), and impaired LV relaxation due to a similar reduction in -dP/dt. Although reduced HR might have contributed to reduced blood pressure and contractility, it is unlikely that these relatively small baseline differences caused the large changes in both +dP/dt and -dP/dt. Furthermore, similarly as in humans with heart disease, anesthesia could induce substantial conductance abnormalities (e.g., brady-arrhythmias and AV blocks) in dKO mice [88].

In 2003, A. K. Reddy et al. accomplished a new study to determine whether arterial stiffening occurred with age in male mice as it does in humans. The group determined aortic input impedance spectra, pulse wave velocity, and augmentation index in mice at the age of 8 and 29 months. Pressure and blood velocity signals were measured simultaneously from the same location in the ascending aorta. Blood velocity was measured non-invasively with a Doppler probe while pressure was obtained using a catheter. As results, characteristic impedance, pulse pressure and augmentation index, as well as aortic pulse wave velocity, were higher in old mice [126, 127].

Augmentation index, which allows to assess the early pressure wave reflection, was calculated by dividing change in pressure (ΔP) by pulse pressure (PP). Aortic pressure signals of an adult and an old mouse are shown in figure 4.5. These results were also similar to those reported in humans, confirming that mice can be used as models of age-related vascular stiffening [126].

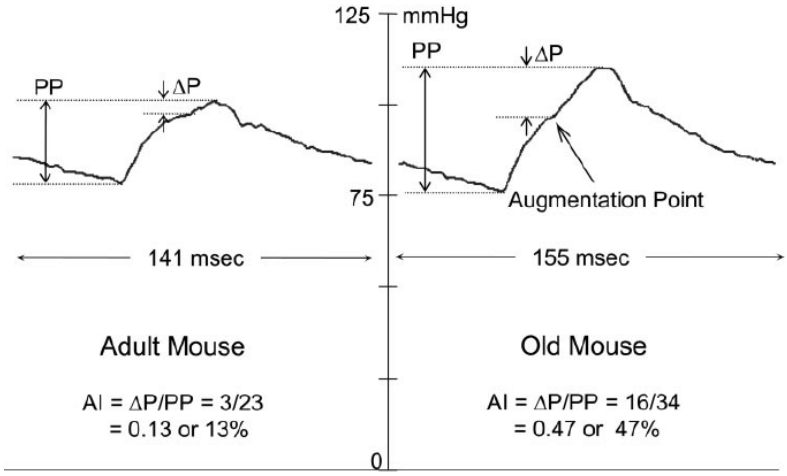

Figure 4.5: *Calculation of AIx from aortic pressure signals of an adult and an old mouse [126].*

Aortic input impedance modulus was calculated by dividing pressure modulus by velocity modulus at each frequency or harmonic. It incorporates the pulsatile and the steady components of the hydraulic load from the left ventricle, providing a more complete description of the load by including factors related to aortic stiffness. The impedance modulus and phase of 5 adult and 6 old mice are plotted versus harmonics in figure 4.6.

At first harmonic, the impedance was significantly higher in old mice due to an early return of wave reflections from peripheral sites. The first minimum of the impedance modulus shifted from the second harmonic in young mice to the forth harmonic in old mice. This allowed the group to characterized the effects of aging on aortic stiffness by means of the aortic input impedance in mice. Besides, these plots beared resemblance to those from humans in magnitude and harmonic number [126].

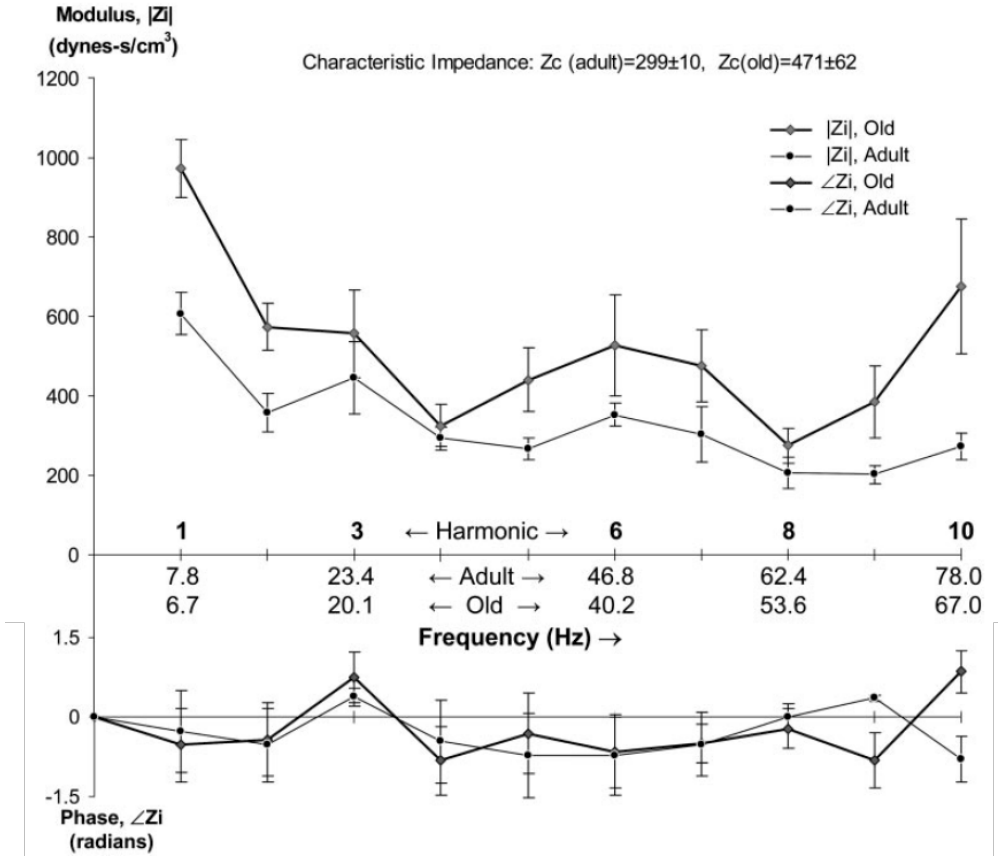

Figure 4.6: *Modulus and phase of ascending aortic input impedance in adult and old mice versus the harmonic number [126].*

Characteristic impedance (Z_C) was estimated by averaging from the second to the tenth harmonic of the impedance moduli. Besides, they approximated Z_C as the product of the PWV and blood density. Z_C and PWV increased significantly with age in mice indicating the stiffening of the aorta. However, differences were not significant between adult and old mice (figure 4.7). Both parameters behaved similar as they would do in humans [126, 127].

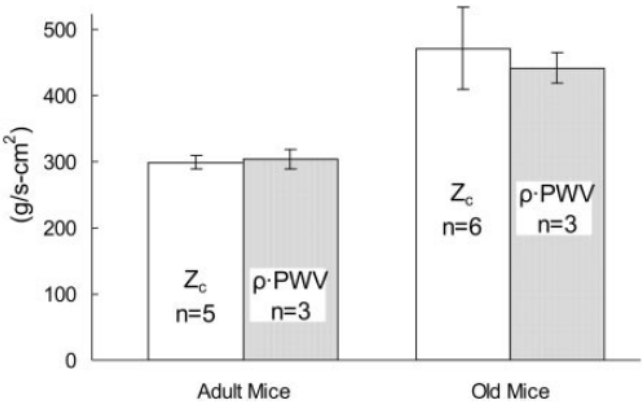

Figure 4.7: *Characteristic impedance and product of blood density and PWV [126].*

Also in 2003, the group of K. Kazama et al., from the Department of Neurology and Neuroscience at the Weill Medical College of Cornell University (New York), investigated whether angiotensin II (ANGII) could alter the coupling between synaptic activity and cerebral blood flow (CBF) in mice [98]. To do this, the group measured the response of CBF, using laser-Doppler flowmetry [128], produced by neural activity. A group of wild type mice, who received an intravenous infusion of ANGII, was compared to wild type controls (saline infusion).

However, ANGII is known to contribute to the genesis of hypertension [98]. Hypertension is highly related to cerebrovascular events and chronic disorders affecting cognitive function, like vascular cognitive impairment or dementia [129]. It alters the structure of cerebral vasculature [130] and is able to alter functional adaptive mechanisms of brain vessels [131]. In humans, it has been reported that hypertensive patients suffer from alterations in resting CBF, reflecting an increase in cerebrovascular resistance [131].

In the experiment, a group of WT mice received an infusion of a saline solution or vehicle (n=5) after which whisker stimulation increases CBF as it would do in anesthetized mice. A second group of WT mice (n=5) received an intravenous ANGII infusion. ANGII induced an increase in mean arterial pressure (MAP), as shown in figure 4.8.A without affecting resting CBF, as shown in figure 4.8.B (values are means $\pm$ SE, *$p < 0.05$). On the contrary, it attenuated the CBF increase produced by whisker stimulation by 65%, figure 4.8.C. However, despite it attenuated the increase in somatosensory cortex blood flow produced by facial whiskers stimulation, it did not attenuate the CBF increase produced by hypercapnia, figure 4.8.D. [98]. Hypercapnia refers to abnormally elevated carbon dioxide (CO2) levels in the blood. It induces cerebral vasodilation and increases cerebral blood flow (CBF) [132]. The group established that ANGII attenuates functional hyperemia, i.e. the increase of blood flow, and thus, it can attenuate the increase in CBF produced by somatosensory activation. However, the mechanical effect of hypertension on cerebral blood vessels is unlikely to be the reason for this behaviour, since the attenuation in functional hyperemia persists even if MAP is kept at a low level. Probably, the most likely reason is that ANGII interferes with the vascular action of the mediators responsible for the increases in CBF evoked by neural activity. The attenuation of functional hyperemia could alter the effect of hypertension on the central nervous system leading to brain dysfunction [98].

In 2004, the group of C. J. Hartley et at. measured the arterial wall motion in different mice models, in order to identify important changes in arterial properties associated with age, atherosclerosis, and the absence of vascular tone [133]. For the study, sixteen mice were used: 6 WT, 2 ApoE, 4 αSMA, and 4 thirty month old (Old) mice. Figure 4.9 shows diameter signals and illustrates the range of amplitudes as well as wave shapes from carotid arteries for each type of mouse. Differences can be seen in magnitude and shape of diameter waves, and in heart rate [133]. As results, total wall displacement happened to be lowest in an ApoE mouse and highest in an αSMA mouse.

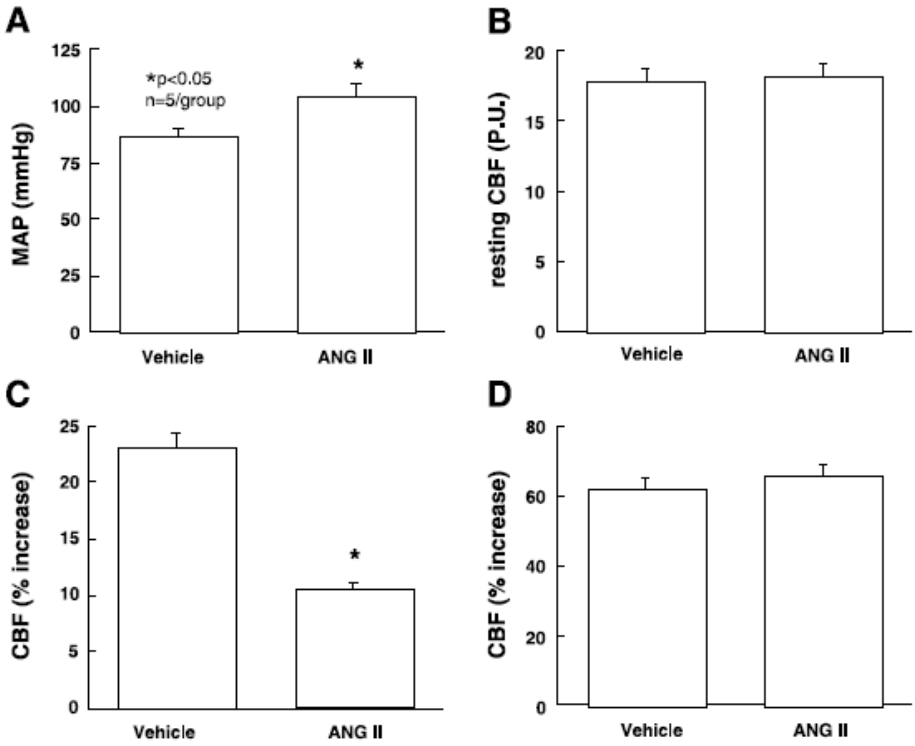

Figure 4.8: *Effect of AngII on mean arterial pressure (MAP) and on selected cerebrovascular responses. ANGII increases MAP (A) but does not affect resting cerebral blood flow (CBF; B). ANGII attenuates the increase in CBF produced by whisker stimulation (C) but not hypercapnia (D). [98].*

Besides, diameter was measured in a WT mouse at the abdominal aorta, iliac arteries and carotid artery as shown in figure 4.10. Results concluded that diameter pulse arrives first in the carotid artery and last in the iliac artery, as expected due to the longer distance. Diameter varies in proportion to the size of the artery, varying the most in the abdominal aorta and the least in the iliac artery. Besides, one can see how pulsations become more damped with increasing distance from the heart [133].

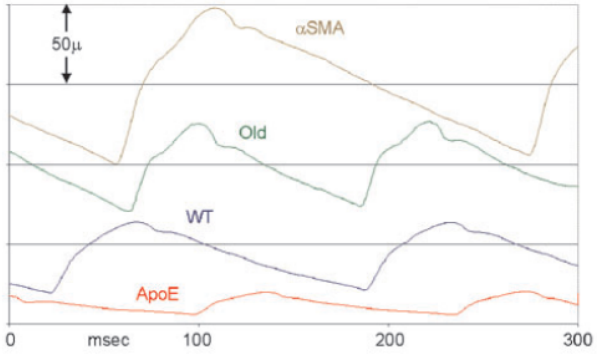

Figure 4.9: *Diameter signals measured at the carotid artery from the four types of mice [133].*

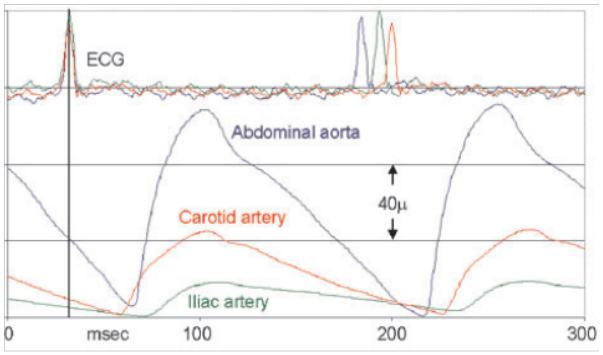

Figure 4.10: *Diameter signals at the abdominal aorta, carotid and iliac artery of a WT mouse [133].*

Furthermore, C. J. Hartley and A. K. Reddy et al. applied the method developed by J. P. Murgo

et al. in 1980 (explained later in section 6.6) to calculate the augmentation index, using diameter signals instead of pressure. Results show that Old and ApoE mice present higher augmentation indexes than normal wild type (figure 4.11), suggesting an earlier arrival of reflections from the periphery in these mice. This age findings in mice are consistent with those in old and atherosclerotic humans. Measurement techniques originally developed for the evaluation of aortic stiffness in humans could be applied in mice, guaranteeing the appropriate interpretation of results [133].

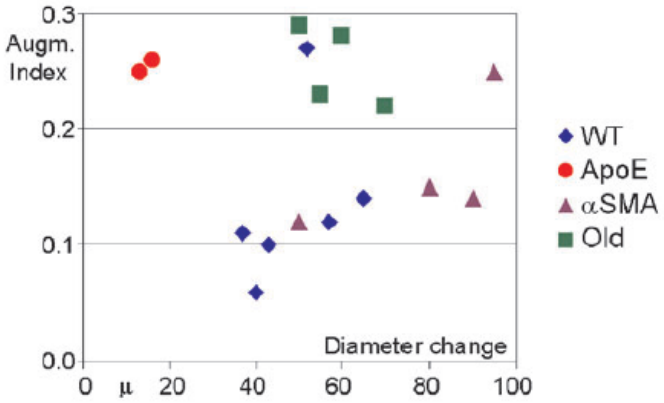

Figure 4.11: *Carotid artery AIx versus net diameter pulsations for the four groups of mice [133].*

A couple of years later, in 2005, the group of Y.-X. Wang demonstrated that treatment of simvastatin, a statin used to lower cholesterol, during 3 months in LDLR-KO mice, a model of hyperlipidemia and atherosclerosis, significantly decreased total cholesterol levels. This effect was accompanied by a significant reduction in atherosclerotic lesions in the aorta (figure 4.12). However, the opposite behaviour was found in ApoE mice. Statins are commonly used as lipid lowering agents and have been shown to reduce cardiovascular morbidity and mortality in patients with atherosclerosis, as well as the incidence of Alzheimer's disease [134].

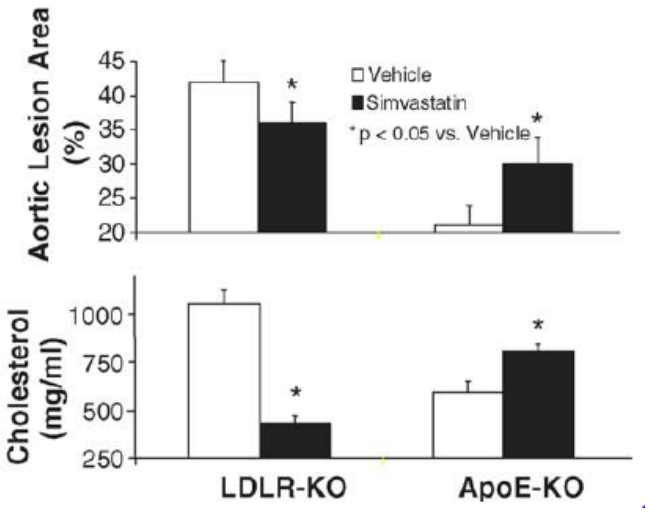

Figure 4.12: *Opposite effects of simvastatin in LDLR-KO and ApoE-KO mice [53].*

The group also showed that chronic infusion of angiotensin (ANGII) promoted vascular

inflammation, accelerated atherosclerosis development and induced abdominal aortic aneurysm (AAA) in ApoE-KO mice. ANGII increased aortic stiffness measured by PWV in both ApoE-KO mice and C57BL/6 wild type controls, as shown in figure 4.13 [53]. They also demonstrated an age-dependent cardiac hypertrophy as well as an increase in cardiac output, measured by aortic flow velocity peak using non-invasive Doppler method, in old (13 months) ApoE-KO mice compared to C57BL/6 wild type controls (figure 4.14).

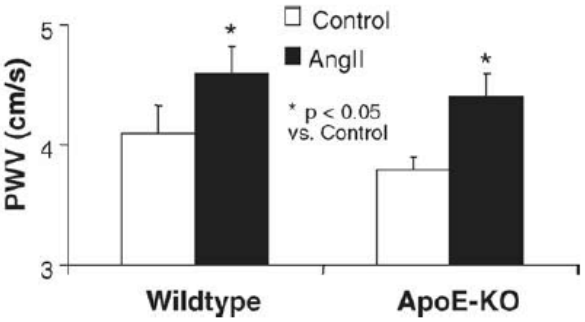

Figure 4.13: *Angiotensin II increased aortic stiffness measured by PWV in ApoE-KO mice and WT controls [53].*

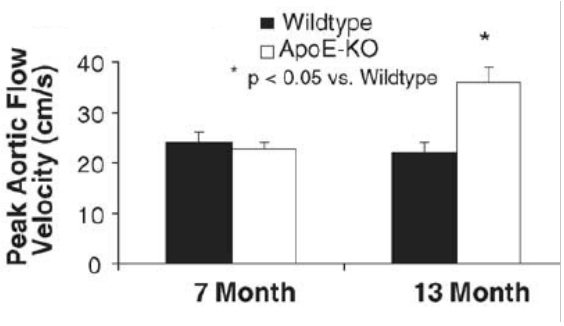

Figure 4.14: *Increase in cardiac output in ApoE-KO mice compared to C57BL/6 wild type controls. Adapted from [53].*

Besides, the group also observed an anti-atherosclerotic effect of estrogen, since it would attenuate atherosclerosis in ApoE-KO, even when accelerated by ANGII, hyperglycemia, or L-NAME [53].

Unlike the elevated PWV in ApoE mice when comparing them with age-matched WT mice, these changes are not always apparent during rest in other mouse models. For instance, in smooth muscle actin knockout (α-SMA$^{(-/-)}$) mice [90], the resting PWV is slightly lower than in WT mice. In 2005, the group of A. K. Reddy et al. proved that even with an intravenous injection of phenylephrine, which in WT mice doubles PWV from 4.6 to 9.9 m/s, this response is absent in α-SMA$^{(-/-)}$ mice [135] (shown in figure 4.15). In contrast, matrix GLA protein knockout mice [95] had significantly elevated PWV (10.4 m/s) even at rest [135].

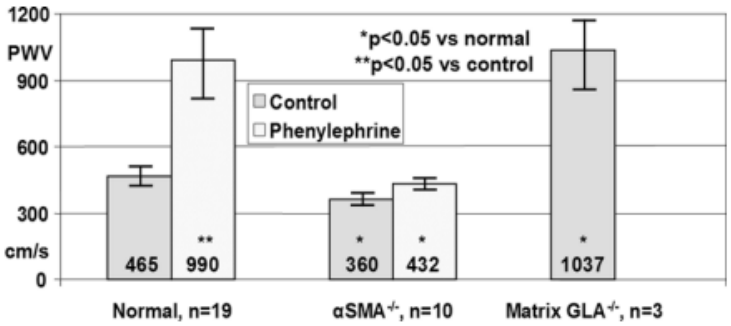

Figure 4.15: *Pulse wave velocity in normal (wild type) and transgenic mice (α-SMA$^{(-/-)}$ and Matrix GLA protein knockout) [135].*

In 2009, the CMR method developed by the team of V. Herold and M. Parczyk et al. was applied to measure PWV in a transgenic group of five 8 month old apolipoprotein E deficient

ApoE$^{(-/-)}$ mice and an age-matched group of four C57BL/6 mice. During 10 weeks before the MR measurements, ApoE$^{(-/-)}$ mice were fed with a high cholesterol diet. The mice were anesthetized during the MR experiments with PWV values measured at both locations, ascending and abdominal aorta. PWV values were higher in ApoE mice compared to controls. However, PWV measurements in WT mice compared at the different ages, 2 months and 8 months, did not show statistically significant differences. Likely, the high cholesterol diet was the reason for the accelerated arterial wall thickening in ApoE mice. The increase in the cross-sectional area would lead to atherosclerotic lesions, explaining the high PWV values in this strain [34].

In 2010, the team from Würzburg (M. Parczyk et al.) performed MR measurements in 8 month old female mice. For the study, they compared a group of ApoE$^{(-/-)}$ mice with a second group of C57BL/6 mice. ApoE$^{(-/-)}$ mice seemed to have higher PWV values compared to C57BL/6. Thus, the measured PWV was demonstrated to be a good marker to classify the state of arterial dysfunction in living mice [83].

In 2011, C. J. Hartley et al. applied a new Doppler technique to estimate the left main coronary flow reserve (CFR) in 10 mice before and 21 days after transverse aortic constriction (TAC), figure 4.16. CFR was calculated as the ratio of hyperemic flow (H) during maximal vasodilation to baseline resting flow (B).

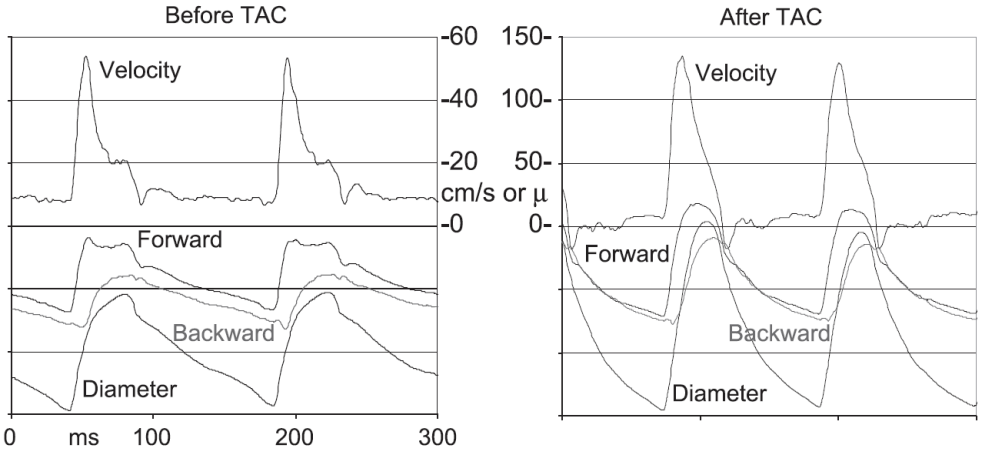

Figure 4.16: *Velocity, diameter change, and forward and backward waves from the right carotid artery of a mouse before and after TAC [4].*

TAC is a common surgical model for creating pressure overload induced cardiac hypertrophy and heart failure [136]. After TAC there was a significant increase in flow during systole, as shown in figure 4.16. The team used diameter instead of pressure and velocity instead of flow to calculate forward and backward waveforms from the measured Doppler signals. They also calculated wave intensity multiplying the derivatives of diameter and velocity, an idea introduced by Niki et al in 2002 [137, 138] (explained later in section 6.5). Although units are different when using diameter instead of pressure, the shapes of the waves and their relative magnitudes are correct. The ratio of the magnitudes of backward to forward waves is similar before and after TAC, although time at which reflected waves arrive is a little shorter after TAC, suggesting that PWV is higher.

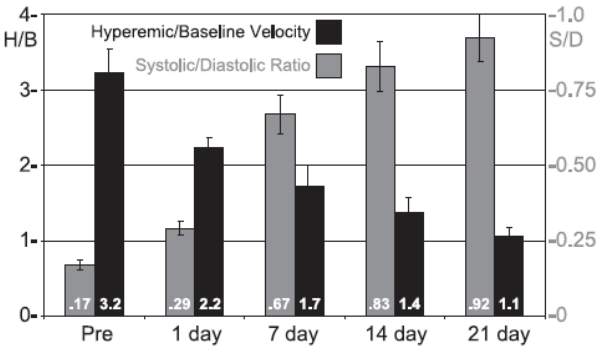

Figure 4.17: *H/B coronary velocity and S/D area ratios before and after TAC [4].*

Cardiac reserve, used as a health indicator, is the difference between the rate at which the heart pumps blood in a certain time and its maximum capacity. Due to the increase in blood flow, CFR (hyperemic/baseline velocity) achieved its maximum level after TAC, and was progressively reduced during the follow-up of 21 days (figure 4.17). For this reasson, it could be used in place of ejection fraction as an index of global cardiac reserve in mice. Besides, the coronary systolic-to-diastolic ratio (S/D) of the spectral velocity signal was also measured. It seemed to be a useful index of myocardial perfusion status since it increased after TAC [4] (figure 4.17).

For the first time, in 2013 the team of R. M. Weisbrod et al., from the Boston University School of Medicine (Massachusetts), showed that arterial stiffness preceded the gradual onset of kidney damage, manifested by albuminuria, cardiac diastolic dysfunction and hypertension, in a mouse model of diet-induced obesity (high-fat-high-sugar or HFHS diet) [139]. This would support the theory that arterial stiffness is a cause, rather than a consequence of hypertension [139].

In comparison to normal diet (ND) mice, HFHS-fed mice significantly increased body weight (BW) and fat mass by 2 months, besides to become glucose intolerant and insulin resistant. Microalbuminuria, an indicator of kidney damage, was significantly increased after 4 months of diet. These observations suggest a role for arterial stiffness as a therapeutic target to treat cardiovascular diseases. Arterial stiffness developed in vivo after one month of the initiation of the diet and preceded the development of hypertension by five months [139].

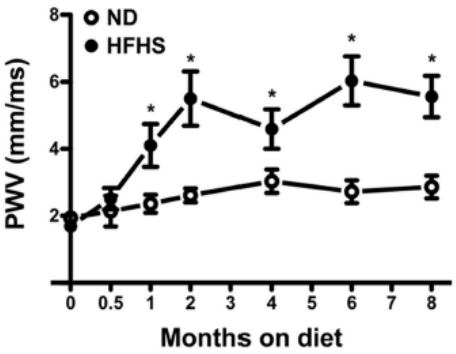

Figure 4.18: *Evolution of PWV (catheters)in HFHS-fed mice verus ND-fed mice [139].*

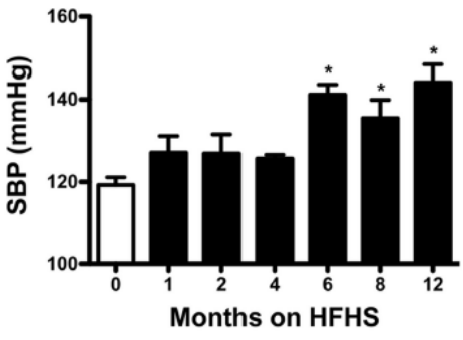

Figure 4.19: *Development of systolic hypertension in HFHS-fed mice [139].*

In order to address the temporal relationship between arterial stiffness and hypertension, young mice (8 weeks old) were followed after starting HFHS for up to one year. PWV measured by Doppler echocardiography increased in 11 HFHS-fed mice within 2 months compared to 9

mice following a normal diet (ND), as illustrated in figure 4.18. After 6 months, there was a statistically significant increase in SBP, PP and MAP, leading to the development of systolic hypertension in HFHS (figure 4.19). Diastolic pressure (DBP) was not significantly different. However, SBP and MAP pressures of obese mice were significantly decreased after reversal to ND, while DBP did not change [139].

Also in 2013, the group of N. Sadekova et al., from the Faculty of Medicine in Montreal (Canada), studied the administration of $CaCl_2$ (calcium chloride) to the carotid arteries in mice. This leads to carotid calcification, allowing the evaluation of the effects of arterial stiffness on the brain of the animals. In total, 22 C57BL/6 male mice between 10 and 12 week old were used for the study [140].

In a group of 11 mice, the effects of periarterial application of 0.3 mol/L $CaCl_2$ on cerebral blood flow pulsatility were studied during 3 weeks after treatment (figure 4.20). CBF pulsatility, previously called increase of CBF, was measured with Doppler optical coherence tomography (OCT). It is related to arterial stiffness and contributes to dysfunction in the brain and kidneys. In the right side of the brain, corresponding to the calcified right common carotid artery, a significant increase in blood speed could be shown. On the contrary, the left side of the brain, corresponding to the intact carotid, did not show a significant increase [140].

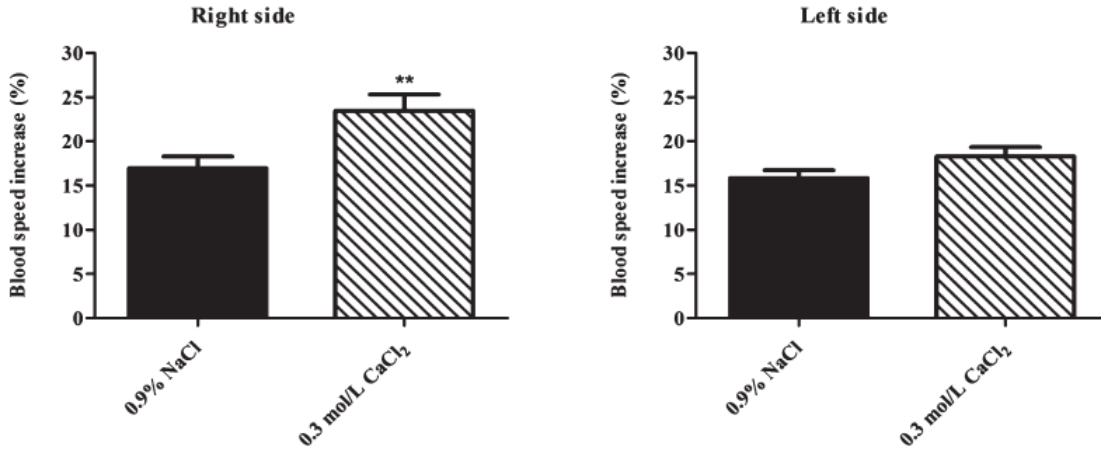

Figure 4.20: *Effects of $CaCl_2$ on CBF pulsatility in the right and the left side of the brain (intact carotid) [140].*

Systolic blood pressure (mmHg) was monitored by a non-invasive tail-cuff method every 4 days from the day of surgery until the end of the treatment, with $CaCl_2$ (14 days). Before surgery, the pressure was similar between both groups, and it remained stable without any increase during the whole treatment period. This confirmed that $CaCl_2$ does not alter blood pressure and that carotid stiffness induced by carotid calcification is the only factor contributing to increased flow pulsatility in the brain. For this reason, arterial stiffness seems to play an important role in the pathogenesis of neurodegenerative diseases [140].

In 2014, A. J. A. Leloup et al. used endothelial nitric oxide synthase knockout ($eNOS^{(-/-)}$) mice in a longitudinal experiment to assess the large artery stiffness with carotid and femoral P tonometers [66]. Compared to WT mice, $eNOS^{(-/-)}$ displayed significantly higher cfPWV. A total of 33 WT and 22 eNOS mice (C57BL/6) were used. Sevoflurane and Nembutal anesthesia were used to immobilize the animals during tonometry measurements. Wild type (WT) mice anesthetized with Nembutal (n=9) had significantly lower cfPWV compared to WT sevoflurane anesthetized mice (n=24), while cfPWV was significantly elevated in sevoflurane-anesthetized $eNOS^{(-/-)}$ mice (n=11) (figure 4.21) [66].

During 12 days, $eNOS^{(-/-)}$ mice (n=5) were treated with perindopril. Vehicle-treated (0.1% ethanol) $eNOS^{(-/-)}$ mice (n=6) served as controls. As result, cfPWV decreased after perindopril treatment of $eNOS^{(-/-)}$ mice while it remained unchanged in vehicle-treated $eNOS^{(-/-)}$ mice (figure 4.22) [66].

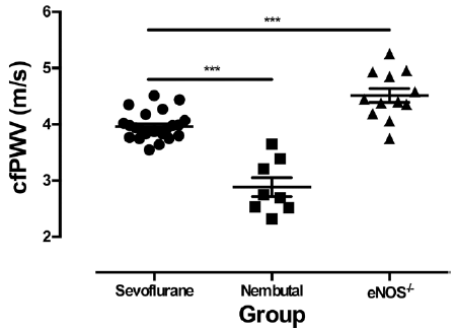

Figure 4.21: *Applanation tonometry–based cf-PWV assessment of known models with altered aortic PWV [66].*

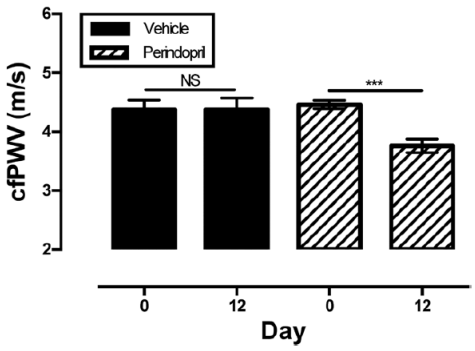

Figure 4.22: *Pharmacological alteration of cf-PWV in a longitudinal experimental setup [66].*

In 2015, the group of D. Cifuentes et al., from the Institut des Vaisseaux et du Sang, Paris (France), combined an Alzheimer's disease (AD) mice model with hypertension (HT). AD, also known as senile dementia of the Alzheimer type, is a chronic neurodegenerative disorder characterized by the development of cortical extracellular amyloid plaques, mainly amyloid β peptide (Aβ), resulting in memory dysfunction [141, 142]. In the study, the group analyzed the effects of ANGII treatment on vascular patterns, neuropathology, and the behavior of the mice in memory tasks [101].

ANGII infusion was administrated in 2 month old mice during 2.5 months via subcutaneously implanted osmotic minipumps. Four experimental groups were analyzed: control (WT) C57BL/6 mice; ANGII-treated or hypertensive C57BL/6 mice (HT); APPPS1 or Alzheimer mice (AD); and ANGII-APPPS1 mice (AD&HT). At 2 months, there was no significant difference of SBP between WT and AD mice. ANGII treatment resulted in a rapid raise in SBP (figure 4.23) in both HT and AD&HT mice, which lasted until the end of experiment [101].

Besides, AD&HT mice showed significantly impairment of temporal order memory performance

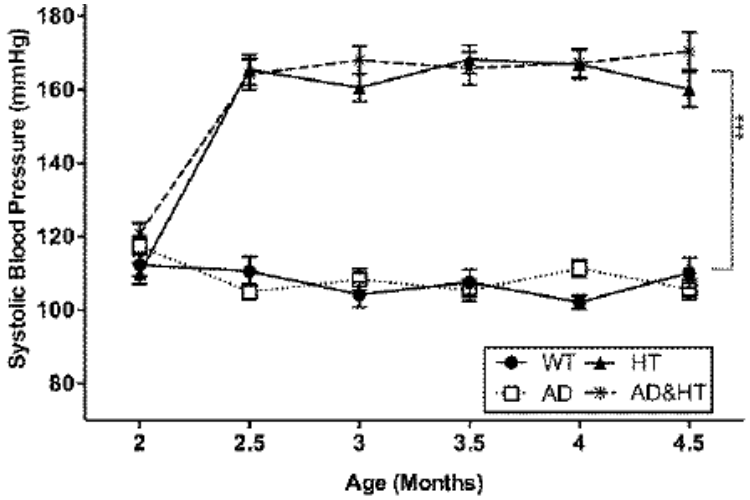

Figure 4.23: *Evolution of SBP in C657BL/6 and APPPS1 mice during ANGII treatment through minipumps [101].*

at the age of 4.5 months compared to both WT and HT mice (figure 4.24), who spent more time exploring the old familiar than recent familiar objects. The results obtained demonstrate that hypertension can cause cerebral vasculature impairment, which accelerates the development of structural and functional alterations related to Alzheimer disease in AD&HT mice [101].

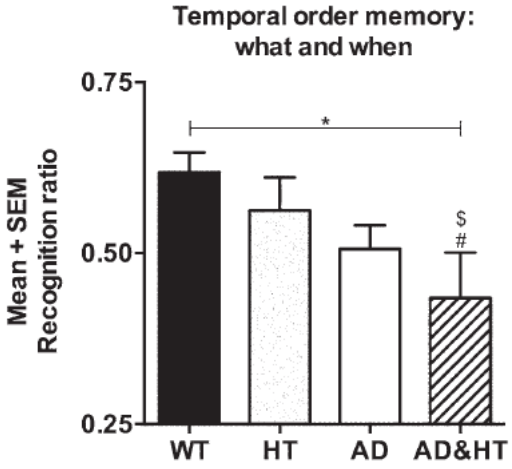

Figure 4.24: *Memory test in different mice [101].*

The team of J. C. Kohn et al. [106], from the Meinig School of Biomedical Engineering at the Cornell University (Ithaca), obtained PWV readings (Doppler US, TT abdominal and thoracic aorta) before and after exercise treatment in mice (C57BL/6 male).

They carried out different studies, one with aged mice (18 month old, n=15 mice) and young mice (2 month old, n=14 mice), and another one with one group with sedentary mice and another after performing an exercise (20 month old, n=7 mice). The data confirmed reports from others indicating PWV increases with age as well as with increasing arterial stiffness, and decrease with exercise in rodents (figure 4.25) [63].

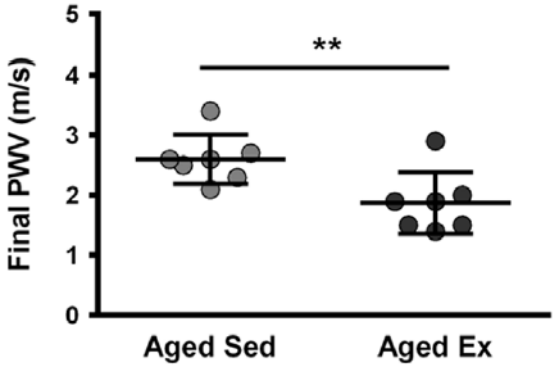

Figure 4.25: *PWV measurements in aged-sedentary and aged-exercised mice after exercise regimen [106].*

In 2016, the high-resolution echocardiography study carried out by the group of N. A. Lee et al., with members from different universities and institutes in Vancouver, Canada, used B-mode and Doppler-mode blood flow velocity images of the aortic arch to demonstrate that the increased PWV (TT method) in Marfan syndrome (MFS) mice is likely based on a loss of aortic elastin fibril organization and integrity [97].

The method applied was relatively simple, with no need of simultaneous blood pressure measurements or assumptions about Doppler angle to obtain flow volumes, and focused on localizing the distance of the aortic root which is the most important locus for the MFS characterization. In the study, Aortic PWV of WT and MFS mice from two age groups (6-8 months and 12-16 months group) was calculated [97]. PWV was significantly increased in 6-8 months MFS mice compared to WT and in 12-16 months MFS mice compared to WT. In MFS mice, PWV was directly proportional to age (figure 4.26) [97].

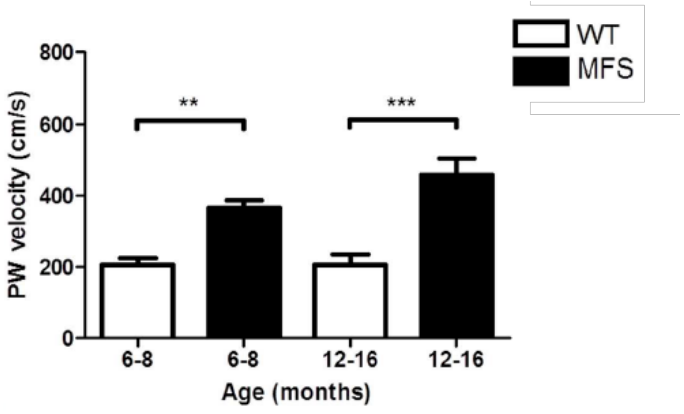

Figure 4.26: *Pulse wave velocity (PWV) of aortic arch in mice: WT versus MFS [97].*

Also in 2016, M. Wiesmann et al., from the Radboud University Medical Center in Nijmegen (The Netherlands), studied the effects of hypertension after two months of angiotensin II (ANGII) infusion in wild-type and AβPP/PS1 mice. High doses of angiotensin II cause hypertension and affect cerebral blood flow contributing to Alzheimer's disease [99].

For the experiment, a total of 51 mice were used, all of them 10 month old and male, divided in 29 WT and 22 AβPP/PS1 mice. Mice of both models were split in a group of hypertension (AngII-infusion) and a group of controls (saline infusion). After one month of induced hypertension, AβPP/PS1 showed higher SBP than wildtype mice. AngII and saline infusion groups were further divided into two subgroups: treatment with angiotensin II receptor blockers, eprosartan mesylate (EM), and standard drinking water as control [99].

Eprosartan treatment restored the systolic blood pressure in all mice. CBF was acquired in two standardised gas concentrations: normal and vasoconstriction. Under both conditions, untreated AβPP/PS1 mice showed a decreased cortical CBF (figure 4.27.a), calculated from MRI measurements, compared to WT mice. Functional connectivity (FC), estimated also from magnetic resonance imaging measurements, was decreased in both groups of mice. Treatment with EM under normal gas concentration increased hippocampal CBF in ANGII- and Sal-infused groups (figure 4.27.b) [99].

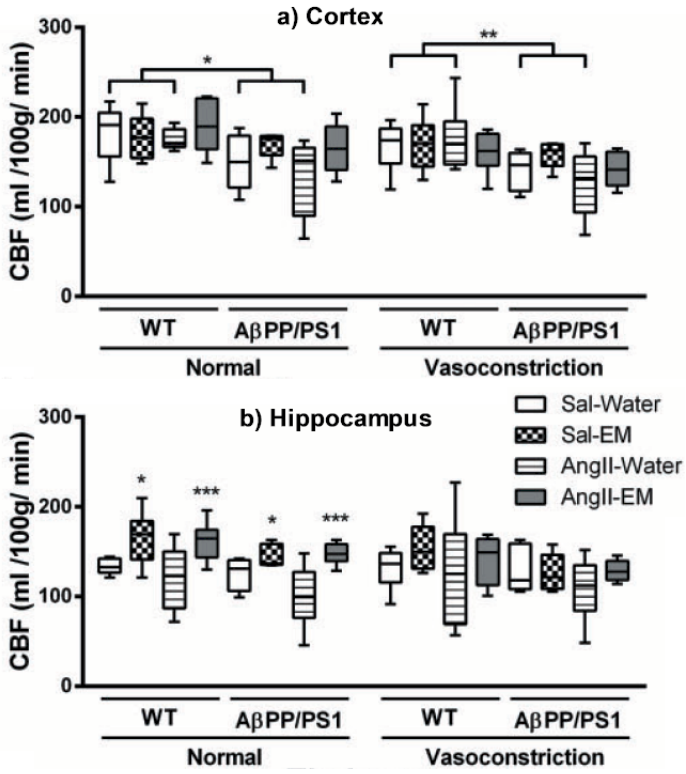

Figure 4.27: *Cerebral blood flow (CBF) measurements in WT and AD mice normal and under vasoconstriction [99].*

These results suggest that hypertension exacerbated Alzheimer's disease's pathological symptoms (impairment of CBF, FC, and cognition) in Alzheimer's disease model mice. Furthermore, it also contributed to decrease FC in WT mice, leading to cognitive decline or dementia, but not necessarily inducing the AD pathology. However, the study revealed that the elevated levels of ANGII could contribute to the development of AD by affecting cerebral blood flow [99].

In 2017, the group of A. Gotschy et al., also from the University of Würzburg, collaborated with V. Herold and some members of his group. Together, they compared local versus global distribution of early arterial stiffening due to initial atherosclerotic lesions. A TT method was used to determine the global PWV in the murine aorta. Furthermore, local aortic stiffness was measured by assessing the local PWV in the upper abdominal aorta by the QA method. The measures were taken in ApoE$^{(-/-)}$ and wild type (WT) mice using ultrahigh field MRI.

Within the WT group, global and local PWV correlated well in the upper abdominal aorta, implying a widely uniform arterial elasticity. However, ApoE$^{(-/-)}$ mice behaved in a different way and showed significantly higher PWV. The experimental results demonstrate that vascular stiffening caused by early atherosclerosis is unequally distributed over the length of large vessels [121].

Also in 2017, N. D. Lascio et. al. applied the image process algorithm developed in 2014 [63], based on the lnD-V loop, for assessing carotid PWV in mice. The heart and the carotid artery were imaged with high-resolution ultrasound (US) at 40 MHz. The group published age-associated changes in parameters derived from wave intensity analysis (WIA) like W1, W2, Wb, the negative area between W1 and W2 (NA) or the reflection index (RI, ratio between Wb and W1) [6].

The technique was applied in sixteen wild-type male mice, at 8 (T0) and 25 weeks (T1) of age. Some cardiac parameters as the cardiac output, and parameters derived from carotid artery images (Ds, Dd, Dm, reID, PWV, V_p) were calculated for all animals at both time points. For each time point, wave intensity analysis was performed and WIA-derived indexes (W1, W2, Wb, NA, RI) were assessed [6].

After evaluation, the study reveled a decrease with age of parameters like W1, W2, Wb, CO, HR, reID, V_p, Dd. No differences were found for Dm, PWV or RI. The decrease in W1 and W2 would suggested a cardiac performance reduction (i.e. age-associated alterations in the arterial–ventricular interaction). The decrease in the absolute value of Wb, considering unchanged RI, indicates an energy decrease of refected waves induced by the decrease in the magnitude of forward waves reflected by W1 [6]. These cardiac and vascular parameters' values at T0 and T1 are presented in table 4.2, together with the results of the statistical analysis (Wilcoxon rank test) to evaluate differences between them.

W1 was significantly correlated with CO at T0, though this correlation was lost at T1. At both T0 and T1, NA values were correlated with V_p measurements [6]. Previous studies in both humans and animals have shown that the W1 amplitude is directly correlated to the maximum rate of pressure rising during left ventricular (LV) ejection, and it is considered a representative parameter of LV systolic performance [6].

Cardiovascular research in mice is summarized in table 4.3.

	T_0 (8 weeks)	T_1 (25 weeks)
HR (bpm)	403 ± 94	346 ± 40*
RR (bpm)	122.33 ± 20.92	108.50 ± 22.424
T (°C)	35.32 ± 0.73	34.92 ± 0.59
LVmass (mg)	107.36 ± 10.29	119.10 ± 14.23*
CO (mL/min)	19.27 ± 4.33	16.71 ± 2.88*
D_m (mm)	0.45 ± 0.03	0.47 ± 0.04
D_s (mm)	0.50 ± 0.04	0.51 ± 0.04
D_d (mm)	0.39 ± 0.03	0.42 ± 0.04
relD (%)	27.4 ± 5.51	21.86 ± 3.95†
PWV (m/s)	1.06 ± 0.29	1.02 ± 0.27
V_p (cm/s)	50.24 ± 15.02	38.61 ± 10.88*
W_1 (m^2/s)	4.42e-7 ± 2.32e-7	2.21e-7 ± 9.77e-8†
W_2 (m^2/s)	2.45e-8 ± 9.63e-9	1.78e-8 ± 7.82e-9*
W_b (m^2/s)	−8.75e-8 ± 5.45e-8	−4.28e-8 ± 2.22e-8†
NA (m^2)	5.59e-10 ± 2.97e-10	2.85e-10 ± 1.41e-10†
RI	0.20 ± 0.08	0.20 ± 0.06

Table 4.2: *Cardiac, vascular and WIA-derived parameters at both T0 and T1 [6].*

Author Year (Ref.)	Study design	Animal	Animal model	Sample Size/Sex/Age	Technology	Parameters (method)	Main result	Conclusion
Hartley et al. 2000 [25]	CS	Mice	G1:ApoE G2:WT	n_1:10/-/13m n_2:10/-/13m	Doppler US	PWV (TT), V, A2/A1 ratio	Significant increases in A2/A1 ratio, PWV and aortic and mitral V in old ApoE, but normal HR and BP compared to WT.	ApoE mice have been proven to develop vascular stiffening, and can be used as models of atherosclerosis.
Fitch 2001 [60]	L: L-NAME (3w) and PE (3w)	Rats	G1:WT(PE,3w), G2:WT(L-NAME, 3w), G3:WT(L-NAME, chronic)	n_1:13/M/- n_2:15/M/- n_3:14/M/-	Catheter	PWV (TT), MAP	Increase in PWV by L-NAME over PE, which increases MAP. Inhibition of NO production (L-NAME) increases PWV.	NO withdrawal reduces aortic compliance independently of BP changes.
Braun et al. 2002 [88]	L: standard chow diet	Mice	G1:ApoE, G2:dKO	n_1:15/-/6w, n_2:13/-/5w	Catheter and ECG	SBP and HR	dKO shows lower SBP and HR than controls. Arrhythmias and AV blocks as consequence of anesthesia.	dKO can be used to study the role of atherosclerosis in the pathogenesis of MI and cardiac dysfunction.
Reddy et al. 2003 [126]	CS	Mice	WT	G1:n_1:5/M/8m, n_2:6/M/29m, G2:n_3:3/M/8m, n_4:3/M/29m	Doppler-US	Z_C, AIx, PP, V	Z_i, Z_C, PP, AIx (G1) and aortic PWV(G2) higher in old mice.	Arterial stiffening increases with age in mice similar as it does in humans.
Kazama et al. 2003 [98]	CS	Mice	G1:WT(saline inf.) G2: WT(ANGII inf.)	n_1:5/-/-, n_2:5/-/-	Tail-cuff, Doppler (V)	MAP, CBF	ANGII infusion increased MAP values and attenuated the increase in CBF (hyperemia) evoked by neural activity.	ANGII seems to interfere between vascular and neural activity, what could lead to brain dysfunction. ANGII administrated mice can be used as HT mouse models.
Hartley et al. 2004 [133]	CS	Mice	G1:WT, G2:ApoE, G3:α-SMA, G4:WT Old	n_1:6/-/3-5m, n_2:2/-/-, n_3:4/-/-, n_4:4/-/30m	Doppler	D, AIx	Lowest wall displacement in ApoE, highest in an αSMA. Old and ApoE had higher AIx than WT.	Findings in mice consistent with those in old and atherosclerotic humans.

Author Year (Ref.)	Study design	Animal	Animal model	Sample Size/Sex/Age	Technology	Parameters (method)	Main result	Conclusion
Wang et al. 2000 [82]	CS	Mice	G1,G2:ApoE G3,G4:WT	n_1,n_3:6/-/4m n_2,n_4:8/-/13m	Catheter (MAP, SBP, DBP, PP)	PWV (TT) and EDNO levels	Old ApoE: higher PWV, smaller EDNO mediated vasorelaxation (ACh).	The lack of EDNO is involved in the development of atherosclerosis, linked to an increase in PWV.
Wang et al. 2005 [53]	CS	Mice	G1,G2:ApoE G3,G4:WT	n_1,n_3:-/-/4m n_2,n_4:-/-/13m	Catheter and Doppler-US	PWV (TT)	Ang II promoted vascular inflammation, atherosclerosis (as L-NAME, opposite to estrogen) and AAA in ApoE mice.	Pharmacological responses allow detection of new cardiovascular functional phenotypes in ApoE mice.
Herold et al. 2009 [34]	CS	Mice	G1:WT, G2:ApoE (fat diet, 10w)	n_1:5/-/2m&8m, n_2:9/-/8m	PC-MRI	Local aortic PWV (QA)	Higher PWV (both locations) in ApoE mice. No big PWV differences for 2 and 8m old WT.	Cholesterol diet accelerates arterial wall thickening in ApoE (higher A), leading to atherosclerotic lesions.
Parczyk et al. 2010 [83]	CS	Mice	G1:ApoE (western diet, 10w), G2:WT	n_1:5/F/8m, n_2:4/-/8m	CMR	Regional PWV (TT)	PWV higher in ApoE than in WT mice.	PWV is an important marker of arterial dysfunction in mice.
Hartley et al. 2011 [4]	L: 21d after TAC	Mice	WT (Stenosis)	n:10/-/-	Doppler US	PWV (TT), CFR (H/B), S/D, WI, V, D	Nearly abolished CFR after 21 days of aortic constriction (TAC), while S/D ratio increases.	CFR can be used as an index of global cardiac reserve in mice, and S/D as an index of myocardial perfusion status.
Weisbrod et al. 2013 [139]	L: 1y after HFHS diet	Mice	G1:WT (HFHS) G2:WT (ND)	n_1:11/F/8w, n_2:9/-/8w	Doppler	SBP, PWV	Arterial stiffess developed after 1 month of diet, fat mass after 2, microalbuminuria after 4 and hypertension after 5 (reverse if back to ND).	Arterial stiffness preceded the gradual onset of kidney damage in HFHS-fed mice.

Author Year (Ref.)	Study design	Animal	Animal model	Sample Size/Sex/Age	Technology	Parameters (method)	Main result	Conclusion
Sadekova et al. 2013 [140]	L: $CaCl_2$, 2w.	Mice	G1:WT ($CaCl_2$) G2:WT (NaCl),	n_1:11/M/10-12w, n_2:11/M/10-12w	Tail-cuff, Doppler-OCT	SBP, CBF changes	CBF pulsatility increased in right side of the brain (common carotid artery calcified). SBP remained stable.	Arterial stiffness induced by carotid calcification is the only factor contributing to increased CBF pulsatility.
Leloup et al. 2014 [66]	L: perindo-pril(12d, G1), ethanol (12d, G1)	Mice	G1:eNOS (sevo. anes.) G2:WT (sevo., nembu.)	n_1:22/-/-, n_2:33/-/-	Applanation tonometry	cfPWV	eNOS: cfPWV fell with perindopril (n=5), not with ethanol (n=6). eNOS (n=11, sevoflurane) sign. higher cfPWV than WT. WT: nembutal (n=11) sign. lower cfPWV than sevoflurane WT (n=24).	The assessment of cfPWV allows characterizing large artery stiffness in mice and analyze effects of anesthesia (nembutal, sevoflurane).
Cifuentes et al. 2015 [101]	CS	Mice	G1:WT, G2:HT (ANGII, 2.5m), G3:AD, G4:AD&HT (ANGII, 2.5m)	n_1=n_2=n_3=n_4:12/M/4.5m	Tail-cuff	SBP	Rapid raise in SBP after ANGII treatment in HT and AD&HT mice. High impaired performance in AD&HT mice.	Hypertension accelerates the onset of cognitive decline in AD&HT mice.
Kohn 2016 et al. [106]	L: exercise (8w)	Mice	G1:WT, G2:WT	n_1:14/M/2m, n_2:15/M/18m	Doppler US/ PWV	PWV	Non-uniform stiffening with age: heterogeneity reversible with exercise.	Clinical evaluation of the artery (PWV) could provide information about subendothelial matrix mechanics.
Lee 2016 et al. [97]	CS	Mice	G1:MFS, G2:WT	n_1:8/-/6-12m, n_2:8/-/6-12m	Doppler (US) and OCT	PWV	The PWV was significantly higher in MFS vs. WT, and increased with age in MFS mice only.	PWV measured in the aortic arch allows the detection of the Marfan syndrome pathology in mice.

Author Year (Ref.)	Study design	Animal	Animal model	Sample Size/Sex/Age	Technology	Parameters (method)	Main result	Conclusion
Wiesmann 2016 et al. [99]	L: ANGII and EM	Mice	G1:WT G2:AβPP	n_1:29/M/10m n_2:22/M/10m	MRI	SBP, CBF	ANGII increased SBP in WT and AD mice and decreased CBF in AD mice. EM treatment restored SBP and increased CBF.	Elevated ANGII causes hypertension (reduction in FC) and contributes to Alzheimer's disease by affecting CBF.
Gotschy et al. 2017 [121]	CS	Mice	G1:ApoE (cholest. diet, 14w), G2:WT	n_1:8/F/18w, n_2:8/F/18w	MRI/ PWV	Local PWV (QA); global PWV (TT)	WT: global and local PWV correlated in upper abdominal aorta; uniform arterial elasticity. ApoE: no correlation.	Vascular stiffening (atherosclerosis) unequally distributed among large vessels.
Lascio et al. 2017 [6]	L (T0=8w, T1=25w)	Mice	WT	n:16/M/-	US images (carotid PWV)	WIA: W1,W2,Wb, NA, RI	At T1 lower W1, W2, Wb, NA, no differences for RI or PWV. W1 significantly correlated with CO at T0. NA correlated with V_p at T0 and T1.	The loss of correlation between WIA-derived and cardiac parameters might be due to an alteration in cardiovascular interaction.

Terminology:
* L = longitudinal study design (T0, T1)
* CS = cross sectional study design
* w = weeks, m = months
* G = group
* F = female; M = male;

Table 4.3: *Cardiovascular research in mice.*

CHAPTER 5

Data and Statistical Methods

In this chapter, materials and methods used in the thesis are specified. All the processing operations were performed using Matlab R2015a (The MathWorks, Inc, Natick, Massachusetts, USA).

5.1 Data and Test Cases

For the present study, specific signals are required. Blood velocity and diameter signals are used to calculate WIA-derived parameters. Physiological values and ECG are also measured in order to calculate parameters such as respiration and heart rate. The used datasets have been provided by the clinical partner from the University of Pisa, Department of Clinical and Experimental Medicine (Italy).

Four different datasets have been provided. All mice were placed on a temperature controlled board and examined under anesthesia induction (1.5% isoflurane). Carotid US-images were obtained with a high-resolution Doppler ultrasound imaging system, a non-invasive technique, see section 3.2.1. Single-beat mean diameter and mean velocity instantaneous values were obtained from B-mode and PW Doppler-mode images, respectively. The system used a sampling rate of 800 Hz.

Besides, ECG recordings and other physiological measurements, such as temperature and the respiration signal, have been provided for all mice. Sample frequency for physiological parameters assessment was 8000 Hz.

The first two datasets correspond to a group of male WT mice (n=13), measured at the age of 8 (WT_t0) and 25 (WT_t2) weeks old. The third group (n=10) consists of mice with carotid plaque vulnerability (ApoE), 16 weeks old. Lastly, the forth dataset corresponds to a group of 13 weeks old diabetes (db/db) mice (n=9).

In a first step, the verification of some developed algorithms has been carried out: hear rate, pulse wave velocity and augmentation index algorithms. Values resulting from applying the algorithms to all recordings (all mice, n=45) have been used for this. These values have been compared with values obtained with alternative methods using Bland Altman plots [143], described in section 5.3.

Therefore, three different test cases (TC) have been analysed. In each of them, two different groups of mice have been compared at a time. TC1 has been performed between WT_t0 and WT_t2, to test for changes due to age, as in [6]. WT_t0 and ApoE mice have been compared in TC2 to see the influence of carotid plaque vulnerability. The last test case, TC3, has been performed between WT_t0 and db/db mice to analyze differences in various parameters caused by diabetes.

5.2 Murine ECG Analysis Algorithm

This section contains a brief description of the algorithm for the automatic detection of ECG components, implemented by Caroline Magg [9] and used for the analysis of ECGrecordings in this thesis. In the present study, this algorithm will be refered to as murine ECG algorithm or simply ECG algorithm. It is an adaptation of the one developed by Bachler et al. [144], for human ECG analysis, referred as human ECG algorithm from now on.

The workflow of the algorithm is given in figure 5.1. Further detailed explanations about this algorithm can be found in "Development and evaluation of a Murine ECG Annotation Algorithm", by Caroline Magg [9].

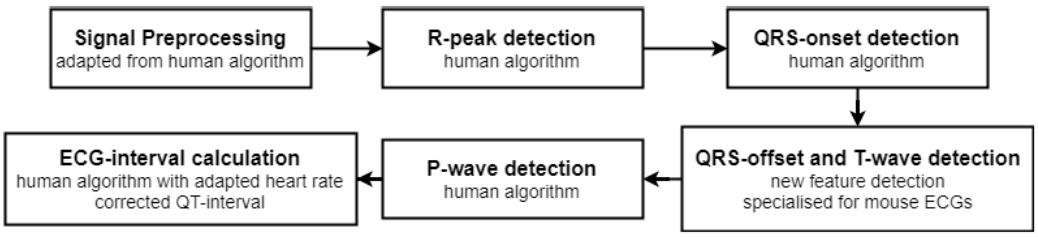

Figure 5.1: *Overview of the processing algorithm for murine ECG signals [9].*

After a first step of signal pre-processing, features are identified. The identification of the r-peak and the QRS-onset are based on the human ECG algorithm, as well as the P-wave detection. However, due to the differences found between human and murine ECG, the detection of QRS-offset and the T-wave is different.

For the r-peak detection, the signal is filtered to remove respiration artefacts. However, for the rest of features a filter is not applied.

Due to the difficulties involved in a separated detection of the J- an the T-wave, the algorithm considers the combination of both as the T-wave. For the QRS-offset and T-wave detection, the algorithm consists of the analysis of a created cluster template and the analysis of each heart beat in the original signal, where the cluster-derived information is used as a reference.

Clustering can be performed by two methods: the kMeans method or a hierarchical method. The hierarchical method has been chosen in this thesis because it allows a variable number of clusters. A cluster template contains less noise since it is created as the median signal of its cluster members. The murine algorithm is prepared to work with 10 seconds segments in order to generate the different templates.

A prominent mimimum after the r-peak is used as reference for the T-onset detection. The detection of the T-peak can be accomplished by two methods, one based in a prominent peak detection and one which uses the "wing" function, also explained in [9]. The first option has been chosen for this thesis.

The T-offset detection can also be performed by two methods: a geometric option and the trapezium or TRA method. Oscillations of the signal between T- and P-wave can influence in the determination of this point as well as in the determination of the P-onset. The geometric method has been used in this thesis.

Figure 5.2 illustrates how the geometric method works. The algorithm establishes a connection line "g" between the QRS-offset and the T-wave. The intersection between a perpendicular line to "g" and the signal itself is the location of the wave offset.

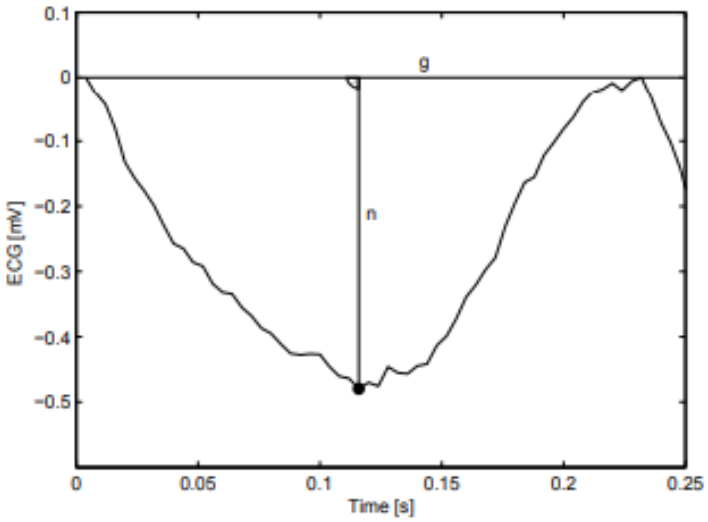

Figure 5.2: *Determination of the T-offset under geometric method. Image adapted from [145].*

In a first detection, the T-offset will be identified as the J-offset. If the T-wave is a clear negative deflection, correction of the T-offset can be applied. This detection is performed by an extension of the trapezium method. In this case, the T-offset is chosen as the intersection between the

baseline and the ECG signal, this is, the end of the negative deflection.

Since the P features depend on the T-offset and the QRS-offset points, if any of them is erroneously identified, the P-onset will probably be misplaced too. This is the reason why the geometric option has been chosen to be used with the datasets provided. The T-offset is earlier detected by the TRA method than by the geometric technique, and therefore, the P-onset is wrongly detected. An example of the preformance of the ECG algorithm in a wild type mouse is shown in figure 5.3, where the T-offset is detected by the geometric method and the TRA method in figures 5.3a and 5.3b, respectively.

(a) **(b)**

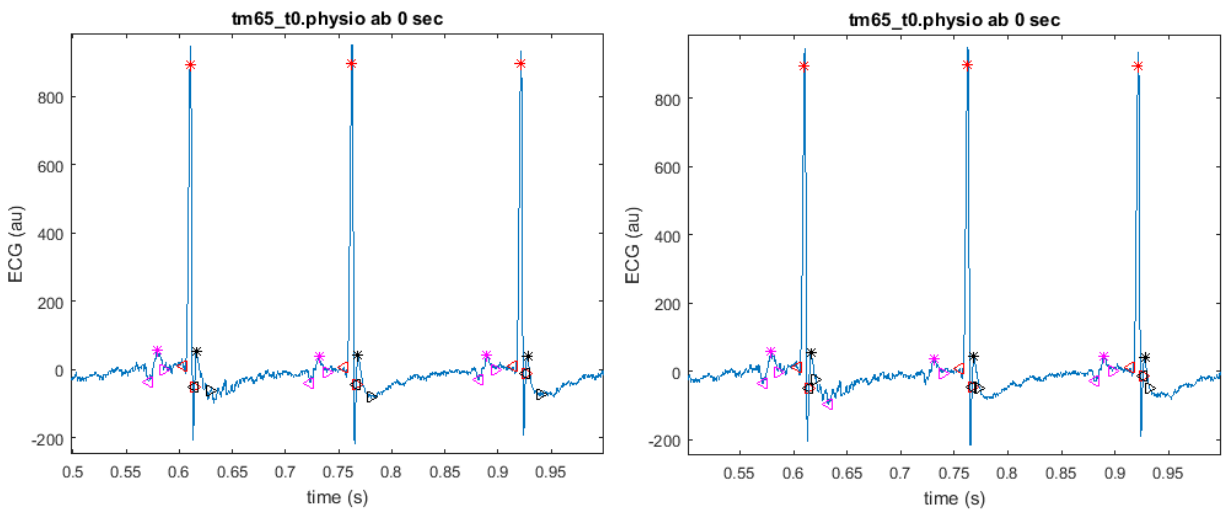

Figure 5.3: *ECG algorithm performance. T-offset detection by geometric option (a) and by TRA method (b).*

5.3 Bland Altman Plots

The Bland Altman plot is a graphical method to compare two measurement techniques. The graphic displays differences between two methods ($value_1$-$value_2$) plotted in the y-axis against the averages of the two measurements in the x-axis [143].

Limits of agreement or LoA are estalished at the mean ± 1.96 SD of differences, where 95% of the differences between measurements are included [143]. The maximum allowed difference should be defined in advance for a good interpretation of the method comparison. If the limits of agreement are in between the negative and possitive maximum allowed difference, both methods are considered to be on agreement [146].

The mean difference between measurements is the estimated bias, and the SD measures random fluctuations around it. However, a trend or a tendency for the mean difference can be as well detected in the bias when increasing the magnitude [146]. Figure 5.4 shows an example where

two methods to measure systolic blood pressure, at the finger and the arm, are compared. LoA and the trend, as a regression line, are drawn.

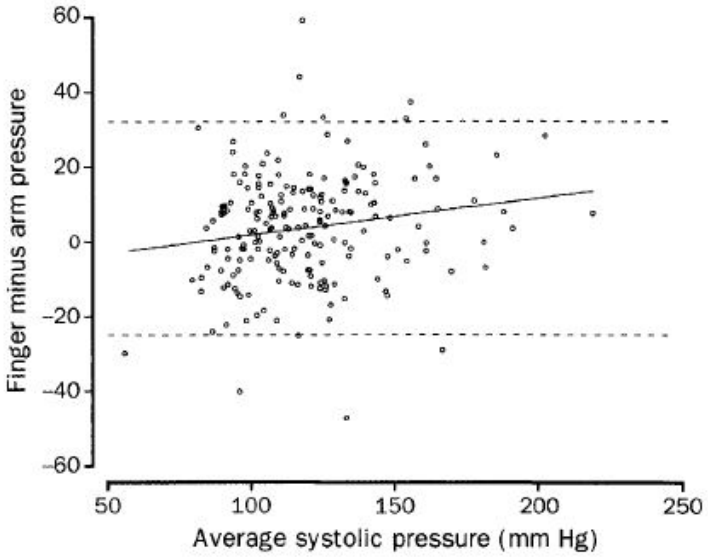

Figure 5.4: *Bland Altman plots to compare two pressure measurement techniques [146].*

For 95% of the subjects, finger measurement will be between 24 mmHg below the arm pressure and 33 mmHg above it. This, however, is a wide range, which denotes a very poor agreement between both methods [146]. In this case, the trend shows an increase in the difference between methods when increasing the magnitude of the measurement. Thus, a certain correlation between difference and average can be established.

5.4 Statistics

When performing a comparison test, data can be paired or unpaired, depending on the test case. Paired samples or populations are those where observations in one sample are related with observations in the other. Usually, paired samples involve the same subjects, where observations have been taken at two different ages or after two different treatments.

Tests for comparison can be either non-parametric or parametric. When non-normal data or of unknown distribution, a non-parametric test is performed and results are shown as median and its interquartile range (IQR). The test applied in this case is known as the Wilcoxon rank test, convenient for small sample size, and robust identifying outliers [147]. However, when they are normally distributed data, results are presented as mean and standard deviation.

The P-value is a probability number that indicates the correlation between two compared groups [148]. A low value indicates a strong evidence against the null hypothesis (no correlation between

the groups). In this thesis, boxplots are used to illustrate the comparison of different parameters between two groups. A significant difference is marked by asterisks at the top of each boxplot. One asterisk shows a $P \leq 0.05$ in our analysis. Two asterisks show a p-value lower than 0.01, while three, lower than 0.001.

For paired groups, the non-parametric test is called Wilcoxon signed-rank (one-sample) [149]. If not normally distributed unpaired data are compared, the non-parametric test applied is called Wilcoxon rank-sum test (two-samples) [149].

Of note: results in this thesis are presented as mean and standard deviation, as well as the median and the interquartile range. However, to allow comparability with the results from N. D. Lascio et al. [6] and due to the small sample sizes, non-parametric tests have been used for comparison.

CHAPTER 6

Algorithms Design

The design of the program allows to run four different analysis in order to compare cardiovascular parameters between two groups of mice. These analyses are: (1) a physiological comparison, (2) ECG intervals comparison, (3) wave intensity analysis and (4) vascular analysis.

All details about the implemented approaches and algorithms are explained in the following.

6.1 Program Overview

A general overview of the program is shown in figure 6.1. Below some steps, represented in boxes, conditions are specified. Conditions in orange are optional, while conditions where different options are possible are written in blue. As illustrated, the four analyses can be run independently. After each analysis, parameters are compared within a boxplot. After analyses are run, a table with all parameters is generated showing the results of the comparison tests applied.

The analyses can be shortly summarized as follows:

1. The physiological analysis allows the comparison of the heart rate, the respiration rate and the temperature between two groups. Algorithms used for the determination of the heart rate and the respiration rate are explained in sections 6.2 and 6.3, respectively.

2. For the ECG intervals comparison, the algorithm developed by Caroline Magg [9] has been applied. The five intervals calculated are: qt, qtc, pq, qrs and rr, all measured in seconds. The rr-interval represents the duration of a heart beat.

3. Wave intensy analysis requires the determination of the PWV. The algorithm calculates the PWV first (see section 6.4) and then the WI signal, from where WIA-derived parameters are obtained (see section 6.5).

4. The name of the vascular analysis comes from the involved diameter and velocity measurements to calculate vascular-derived parameters (see section 6.7). Thereafter, diameter values have been used to calculate the AIx (see section 6.6).

Before starting the program, one can set various options to select analyses and settings. Before performing the selected analyses, one has to choose the groups to be compared.

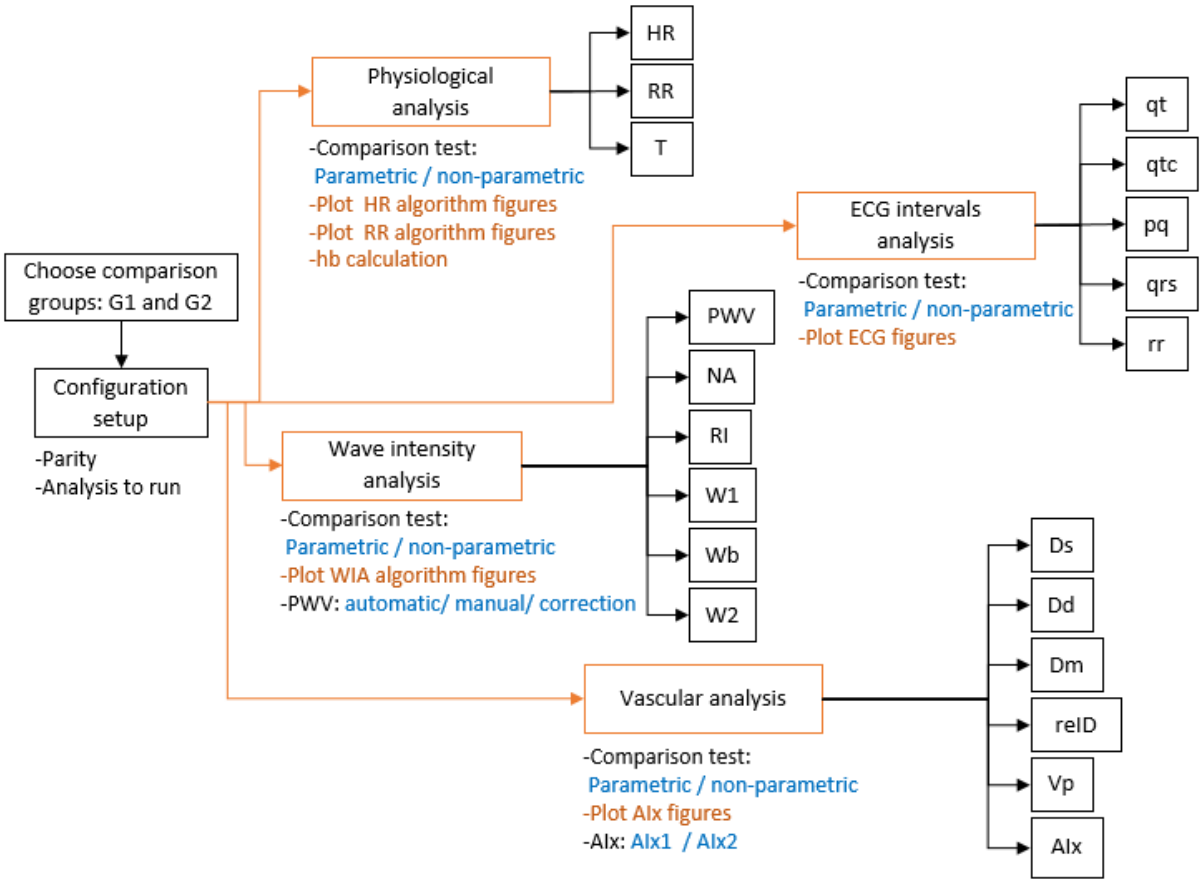

Figure 6.1: *Overview diagram showing the four possible comparison analysis and the parameters obtained.*

6.2 Heart Rate Algorithm

The heart rate algorithm (HR algorithm) allows the identification of the heart rate and, optionally, the heart beat duration. The workflow of the algorithm is shown in figure 6.2.

Green boxes in the shape of rounded rectangles contain the steps for which a different subplot is generated by the algorithm, if plotting is selected. Orange boxes represent optional plots. Steps in orange are also optional.

In a very first step, ECG signal peaks can be identified using the Matlab function *findpeaks*. In order to not misclassify the R-peak and the peak of the J-wave, two thresholds have been defined. The first threshold is the the minimum distance between peaks, which has been set as

1/15 times the sample frequency. The second threshold is the minimum height, chosen as the mean amplitude of the ECG signal.

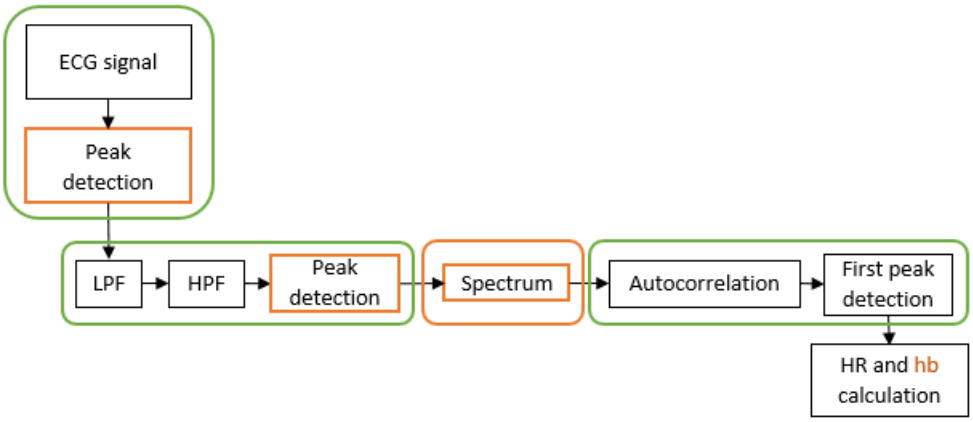

Figure 6.2: *Heart rate algorithm workflow.*

Figure 6.3 shows an example of how the HR algorithm works for a wild type mouse at two different ages. For clean and clear signals, this approach is good enough to determine the heart rate, as one can see in figure 6.3a. However, this is not always the case. Sometimes the power line noise interference at 50 Hz is extremely high, as exemplarily shown in figure 6.3b.

(a)

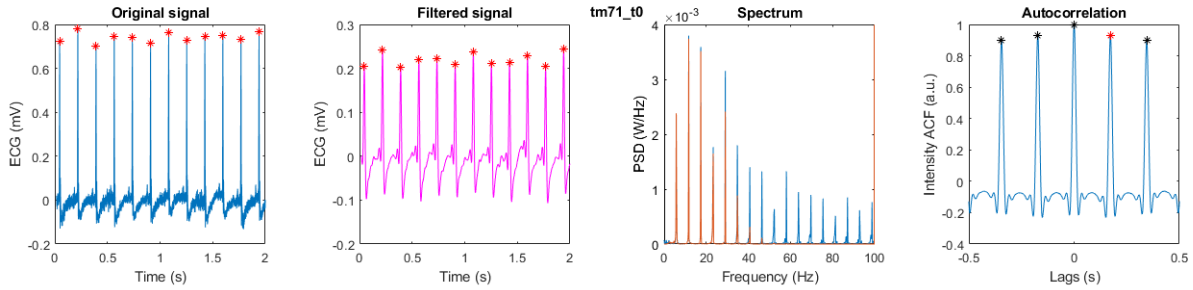

(b)

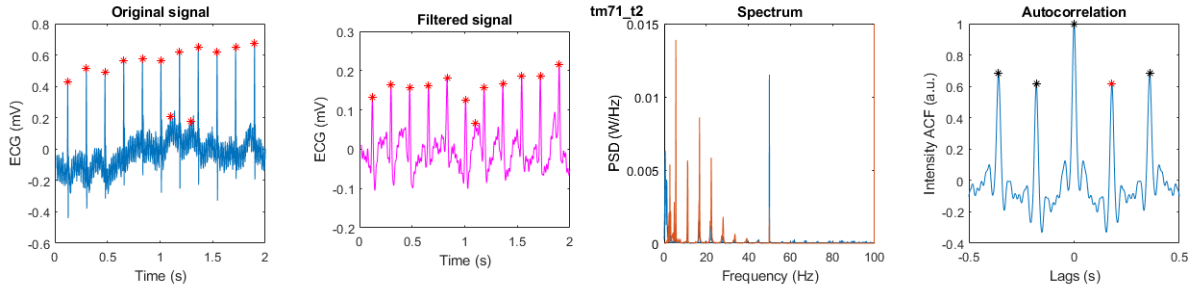

Figure 6.3: *Heart rate algorithm output figures. ECG signals from a wild type mouse at the age of 8 weeks (a) and at the age of 25 weeks (b).*

In a second step, a low pass filter (LPF) has been implemented to remove the noise. After some trials, a cutoff frequency of 40 Hz has been proved to work properly for most of the cases. After that, a high pass filter (HPF) has been used in order to remove the influence of breathing, where

the cutoff frequency has been fixed at 2 Hz. Again, *findpeaks* is used to identify the R-peaks in the filtered signal.

After filtering, the spectrum of frequencies of the signals can be optionally calculated to show the efficiency of the filters. The spectrum of the original signal, in blue, and of the filtered signal, in orange, are displayed (figure 6.3).

However, it could happen that *findpeaks* again does not work properly due to the shape of the recorded signal. This can be observed in figure 6.3 (lower trace) for the wild type mouse tm71 at the age of 25 weeks. To overcome this problem, the autocorrelation function of the filtered signal has been calculated.

The autocorrelation of a signal and the signal itself have the same cyclic characteristics. The first peak in the autocorrelation corresponds to the period of the waveform. For this reason, autocorrelation has been used to calculate the heart rate frequency. Additionally, the heart beat duration can also be derived from it.

6.3 Respiration Rate Algorithm

The respiration rate algorithm, or simply RR algorithm, is used to calculate the periodicity of the breathing signal. The design of algorithms for the calculation of HR and RR is pretty similar. The workflow of the respiration rate algorithm is shown in figure 6.4. Again, green boxes indicate plotted intermediate steps, and orange boxes and steps are optional.

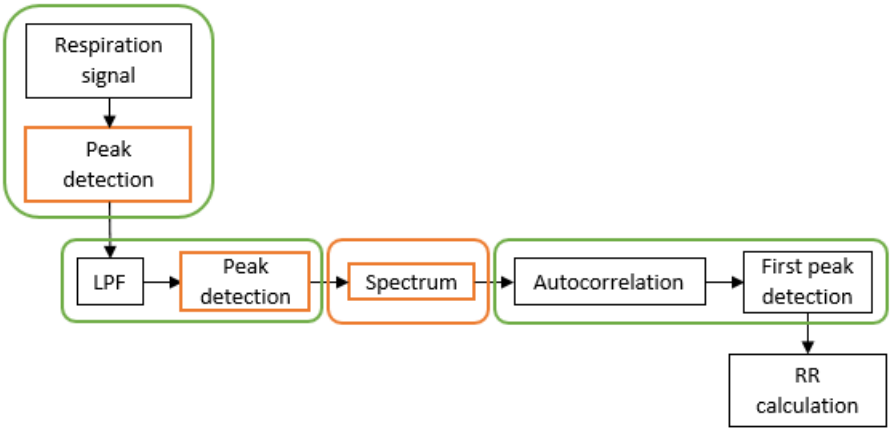

Figure 6.4: *Respiration rate algorithm workflow.*

The main difference is that the RR algorithm is performed using only a low pass filter (LPF) to remove possible high frequency noise, with a cutoff frequency of 5 Hz.

In figure 6.5, one can exemplarily see how the algorithm works in a wild type mouse. In the upper trace (figure 6.5a), one can observe how the Matlab function *findpeaks* is enough to detect the periodicity of a clean signal, where all R-peaks are detected. However, in comparison to

this approach, autocorrelation function assures a more reliable result as one can see in figure 6.5b, where the same mouse has been examinated again at t2. Thus, periodicity is obtained independently of the shape of the recorded signal.

(a)

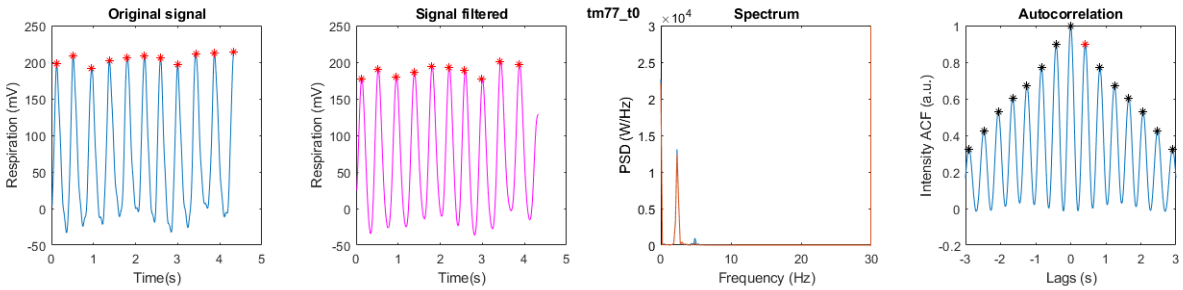

(b)

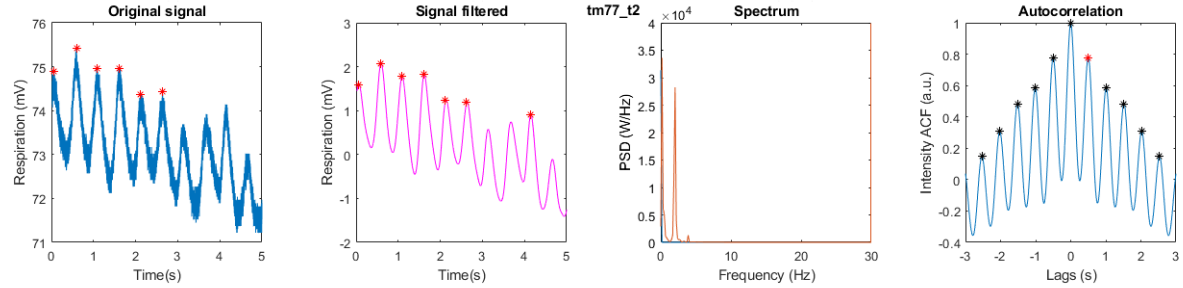

Figure 6.5: *Respiration rate algorithm output figures. Respiration signals from a wild type mouse at the age of 8 weeks (a) and at the age of 25 weeks (b).*

6.4 Pulse Wave Velocity Algorithm

The lnD-V loop method, briefly introduced in section 3.3.3, has been considered to calculate the local PWV. In this section, a more detailed explanation of the method is given.

Although along this thesis, blood flow velocity is denoted as V, in the mathematical expressions found in this section it is, as originally, denoted as U.

Pressure and velocity changes are assumed to be the addition of the differences across the forward (+) and backward (-) wavefronts. Thus, they can be defined as:

$$dP = dP_+ + dP_- \tag{6.1}$$

$$dU = dU_+ + dU_- \tag{6.2}$$

During early systole, simultaneous pressure and flow velocity follow a linear relationship in the absence of reflected waves [150]. This relationship is described by the water hammer equation,

which can be written as

$$dP_x = \pm \rho c dU_x \tag{6.3}$$

where ± refers to forward and backward waves, dP and dU are pressure and blood flow velocity differences over the measured interval in the direction of the blood flow (x), ρ is the blood density and c is the wave speed, i.e. the pulse wave velocity.

Based thereupon, Khir et al. developed a method to assess the wave speed in early systole (upstroke) [151–153] in 2001. This method is called the pressure-velocity loop or PU-loop. The slope of the loop is defined as follows:

$$S_o = \frac{dP_+}{dU_+} = \rho c \tag{6.4}$$

In 2009, Khir et al. introduced a new version of this method using diameter (D) and U waveforms [122]. Diameter changes due to forward and backward pressure changes can analogously be expressed as:

$$dD = dD_+ + dD_- \tag{6.5}$$

If there are only unidirectional waves present, a linear relationship between the natural logarithm diameter and velocity values is derived. Then, local wave speed can be determined as:

$$c = \pm 0.5 \cdot \frac{dU\pm}{dlnD\pm} \tag{6.6}$$

In this thesis, three modes to calculate the PWV have been implemented. The first mode assesses the PWV fully automatically. The other two options allow manual correction in case of noisy curves or in cases where points from the non-linear parts of the loop are erroneously included. The second mode, manual, allows the user to choose the starting and ending points of the linear part of the diameter curve for every mouse. The third mode, correction, is a mixture of the previous modes: once the automatic PWV has been calculated for each subject, the user is asked if a manual correction is needed before continuing.

The workflow of the PWV algorithm is shown in figure 6.6. In a first step, the algorithm creates the lnD-V loop. Then, the linear phase during early systole is identified. Starting and ending points for calculating the slope are chosen as those where velocity reaches its 5% and 90%, respectively, following the steps of N. D. Lascio et al. [154].

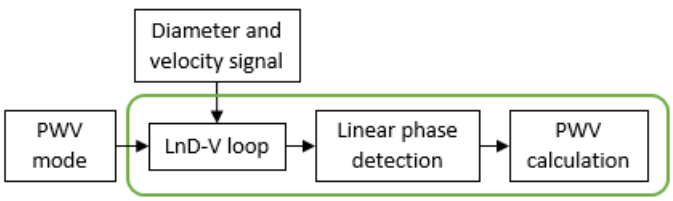

Figure 6.6: *Pulse wave velocity algorithm workflow.*

In the last step, PWV is calculated using Khir's method [122], with the following expression:

$$PWV = \frac{0.5}{S_o} \tag{6.7}$$

where S_o is the slope of the loop.

6.5 Wave Intensity Analysis Algorithm

Forward and backward waves identification in mice has also been accomplished using simultaneous diameter and velocity measurements. This idea was first introduced by Niki et al. in 2002 [137], based on the use of the water hammer equation for forward traveling waves. Another option to calculate wave intensity was be means of the pulse wave velocity, idea introduced by the same group [138]. Years later, in 2007, Khir et al. [153] devised a new model where wave intensity was also calculated using wave speed and diameter signals.

Wave intensity analysis is based on the method of characteristics solution of the 1-D equations derived from the conservation of mass and momentum in elastic vessels, as described by Parker et al. in 1990 [7] and later on, together with Khir et al. in 2004 [152]. The successive wavefronts of pressure P and velocity U propagate forward and backward through the vessels with magnitudes dP and dU [155].

The net wave intensity, denoted as dI, is usually obtained multiplying changes in pressure with changes in blood flow velocity:

$$dI = \frac{dP}{dt} \cdot \frac{dU}{dt} \tag{6.8}$$

The analysis is carried out in the time domain, since the waveforms of pressure and velocity are represented as successive wavefronts.

Forward and backward wave intensities can be aproximated as dI_+ and dI_- [152], leading to the following expression:

$$dI_{\pm} = \frac{1}{4\rho c} \cdot (dP \pm \rho c dU)^2 \tag{6.9}$$

In this thesis, the energy carried by forward and reflected waves has been calculated by means of the wave intensity signal using Khir's method [152], as in the work of N. D. Lascio et al. [6]. The following mathematical expression has been used:

$$dI_{\pm} = \frac{1}{4(D/2PWV)} \cdot (dD \pm \frac{D}{2PWV} dV)^2 \tag{6.10}$$

The workflow of the WIA algorithm is shown in figure 6.7. Diameter and velocity signals are used to calculate the PWV depending on the chosen mode. To calculate the PWV (step in red), the PWV algorithm is called. Thereafter, the wave intensity signal is calculated using equation

6.10.

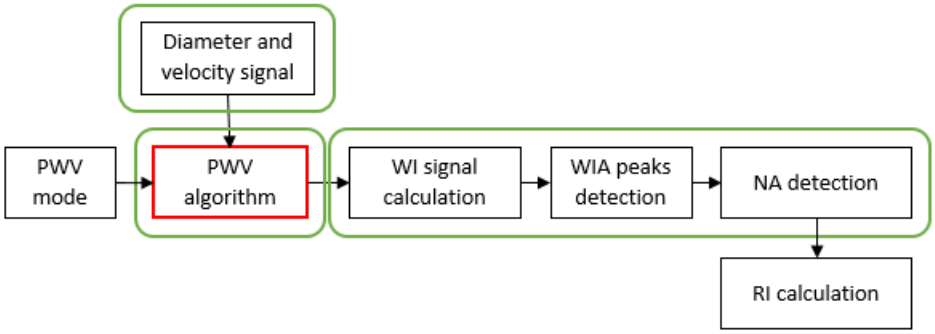

Figure 6.7: *Wave intensity analysis algorithm workflow.*

Once the wave intensity signal is estimated, the W1, Wb and W2 peaks are identified. W1 represents the forward wave. The second peak, with negative magnitude, represents the energy of reflected waves. W2 corresponds to the forward expansion front related to the closing of the aortic valve. Further explanations about these parameters can be found in section 2.3.

Afterwards, the negative area is determined and the reflection index is calculated as:

$$RI = \frac{Wb}{W1} \tag{6.11}$$

Figure 6.8 illustrates an example where the PWV and WIA algorithms have been performed in a wild type mouse at the age of 8 weeks. Image on the left shows diameter and velocity recording from mouse tm65. In the second image, the slope of the loop (in red) is calculated between the two green points, after what the PWV is calculated. In the image on the right, the wave intensity peaks are detected (in magenta), and the negative area is calculated.

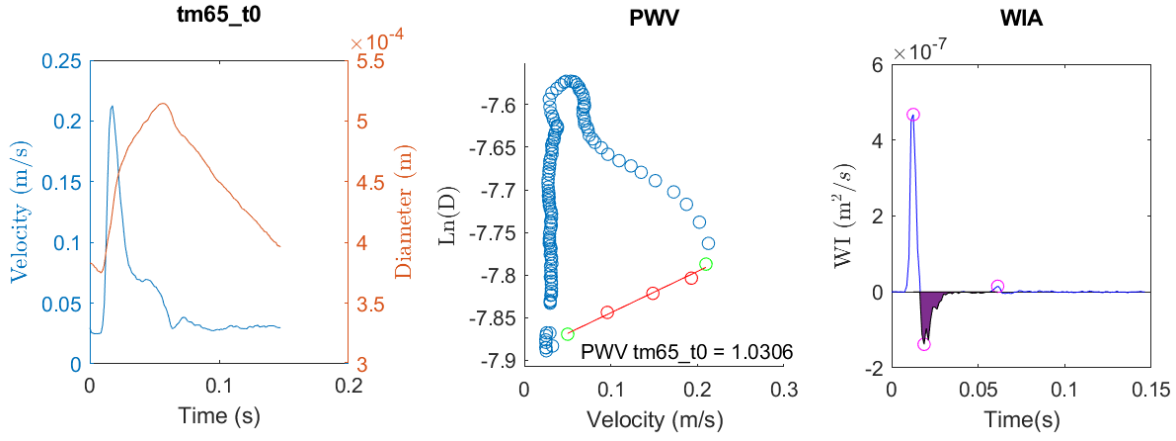

Figure 6.8: *Wave intensity analysis algorithm output figures for a wild type mouse at the age of 8 weeks.*

6.6 Augmentation Index Algorithm

The aim of the developed algorithm is to detect the augmentation index from a diameter signal following the steps of C. J. Hartley et al. [133]. Hartley's approach to detect the inflection point in the diameter curve estimating the arrival of reflected waves was based on the method described by J. P. Murgo et al. for pressure signals [156].

According to J. P. Murgo et al. [156], depending on the waveform, pressure signals can be classified in four groups [156]. In signals from types A and B, the systolic blood pressure comes after the inflection point caused by the wave superposition as illustrated in figure 6.9 (left). For these signals, AIx is calculated as follows:

$$AIx = \frac{P_s - P_i}{P_s - P_d} \tag{6.12}$$

where P_s is the systolic blood pressure, P_d the diastolic blood pressure and P_i the pressure at the inflexion point. The denominator of the function represents the pulse pressure (PP). For type A signals, AIx is higher than 0.12. For type B signals, AIx lies between 0 and 0.12.

In type C pressure signals, the systolic pressure peak precedes the inflection point, as shown in 6.9 (right). For this case, AIx is calculated as follows:

$$AIx = \frac{P_i - P_s}{P_s - P_d} \tag{6.13}$$

In type D signals, the reflected wave arrives early in systole and merges with the incident wave. For this reason, the inflection point cannot be observed visually.

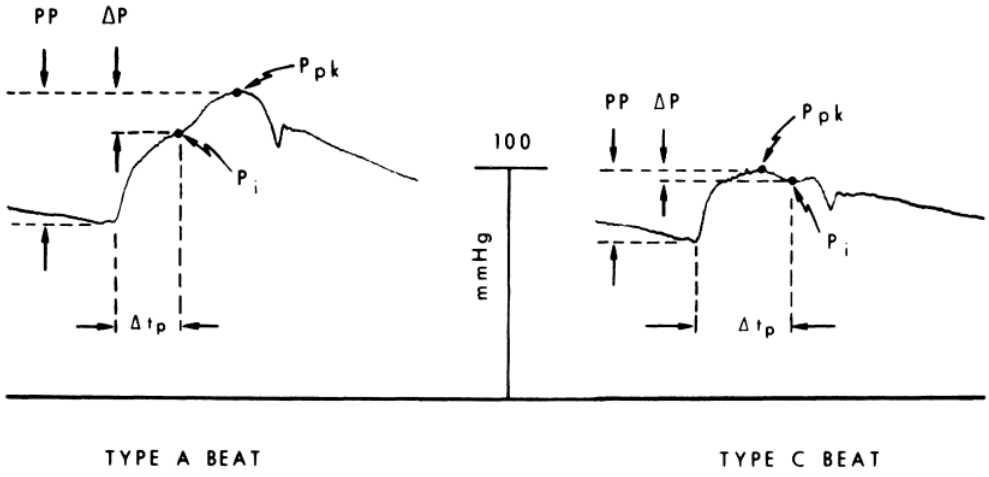

Figure 6.9: *Determination of parameters to calculate AIx in type A and C pressure signals. P_{pk} is the peak systolic pressure, P_i the inflection point, and A_{tp} the time the wave needs to travel from the heart to the reflection site and back.*

AIx values higher than 0.12, as in type A signals, correspond to a large artery stiffness. In type B signals, reflected waves arrive in late systole, indicating a lower arterial stiffness.

The idea of using diameter signals to calculate the AIx was performed in mice by Hartley et al. in 2004 for the first time [133]. They considered only signals where the systolic diameter (i.e. the maximal diameter) comes after the anacrotic notch, i.e. type A and B. The anacrotic notch was determined as the inflection point of the diameter signal before reaching its maximum, the systolic diameter.

In the present work, two methods have been designed in order to detect the inflection point of the diameter curve. In both methods, the notch is detected by calculating the 1^{st} derivative of the diameter wave and identifying its local minimum located between diastolic and systolic diameter values, as shown in figures 6.12a and 6.12b.

Figure 6.10 shows the workflow of the implemented algorithm. Different signals are derived from the diameter wave in order to provide a robust detection of the inflection point, which is calculated taking the median of three points in both methods. The signals involved to calculate these points are the same in both methods.

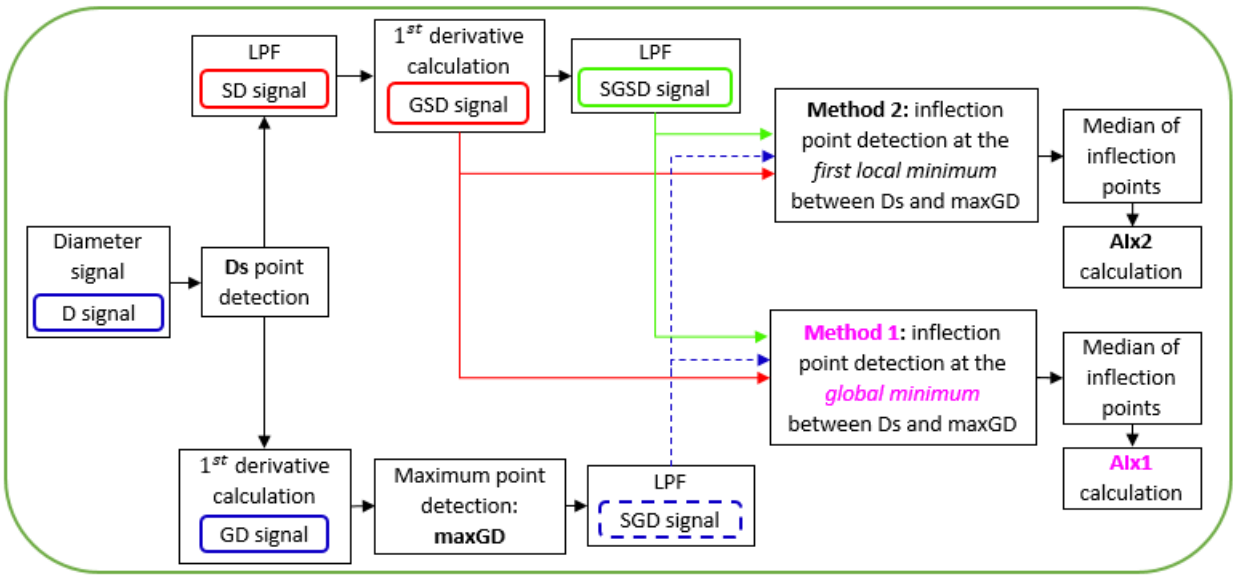

Figure 6.10: *Augmentation index algorithm workflow. The different signals used are: diameter (D), smoothed diameter (S/D), gradient smoothed diameter (GSD), smoothed gradient smoothed diameter (SGSD), gradient diameter (GD) and smoothed gradient diameter (SGD).*

The first derived signal comes from smoothing the diameter. To do this, a low pass filter (LPF) has been designed. A cutoff frequency of 12 times the heart rate of the examined mouse has been proved to work properly for the datasets used. From now on, this filtered signal will be called smoothed diameter (SD), plotted in red (see figures 6.11, 6.12b and 6.12a).

Following Hartley steps, the first derivative or the gradient of the diameter signal has been calculated. It is plotted in blue as the original diameter signal. This signal is denoted as gradient diameter (GD) signal. The gradient of the SD signal has been as well calculated, denoted as gradient smoothed diameter (GSD), in red as the SD signal.

Similarly to Hartley et al., the implemented algorithm is only designed to work with type A and B diameter signals. For this reason, inflection points to calculate the AIx are searched in the time interval between the maximum of the first derivative of the diameter curve (GD), denoted as $maxGD$, and the maximum of the diameter curve, corresponding to the systolic diameter, denoted as D_s. Both points are shown in the algorithm plots as red stars (see figure 6.11).

Local minima in the gradient diameter curves during the delimited time interval are used to find the inflection points in the original diameter curve (D). For this reason, GSD and GD signals are also filtered in order to get smoother curves with fewer local minima. These signals are named smoothed gradient smoothed diameter (SGSD) and smoothed gradient diameter (SGD), in green and dashed blue, respectively. The remaining local minima correspond to the inflection points with higher influence, more likely to reflect the arrival of reflected waves instead of changes in the slope due to a bad quality of the signal.

Figure 6.11 shows an example of the algorithm performed in wild type mmouse. Local minima in gradient diameter curves are illustrated, as well as the different inflection points in the original diameter curve used to calculate the augmentation index.

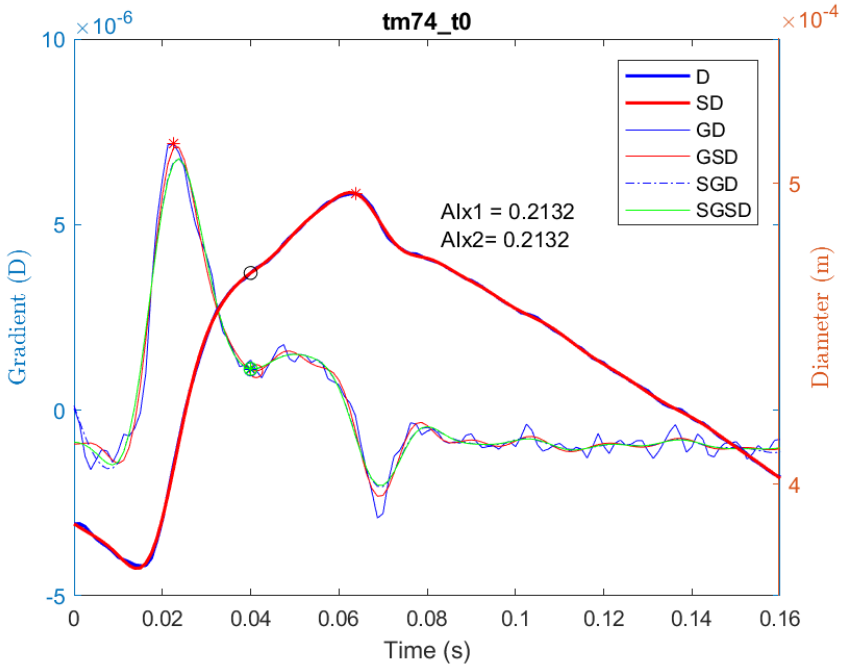

Figure 6.11: *Augmentation index algorithm performance with one inflection point detected over a wild type mouse. In the right y-axis, diameter (D) in blue and smoothed diameter (SD) in red signals are represented. In the left y-axis, the first derivative or gradient diameter signals are represented: original gradient diameter (GD) in blue, smoothed gradient diameter (SGD) as a dashed blue line, gradient smoothed diameter (GSD) in red, and smoothed gradient smoothed diameter (SGSD) in green.*

The first method calculates the median of the first local minimum detected in the three specified first derivative diameter signals between diastolic and systolic diameter, based on Hartley's idea, scattered as empty circles.

The second method, on the contrary, calculates the median of the lowest minimum detected in the first derivative diameter signals, which a strongest change in the slope, scattered as filled circles.

The inflection point corresponding to AIx1 (aumentation index achieved by method 1) is scattered in magenta over the original diameter curve (see figure 6.12b). It is located at the time where the median of the first local minimum from signals SGSG, GSD and SGD is found. The notch corresponding to AIx2, achieved by the second method, is scattered in black over D at the time where the median of the lowest minimum from the previous mentioned signals is located (figure 6.12b).

If signals were ideal, there would be only one clear notch in the diameter curve. Exemplarily, this happens in the case of the wild type mouse, illustrated in figure 6.11. In this case, the first derivative signal presents only one local minimum in the range delimited between diastolic and systolic diameter. Therefore, both methods return the same AIx value, and only the black circle can be seen.

However, signals may not always be ideal, since sometimes not only one notch will be identified, as for example in the case of the FF26 ApoE mouse, shown in figure 6.12. This is the reason why two methods have been implemented. Diameter derived signals can be better seen in figure 6.12b, where the figure 6.12a has been zoomed in.

The augmentation index (AIx) is then calculated by dividing the change in diameter, from the inflection point to the systolic diameter, by the difference between systolic and diastolic diameter values as follows:

$$AIx = \frac{D_s - D_i}{D_s - D_d} \tag{6.14}$$

where D_s is the diastolic diameter, D_d the diastolic diameter, D_i the diameter at the anacrotic notch, and D_s - D_i the change in diameter.

6.7 Vascular Derived Parameters

Derived from vascular measurements, diameter and velocity parameters are calculated to analyze the distension capability of the vessels as in the work of N. D. Lascio et al. [6]. Those parameters are: mean diameter (Dm), diameter at systole (Ds), diameter at diastole (Dd), relative distension (reID) [6] and peak velocity, the maximum blood flow velocity (V_p). Relative distension is a parameter representative of the vessel storage capability [157]. It is calculated as follows:

$$reID = (\frac{D_s - D_d}{D_d}) \cdot 100\% \tag{6.15}$$

(a)

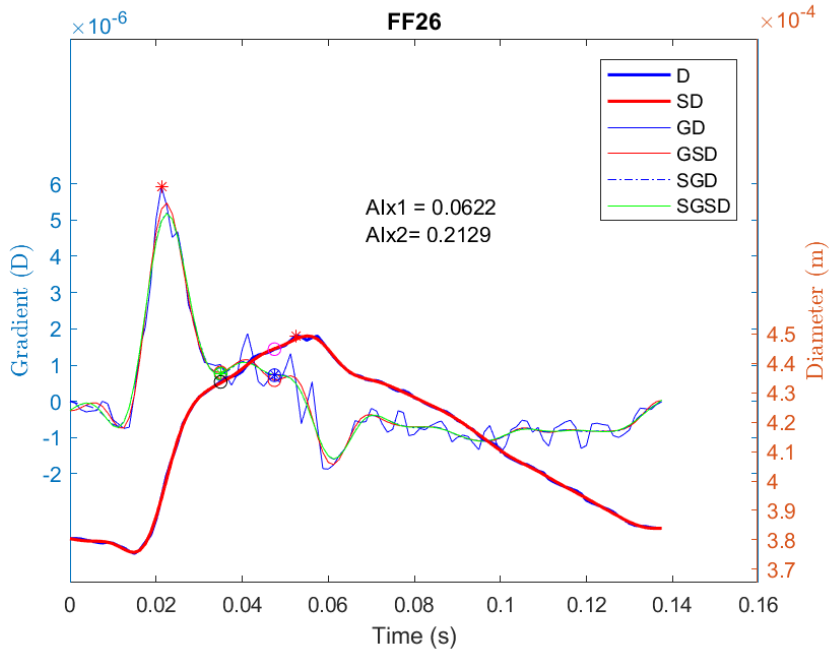

(b)

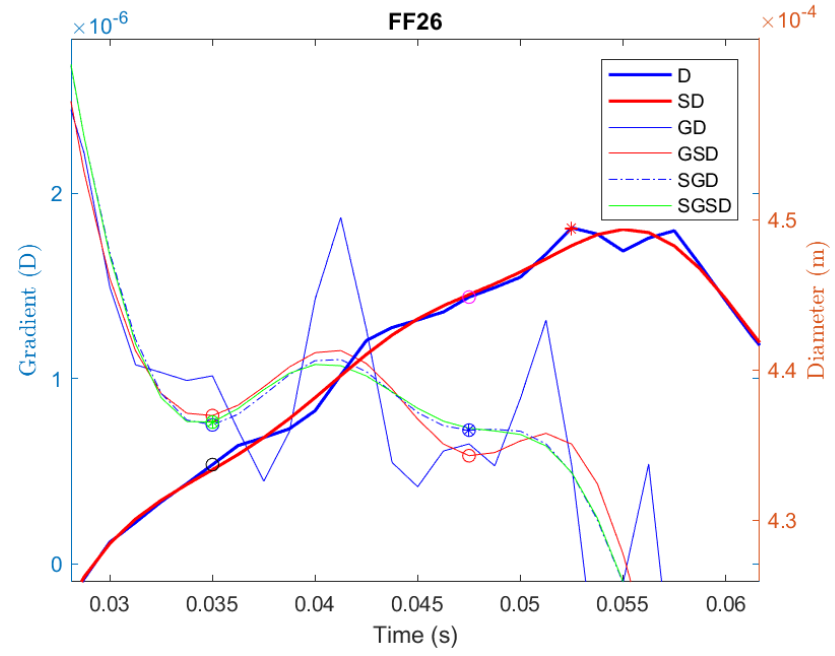

Figure 6.12: *Augmentation index algorithm performance with two inflection points detected over an ApoE mouse, mouse FF26 16 weeks old (a), amplified in (b). In the right y-axis, diameter (D) in blue and smoothed diameter (SD) in red signals are represented. In the left y-axis, the first derivative or gradient diameter signals are represented: original gradient diameter (GD) in blue, smoothed gradient diameter (SGD) as a dashed blue line, gradient smoothed diameter (GSD) in red, and smoothed gradient smoothed diameter (SGSD) in green.*

CHAPTER 7

Results and Statistical Analysis

In this chapter, some implemented algorithms are firstly validated by comparing them to values obtained by external algorithms. Thereafter, the four different analyses (physiological, ECG intervals, wave intensity and vascular analysis) have been performed in the three test cases. The main aim of this study is to compare results, obtained when applying these analyses, with those from N. D. Lascio et al. [6] for TC1.

Results in this thesis are presented as mean and standard deviation, as well as the median and the interquartile range. However, to allow comparability with the results from N. D. Lascio et al. and due to the small sample sizes, non-parametric tests have been used for comparison.

7.1 Validation of Algorithms

Three algorithms have been validated by means of Bland Altman plots in this section. The heart beat duration obtained with the HR algorithm (section 6.2) is compared to the rr-interval obtained applying the murine ECG algorithm (section 5.2). Automatic PWV algorithm is compared to N. D. Lascio's method. Last, AIx1 and AIx2 values obtained applying methods 1 and 2 to calculate the augmentation index (section 6.6) are evaluated as well.

7.1.1 Heart Rate Algorithm

The rr-peak interval values, obtained with the Murine ECG analysis algorithm, have been used to validate the HR algorithm. The corresponding Bland-Altman plot is shown in figure 7.1.

The mean difference between values obtained with each of the methods is less than 55 μs (HR algorithm - ECG algorithm) with a standard deviation of 1.3 ms. Furthermore, no trend can be seen.

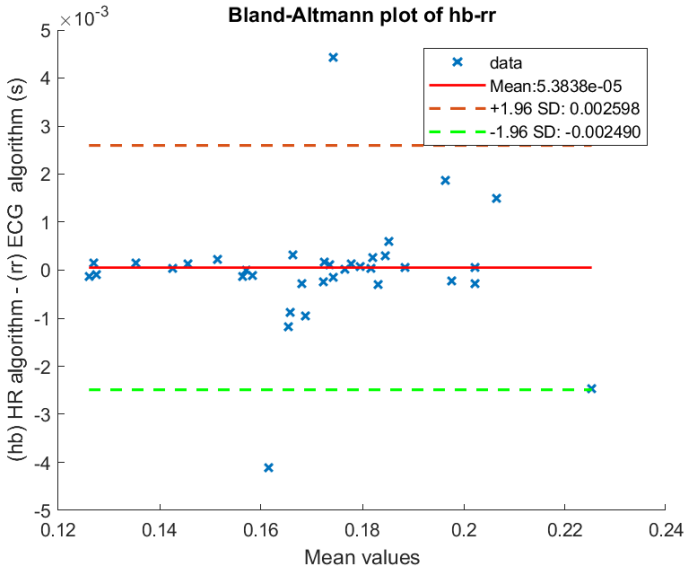

Figure 7.1: *Bland Altman plot to compare values obtained with HR and ECG algorithms.*

In some cases, the HR algorithm under- or over- estimates the heart beat duration compared to the ECG algorithm. However, considering a normal heart beat duration of 70-190 ms in mice, the difference set by the limits of agreement is small enough to consider the methods as equivalent.

7.1.2 Pulse Wave Velocity Algorithm

The PWV algorithm has been compared to the one designed by N. D. Lascio et al. [6] using all mice from all four datasets, except for two wild type mice (at t0 and t2) from which physiological data was not provided (41 mice). The comparison graph is shown in figure 7.2.

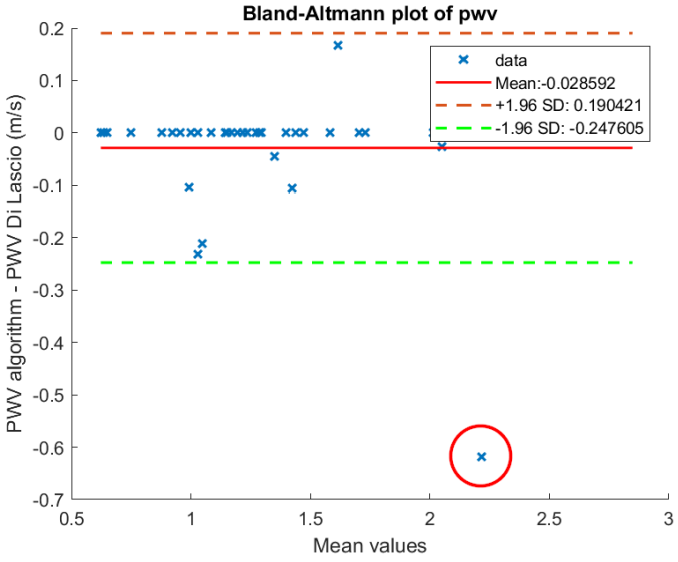

Figure 7.2: *Bland Altman plot to compare the implemented PWV algorithm and the algorithm from N. D. Lascio et al. [6]. The red circle contains the PWV difference from FF24 mouse.*

The mean difference between values obtained with each of the methods is less than 28.6 mm/s (PWV algorithm - PWV N. D. Lascio) with a standard deviation of 112 mm/s. For the mouse FF24, however, there is a significance difference between PWV values achieved by both methods. This is probably due to the fact that N. D. Lascio applied manual correction in some cases.

Being the mean of the PWV values provided by N. D. Lascio over the 41 mice of 1.36 m/s, the limits of agreement established by the differences between PWV values are considered acceptable. This allows for the comparison between PWV algorithm results with those from N. D. Lascio et al. [6].

7.1.3 Augmentation Index Algorithm

In figure 7.3, one can see the Bland Altman plots to compare AIx1 and AIx2 values obtained applying both implemented methods in the four datasets of mice.

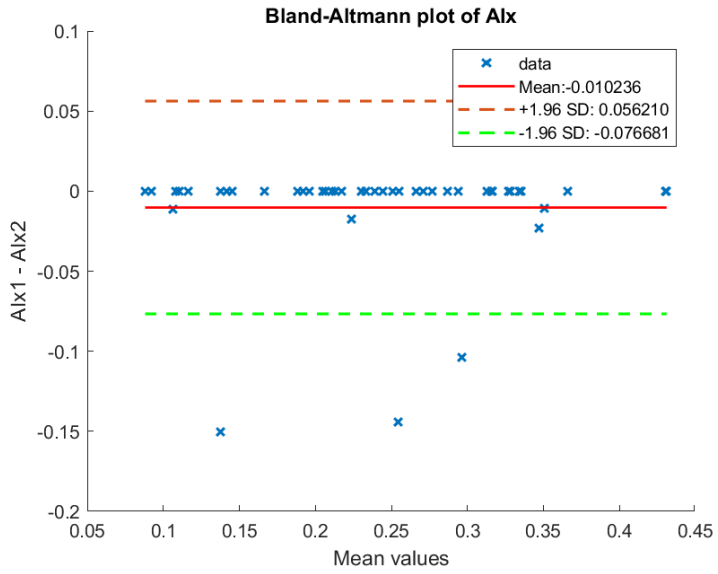

Figure 7.3: *Bland Altman plot comparing both implemented methods to calculate the AIx.*

The mean difference between values obtained with each of the methods is around -1.02% (AIx1 - AIx2) with a standard deviation of 3.4%. This time, points showing a non-zero difference in the comparison graph reflect the non-ideal cases, where the diameter curve has more than one inflection point.

However, since a high difference is only noticeable (higher than 10%) in a small number of cases, in this thesis and with the datasets provided, both methods can be used interchangeably for comparing the different groups of mice.

7.2 TC1: Comparison between Young and Old Wild Type Mice

The first comparison has been performed for TC1, this is, on a sample of wild type mice (n=13) at the age of 8 (WT_t0) and 25 weeks (WT_t2). In our study, this is the only test case where mice comparison is paired, since it is based on wild type mice, measured at two different ages. Thus, results of applying a Wilcoxon signed-rank are shown in table 7.1.

Figure 7.4 shows how the median of HR, RR and temperature decrease with age. RR and temperature at t2 show a significant difference with respect to t0 (RR_{t0} = 131 [111 156] (bpm), RR_{t2} = 117 [95.8 133] (bpm), p_{RR} = 0.01; T_{t0} = 35.5 [35.1 35.6] (^{o}C), T_{t2} = 34.8 [33.8 35.1] (^{o}C), p_T = 0.02), while HR decreases non-significantly (HR_{t0} = 379 [346 405] (bpm), HR_{t2} = 340 [324 369] (bpm), p_{HR} = 0.41)

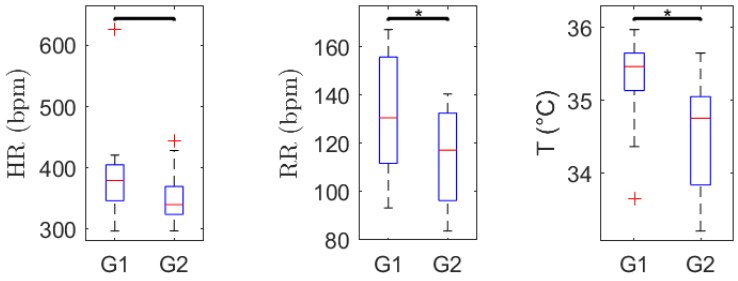

Figure 7.4: *Physiological comparison for TC1.*

When comparing wild type mice, one can see that time between two heart beats increases. Exemplarily, in figure 7.5, an ECG from a wild type mouse (id tm72) is shown. At the age of 8 weeks (t0), the young mouse shows a heart rate of 345 bpm, which decreases to 324 bpm after 17 weeks (t2).

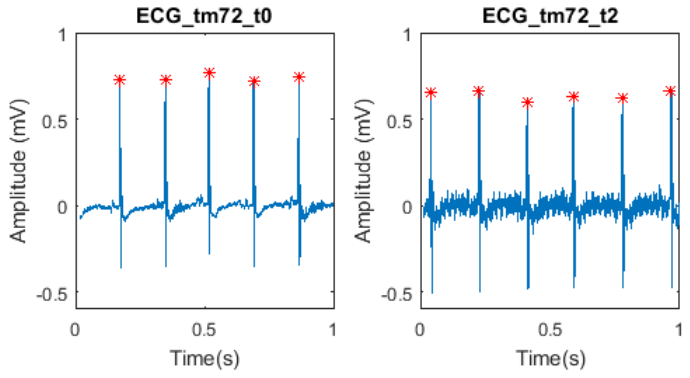

Figure 7.5: *Example of duration of a heart beat for a wild type mouse at t0 and t2.*

Exemplarily, the respiration signal from the wild type mouse tm72 is shown in figure 7.6. As one can see, time between two respiration peaks is higher when the mouse is older, at 25 weeks. The RR is 109.09 bpm at t0 while 83.52 bpm at t2.

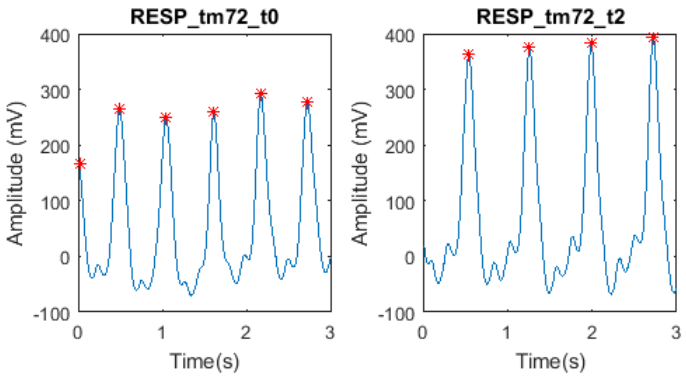

Figure 7.6: *Example of duration of a respiration beat for a wild type mouse at t0 and t2.*

ECG intervals comparison for TC1 is shown in figure 7.7 and table 7.1. In general, duration of all intervals is higher in t2 measurements. However, only changes with age in qt and qrs are significant (qt_{t0} = 0.0237 [0.0226 0.0273] (s), qt_{t2} = 0.0291 [0.0272 0.0315] (s), p_{qt} = 0.01; qrs_{t0} = 0.0101 [0.0091 0.0112] (s), qrs_{t2} = 0.0113 [0.0108 0.0147] (s), p_{qrs} = 0.01).

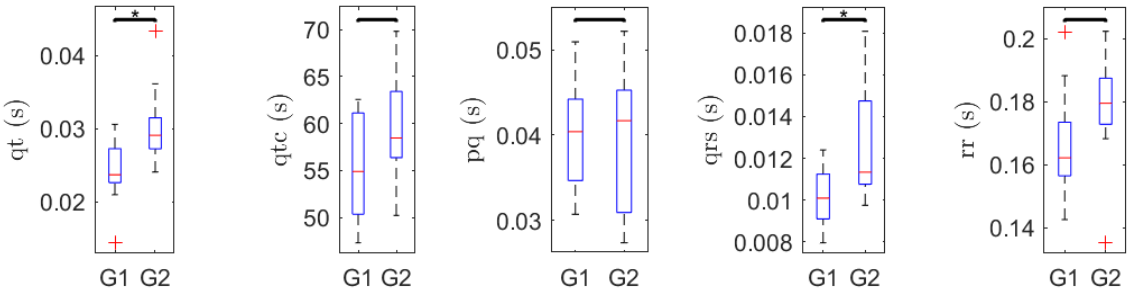

Figure 7.7: *ECG interval comparison for TC1.*

PWV and WIA-derived parameters comparison of TC1 is shown in figure 7.8. NA and W_1 decrease significantly with age (NA_{t0} = 4.62e-10 [3.6e-10 7.56e-10] (m^2), NA_{t2} = 2.78e-10 [2.12e-10 3.96e-10], p_{NA} = 0.04; $W1_{t0}$ = 4.67e-07 [2.57e-07 7.09e-07] (m^2/s), $W1_{t2}$ = 2.57e-07 [1.74e-07 3.1e-07] (m^2/s), p_{W1} = 0.02). This suggests that the intensity of the forward wave, measured at the carotid arterial, decreases with age.

Vascular analysis includes the comparison between vascular-derived parameters, obtained from diameter and velocity signals, as well as the calculated AIx values. As shown in figure 7.9, the only significant changes can be observed for reID and AIx in TC1. While reID decreases with age ($reID_{t0}$ = 25.2 [24 32.9] (%), $reID_{t2}$ = 21.1 [18.9 23.7] (%), p_{reID} = 0.006), AIx increases (AIx_{t0} = 0.192 [0.115 0.223] (%), AIx_{t2} = 0.266 [0.199 0.319] (%), p_{AIx} = 0.03). Although less pronounced, change in diastolic diameter D_d is borderline significant (Dd_{t0} = 0.394 [0.374 0.422] (mm), Dd_{t2} = 0.428 [0.408 0.46] (mm), p_{Dd} = 0.06), while the systolic diameter remains unchanged.

Exemplarily, the change in AIx is shown in figures 7.10 and 7.11, where AIx plots from two wild

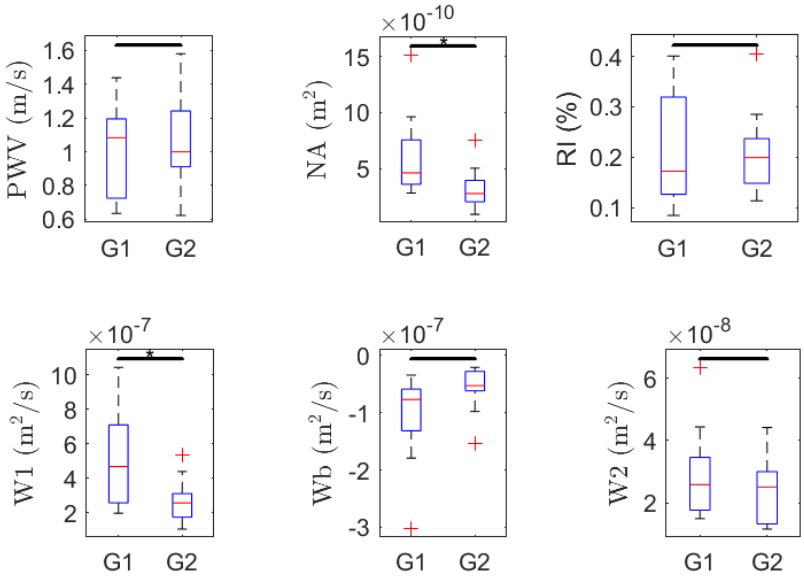

Figure 7.8: *Wave intensity analysis comparison for TC1.*

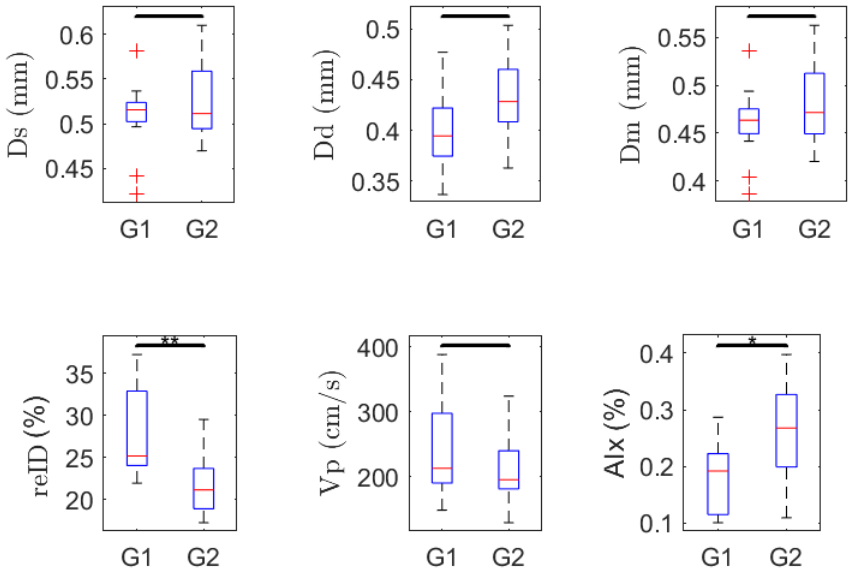

Figure 7.9: *Vascular comparison for TC1.*

type mice at t0 and t2 are illustrated. At the age of 25 weeks, the AIx is more than twice as high as AIx at the age of 8 weeks for mouse tm76 and even higher for tm66.

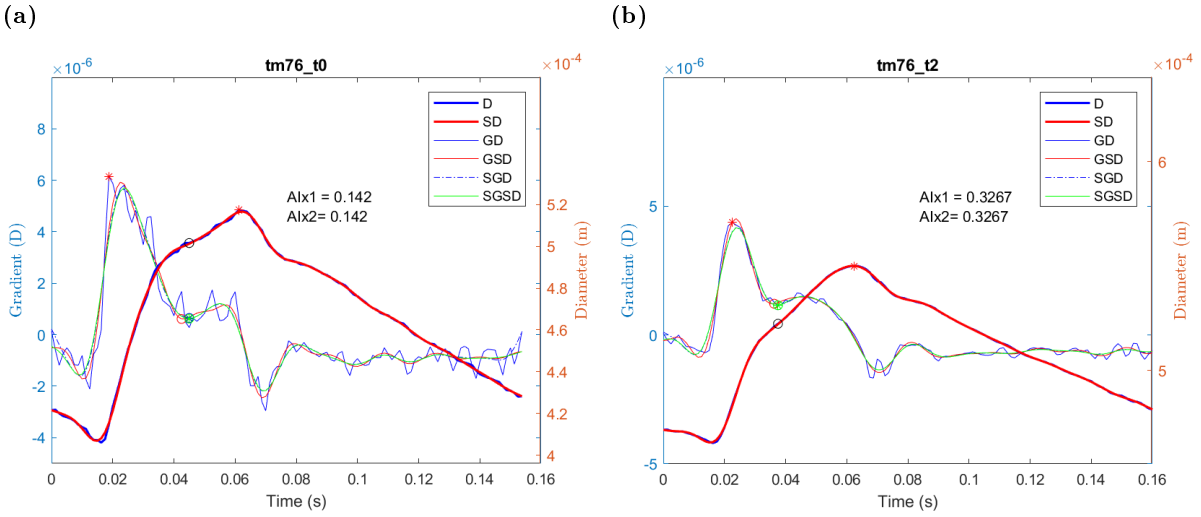

Figure 7.10: *Augmentation index algorithm performance comparison for the wild type mouse tm76 at the age of 8 weeks (a) and 25 weeks (b).*

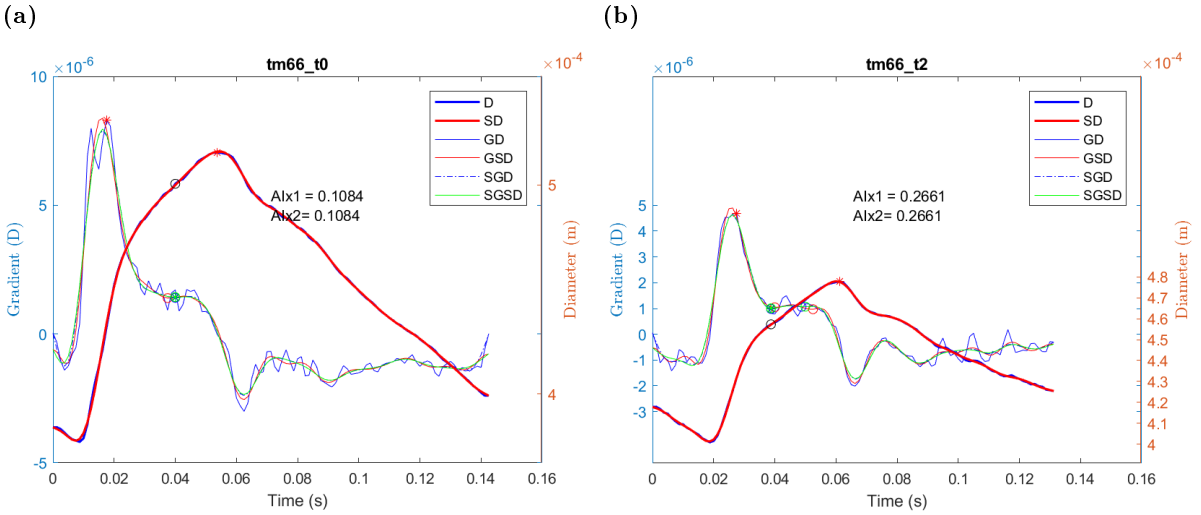

Figure 7.11: *Augmentation index algorithm performance comparison for the wild type mouse tm66 at the age of 8 weeks (a) and 25 weeks (b).*

	WT (t0)		ApoE		
Variables (units)	Median [IQR]	Mean (SD)	Median [IQR]	Mean (SD)	p
HR (bpm)	379 [346 405]	388 (87 SD)	340 [324 369]	352 (46.9 SD)	0.41
RR (bpm)	131 [111 156]	132 (26.1 SD)	117 [95.8 133]	113 (20.6 SD)	0.01
T (°C)	35.5 [35.1 35.6]	35.3 (0.687 SD)	34.8 [33.8 35.1]	34.6 (0.797 SD)	0.02
qt (s)	0.0237 [0.0226 0.0273]	0.024 (0.00446 SD)	0.0291 [0.0272 0.0315]	0.0305 (0.00551 SD)	0.01
qtc (s)	54.9 [50.4 61.1]	55.1 (5.65 SD)	58.5 [56.4 63.4]	59.6 (6.13 SD)	0.11
pq (s)	0.0404 [0.0347 0.0442]	0.0402 (0.0062 SD)	0.0417 [0.0309 0.0453]	0.0395 (0.00846 SD)	0.97
qrs (s)	0.0101 [0.0091 0.0112]	0.0101 (0.0014 SD)	0.0113 [0.0108 0.0147]	0.0127 (0.00269 SD)	0.01
rr (s)	0.162 [0.157 0.174]	0.166 (0.0186 SD)	0.18 [0.173 0.188]	0.178 (0.0191 SD)	0.38
Dm (mm)	0.463 [0.449 0.475]	0.459 (0.0373 SD)	0.472 [0.449 0.513]	0.483 (0.0414 SD)	0.19
Ds (mm)	0.516 [0.502 0.524]	0.508 (0.0402 SD)	0.511 [0.494 0.559]	0.525 (0.0425 SD)	0.27
Dd (mm)	0.394 [0.374 0.422]	0.397 (0.0372 SD)	0.428 [0.408 0.46]	0.432 (0.0394 SD)	0.06
reID (%)	25.2 [24 32.9]	28.1 (5.44 SD)	21.1 [18.9 23.7]	21.7 (3.79 SD)	0.006
Vp (cm/s)	21.3 [19 29.8]	23.9 (7.09 SD)	19.5 [18.1 24]	21.3 (5.86 SD)	0.31
AIx (%)	0.192 [0.115 0.223]	0.183 (0.061 SD)	0.266 [0.199 0.319]	0.254 (0.0754 SD)	0.03
PWV (m/s)	1.08 [0.725 1.2]	1.02 (0.269 SD)	1 [0.911 1.24]	1.05 (0.277 SD)	0.79
W1 (m^2/s)	4.67e-07 [2.57e-07 7.09e-07]	5.09e-07 (2.66e-07 SD)	2.57e-07 [1.74e-07 3.1e-07]	2.71e-07 (1.21e-07 SD)	0.02
W2 (m^2/s)	2.58e-08 [1.77e-08 3.46e-08]	2.9e-08 (1.37e-08 SD)	2.51e-08 [1.32e-08 3e-08]	2.33e-08 (1e-08 SD)	0.27
Wb (m^2/s)	-7.71e-08 [-1.32e-07 -5.9e-08]	-1.02e-07 (7.35e-08 SD)	-5.29e-08 [-6.2e-08 -2.82e-08]	-5.54e-08 (3.65e-08 SD)	0.08
NA (m^2)	4.62e-10 [3.6e-10 7.56e-10]	6.02e-10 (3.5e-10 SD)	2.78e-10 [2.12e-10 3.96e-10]	3.27e-10 (1.6e-10 SD)	0.04
RI (%)	0.172 [0.126 0.319]	0.219 (0.118 SD)	0.199 [0.148 0.237]	0.203 (0.0801 SD)	0.89

Table 7.1: *Comparison of physiological, ECG intervals, WIA-derived and vascular-derived parameters for TC1.*

7.3 TC2: Comparison between Young Wild Type and ApoE Mice

In a second comparison, TC2, young wild type mice (8 weeks old) have been compared to ApoE mice, twice as old (16 weeks old). Numerical results of applying a Wilcoxon rank-sum test are presented in table 7.2.

Boxplots obtained from physiological comparison are shown in figure 7.12. In this case, the results obtained behave exactly the opposite way as in TC1: all three parameters, i.e. the heart rate, the respiration rate and the temperature, are higher in the second group, of ApoE mice. However, changes are just significant for RR (RR_{WT} = 131 [111 156] (bpm), RR_{ApoE} = 159 [141 172] (bpm), p_{RR} = 0.04).

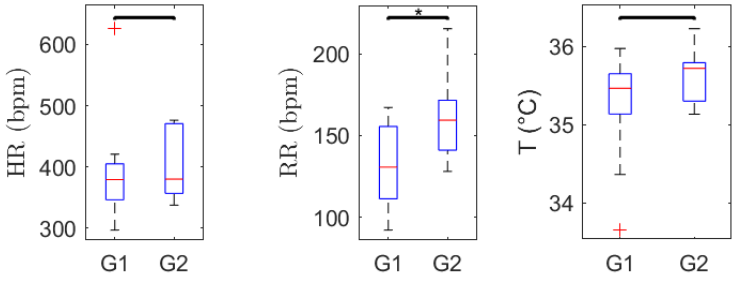

Figure 7.12: *Physiological comparison for TC2.*

Results for the ECG intervals analysis are illustrated in figure 7.13. None of the intervals change significantly between both types of mice. For example, rr-interval changes from rr_{WT} = 0.162 [0.157 0.174] (s) to rr_{ApoE} = 0.166 [0.127 0.17] (s) (p_{rr} = 0.36).

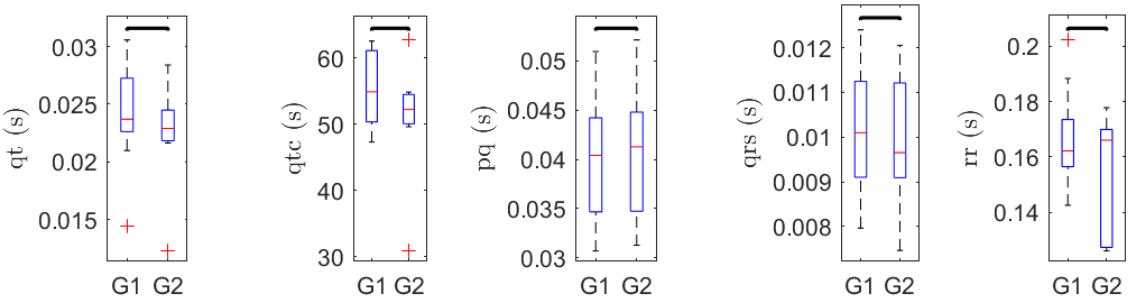

Figure 7.13: *ECG interval comparison for TC2.*

For TC2, the comparison graph corresponding to wave intensity analysis is shown in figure 7.14. Unlike in the previous test case, in TC2 W2 changes are now highly significant ($W2_{WT}$ = 2.58e-08 [1.77e-08 3.46e-08] (m^2/s), $W2_{ApoE}$ = 3.89e-08 [3.34e-08 5.72e-08] (m^2/s), p_{W2} = 0.008), while W1 remains unchanged ($W1_{WT}$ = 4.67e-07 [2.57e-07 7.09e-07] (m^2/s), $W1_{ApoE}$ = 4.77e-07 [2.49e-07 5.52e-07] (m^2/s), p_{W1} = 0.51). Furthermore, PWV is significantly increased for ApoE mice (PWV_{WT} = 1.08 [0.725 1.2] (m/s), PWV_{ApoE} = 1.72 [1.33 2.17] (m/s), p_{PWV} = 0.006).

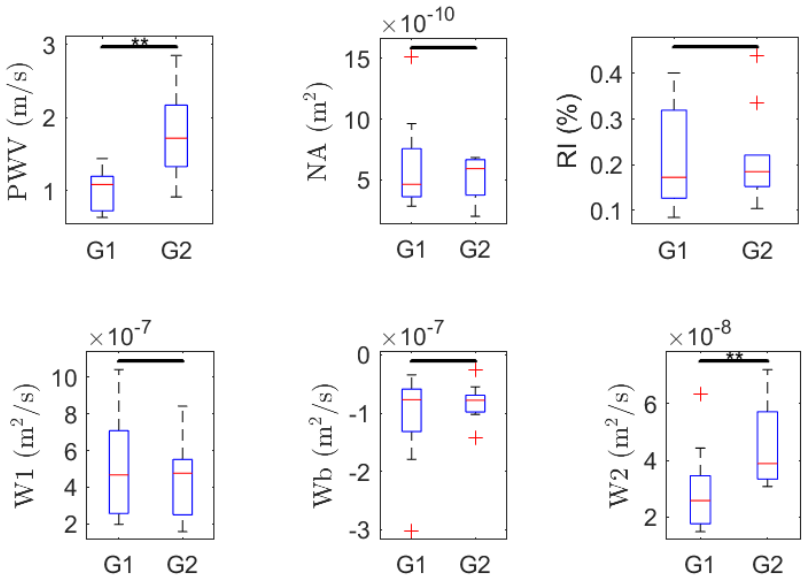

Figure 7.14: *Wave intensity analysis for TC2*

Consecutively, vascular analysis has been applied in TC2. Systolic diameter and mean diameter values show significant changes (Ds_{WT} = 0.516 [0.502 0.524] (mm), Ds_{ApoE} = 0.461 [0.449 0.482] (mm), p_{Ds} = = 0.004; Dm_{WT} = 0.463 [0.449 0.475] (mm), Dm_{ApoE} = 0.42 [0.413 0.441] (mm), p_{Dm} = 0.006), being higher for WT mice. For this reason, reID is also higher in wildtype mice ($reID_{WT}$ = 25.2 [24 32.9] (%), $reID_{ApoE}$ = 23.5 [20.7 25.7] (%), p_{reID} = 0.04). On the contrary, blood flow velocity peak, denoted by Vp, is significantly higher for ApoE mice (Vp_WT = 21.3 [19 29.8] (cm/s), Vp_ApoE = 36.7 [28 42.5] (cm/s), p_Vp = 0.005). AIx difference is not significant.

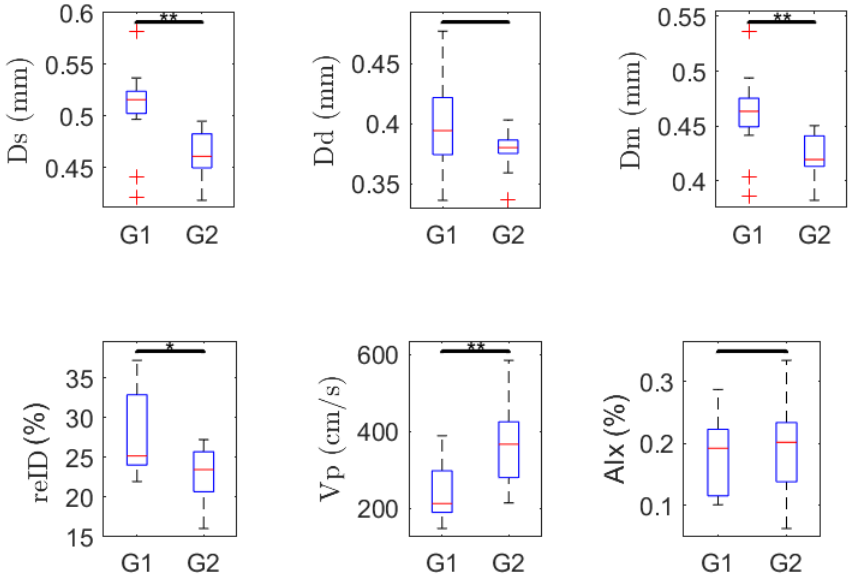

Figure 7.15: *Vascular comparison for TC2.*

Exemplarily, two comparisons of the augmentation index calculation for a wild type and an ApoE mouse are shown in figures 7.16 and 7.17. The first comparison is made between mice whose AIx values are similar to the median of this parameter of their group. Hence, one can not see big differences between waves from figures 7.16a and 7.16a. However, in the second comparison, AIx values are much higher in the ApoE mouse (figure 7.17b) than in the wild type mouse tm65 (figure 7.17a).

(a) **(b)**

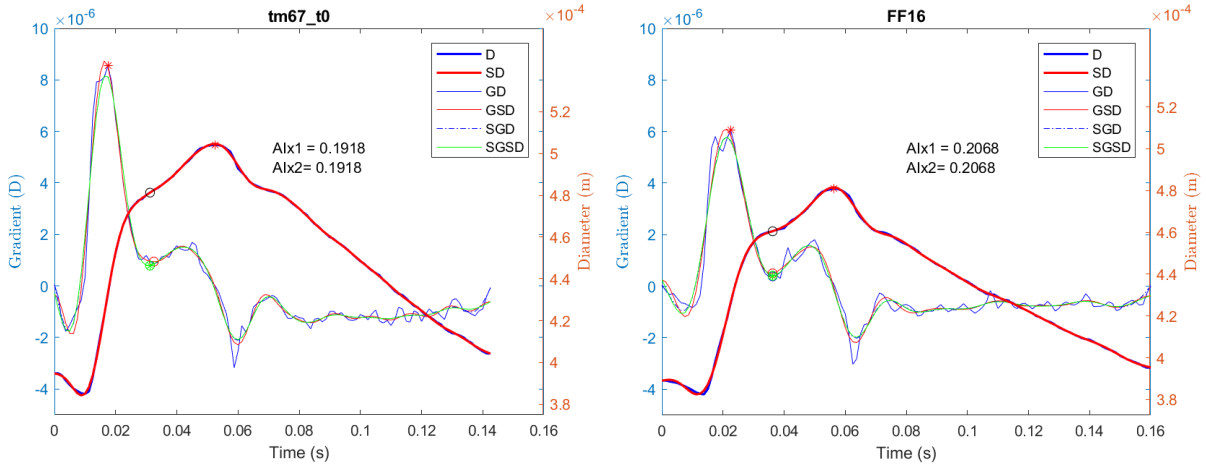

Figure 7.16: *Augmentation index algorithm performance between a wild type mouse and an ApoE mouse with similar AIx values: mouse tm67 at the age of 8 weeks (a) and mouse FF16 at the age of 16 weeks (b).*

(a) **(b)**

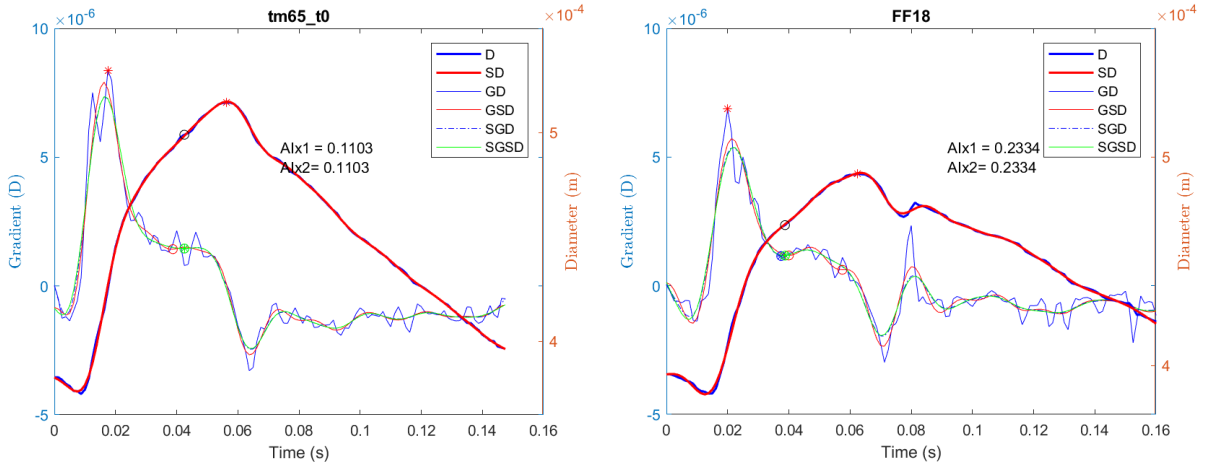

Figure 7.17: *Augmentation index algorithm performance between a wild type mouse and an ApoE mouse with different AIx values: mouse tm65 at the age of 8 weeks (a) and mouse FF18 at the age of 16 weeks (b).*

	WT (t0)		ApoE		
Variables (units)	Median [IQR]	Mean (SD)	Median [IQR]	Mean (SD)	p
HR (bpm)	379 [346 405]	388 (87 SD)	380 [357 471]	400 (56.7 SD)	0.46
RR (bpm)	131 [111 156]	132 (26.1 SD)	159 [141 172]	160 (24.9 SD)	0.04
T (°C)	35.5 [35.1 35.6]	35.3 (0.687 SD)	35.7 [35.3 35.8]	35.6 (0.337 SD)	0.22
qt (s)	0.0237 [0.0226 0.0273]	0.024 (0.00446 SD)	0.0229 [0.0218 0.0245]	0.0225 (0.00437 SD)	0.45
qtc (s)	54.9 [50.4 61.1]	55.1 (5.65 SD)	52.2 [50.1 54.5]	50.9 (9.06 SD)	0.42
pq (s)	0.0404 [0.0347 0.0442]	0.0402 (0.0062 SD)	0.0413 [0.0347 0.0448]	0.0406 (0.00696 SD)	0.90
qrs (s)	0.0101 [0.0091 0.0112]	0.0101 (0.0014 SD)	0.00965 [0.00909 0.0112]	0.00991 (0.00149 SD)	0.75
rr (s)	0.162 [0.157 0.174]	0.166 (0.0186 SD)	0.166 [0.127 0.17]	0.154 (0.0213 SD)	0.36
Dm (mm)	0.463 [0.449 0.475]	0.459 (0.0373 SD)	0.42 [0.413 0.441]	0.423 (0.0204 SD)	0.006
Ds (mm)	0.516 [0.502 0.524]	0.508 (0.0402 SD)	0.461 [0.449 0.482]	0.464 (0.0242 SD)	0.004
Dd (mm)	0.394 [0.374 0.422]	0.397 (0.0372 SD)	0.38 [0.375 0.387]	0.377 (0.018 SD)	0.23
reID (%)	25.2 [24 32.9]	28.1 (5.44 SD)	23.5 [20.7 25.7]	22.9 (3.35 SD)	0.04
Vp (cm/s)	21.3 [19 29.8]	23.9 (7.09 SD)	36.7 [28 42.5]	37 (10.7 SD)	0.005
AIx (%)	0.192 [0.115 0.223]	0.183 (0.061 SD)	0.201 [0.138 0.233]	0.193 (0.0855 SD)	0.83
PWV (m/s)	1.08 [0.725 1.2]	1.02 (0.269 SD)	1.72 [1.33 2.17]	1.73 (0.625 SD)	0.006
W1 (m^2/s)	4.67e-07 [2.57e-07 7.09e-07]	5.09e-07 (2.66e-07 SD)	4.77e-07 [2.49e-07 5.52e-07]	4.48e-07 (2.17e-07 SD)	0.51
W2 (m^2/s)	2.58e-08 [1.77e-08 3.46e-08]	2.9e-08 (1.37e-08 SD)	3.89e-08 [3.34e-08 5.72e-08]	4.66e-08 (1.52e-08 SD)	0.008
Wb (m^2/s)	-7.71e-08 [-1.32e-07 -5.9e-08]	-1.02e-07 (7.35e-08 SD)	-7.81e-08 [-9.82e-08 -6.95e-08]	-8.11e-08 (3.1e-08 SD)	0.88
NA (m^2)	4.62e-10 [3.6e-10 7.56e-10]	6.02e-10 (3.5e-10 SD)	5.92e-10 [3.73e-10 6.66e-10]	5.32e-10 (1.68e-10 SD)	0.93
RI (%)	0.172 [0.126 0.319]	0.219 (0.118 SD)	0.185 [0.152 0.221]	0.209 (0.104 SD)	0.93

Table 7.2: *Comparison of physiological, ECG intervals, WIA-derived and vascular-derived parameters for TC2.*

7.4 TC3: Comparison between Young Wild Type and db/db Mice

The third test case, TC3, compares a sample of 8 weeks young wild type mice with a sample of db/db mice, who suffer from diabetes, 5 weeks older (13 weeks old). Numerical results from the non-parametric test applied considering unpaired samples are found in table 7.3.

In this case, the physiological analysis shows a significant lower heart rate (HR_{WT} = 379 [346 405] (bpm), $HR_{db/db}$ = 328 [285 335] (bpm), p_{HR} = 0.01) and temperature (T_{WT} = 35.5 [35.1 35.6] (ºC), $T_{db/db}$ = 34.2 [33.9 35] (ºC), p_T = 0.01) for the second group of mice, db/db. This time, however, the change in respiration rate is not significant in comparison to TC1 and TC2 (RR_{WT} = 131 [111 156] (bpm), $RR_{db/db}$ = 152 [139 166] (bpm), p_{RR} = 0.22).

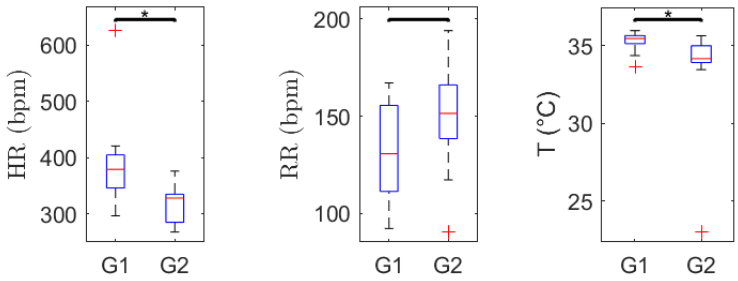

Figure 7.18: *Physiological comparison for TC3.*

Boxplots corresponding to the ECG intervals analysis are illustrated in figure 7.19. The lower heart rate in db/db mice is related with the higher rr-interval, which shows a significant change (rr_{WT} = 0.162 [0.157 0.174] (s), $rr_{db/db}$ = 0.183 [0.179 0.209] (s), p_{rr} = 0.01). The qt-interval is also significantly higher in diabetes mice (qt_{WT} = 0.0237 [0.0226 0.0273] (s), $qt_{db/db}$ = 0.0284 [0.0268 0.0295] (s), p_{qt} = 0.02).

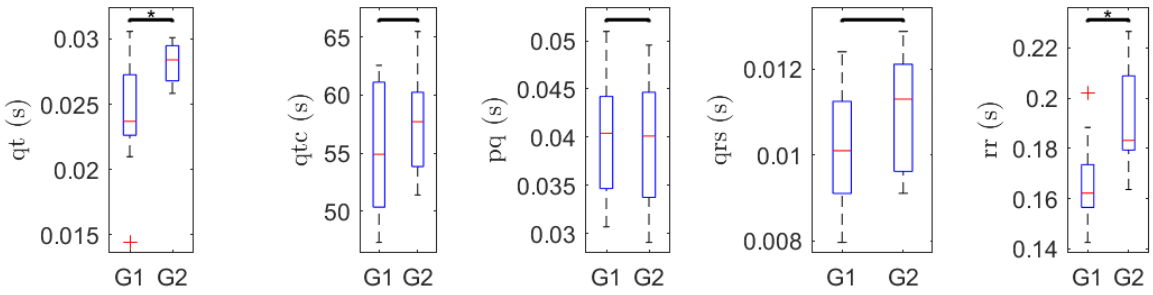

Figure 7.19: *ECG interval comparison for TC3.*

Boxplots from wave intensity analysis comparison are shown in figure 7.20. PWV is significantly higher in unhealthy mice (PWV_{WT} = 1.08 [0.725 1.2] (m/s), $PWV_{db/db}$ = 1.47 [1.21 2.02] (m/s), p_{PWV} = 0.003). The change in the magnitude of W1 is higly significant in this test case, being

lower for diabetes mice ($W1_{WT}$ = 4.67e-07 [2.57e-07 7.09e-07] (m^2/s), $W1_{db/db}$ = 1.57e-07 [1.26e-07 2.46e-07] (m^2/s), p_{W1} = 0.002), related to the strong decrease in the absolute magnitude of reflected waves, meassured by Wb (Wb_{WT} = -7.71e-08 [-1.32e-07 -5.9e-08] (m^2/s), $Wb_{db/db}$ = -2.67e-08 [-4.2e-08 -2.4e-08] (m^2/s), $p_{Wb} < 0.001$). As a result, the change in the negative area is significant as well, being lower for db/db mice than for WT mice (NA_{WT} = 4.62e-10 [3.6e-10 7.56e-10] (m^2), $NA_{db/db}$ = 2.36e-10 [1.97e-10 3e-10] (m^2), $p_{NA} < 0.001$).

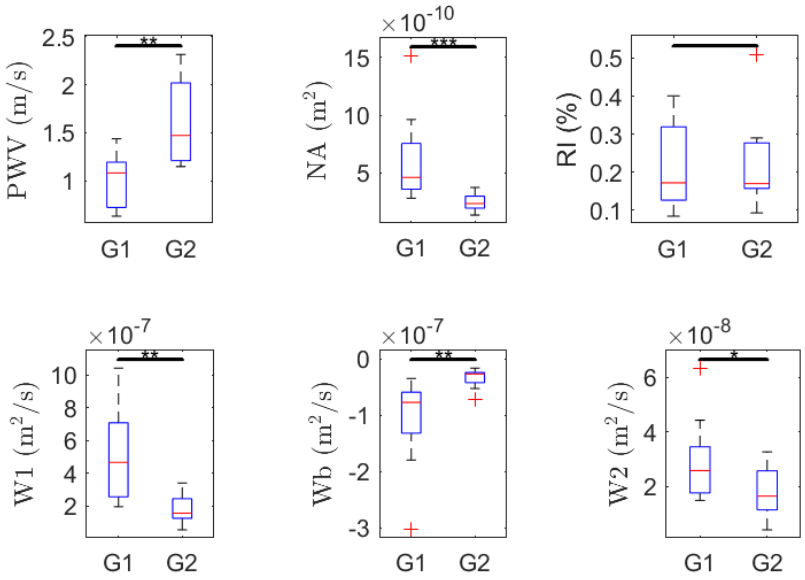

Figure 7.20: *Wave intensity analysis for TC3*

Comparison of parameters from vascular analysis applied for TC3 is illustrated in figure 7.21. Similarly to TC1, the most significant changes are found in reID ($reID_{WT}$ = 25.2 [24 32.9] (%), $reID_{db/db}$ = 18.6 [16.7 21.4] (%), p_{reID} = 0.003) and AIx (AIx_{WT} = 0.192 [0.115 0.223] (%), $AIx_{db/db}$ = 0.336 [0.266 0.382] (%), $p_{AIx} < 0.001$).

Change in blood flow velocity is borderline significant (Vp_{WT} = 21.3 [19 29.8] (cm/s), $Vp_{db/db}$ = 16.7 [15.5 20] (cm/s), p_{Vp} = 0.05). However, in this test case diameter changes between wild type and diabetes mice are not significant.

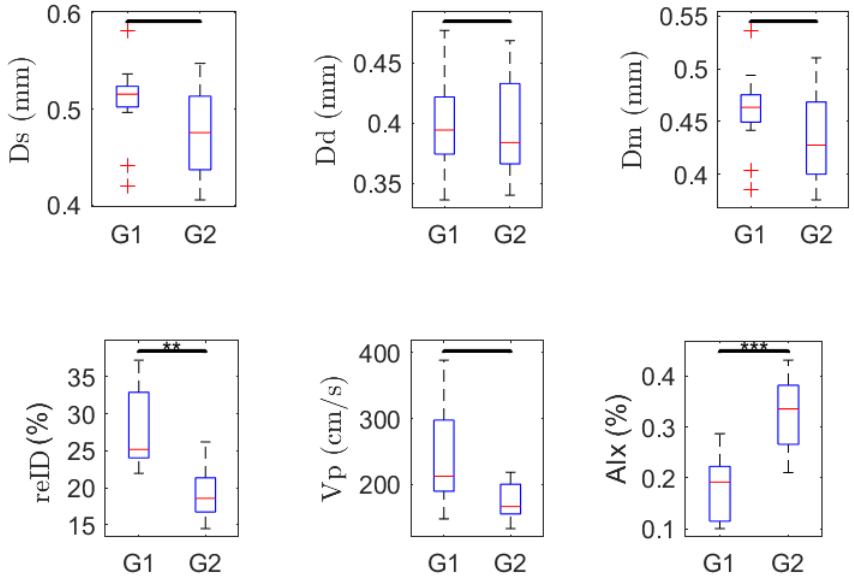

Figure 7.21: *Vascular comparison for TC3.*

	WT (t0)		ApoE		
Variables (units)	Median [IQR]	Mean (SD)	Median [IQR]	Mean (SD)	p
HR (bpm)	379 [346 405]	388 (87 SD)	328 [285 335]	316 (36 SD)	0.01
RR (bpm)	131 [111 156]	132 (26.1 SD)	152 [139 166]	148 (30 SD)	0.22
T (°C)	35.5 [35.1 35.6]	35.3 (0.687 SD)	34.2 [33.9 35]	33.3 (3.91 SD)	0.01
qt (s)	0.0237 [0.0226 0.0273]	0.024 (0.00446 SD)	0.0284 [0.0268 0.0295]	0.0281 (0.00154 SD)	0.02
qtc (s)	54.9 [50.4 61.1]	55.1 (5.65 SD)	57.7 [53.8 60.2]	57.5 (4.53 SD)	0.34
pq (s)	0.0404 [0.0347 0.0442]	0.0402 (0.0062 SD)	0.0401 [0.0338 0.0447]	0.0395 (0.00692 SD)	0.97
qrs (s)	0.0101 [0.0091 0.0112]	0.0101 (0.0014 SD)	0.0113 [0.00962 0.0121]	0.0109 (0.00143 SD)	0.32
rr (s)	0.162 [0.157 0.174]	0.166 (0.0186 SD)	0.183 [0.179 0.209]	0.192 (0.0212 SD)	0.01
Dm (mm)	0.463 [0.449 0.475]	0.459 (0.0373 SD)	0.428 [0.4 0.469]	0.437 (0.0455 SD)	0.29
Ds (mm)	0.516 [0.502 0.524]	0.508 (0.0402 SD)	0.476 [0.437 0.513]	0.475 (0.0475 SD)	0.12
Dd (mm)	0.394 [0.374 0.422]	0.397 (0.0372 SD)	0.384 [0.366 0.433]	0.398 (0.0429 SD)	0.89
reID (%)	25.2 [24 32.9]	28.1 (5.44 SD)	18.6 [16.7 21.4]	19.3 (4 SD)	0.003
Vp (cm/s)	21.3 [19 29.8]	23.9 (7.09 SD)	16.7 [15.5 20]	17.6 (2.84 SD)	0.05
AIx (%)	0.192 [0.115 0.223]	0.183 (0.061 SD)	0.336 [0.266 0.382]	0.328 (0.0758 SD)	$<$0.001
PWV (m/s)	1.08 [0.725 1.2]	1.02 (0.269 SD)	1.47 [1.21 2.02]	1.6 (0.435 SD)	0.003
W1 (m^2/s)	4.67e-07 [2.57e-07 7.09e-07]	5.09e-07 (2.66e-07 SD)	1.57e-07 [1.26e-07 2.46e-07]	1.81e-07 (9.2e-08 SD)	0.002
W2 (m^2/s)	2.58e-08 [1.77e-08 3.46e-08]	2.9e-08 (1.37e-08 SD)	1.65e-08 [1.15e-08 2.58e-08]	1.74e-08 (9.72e-09 SD)	0.05
Wb (m^2/s)	-7.71e-08 [-1.32e-07 -5.9e-08]	-1.02e-07 (7.35e-08 SD)	-2.67e-08 [-4.2e-08 -2.4e-08]	-3.45e-08 (1.73e-08 SD)	0.001
NA (m^2)	4.62e-10 [3.6e-10 7.56e-10]	6.02e-10 (3.5e-10 SD)	2.36e-10 [1.97e-10 3e-10]	2.45e-10 (7.29e-11 SD)	$<$0.001
RI (%)	0.172 [0.126 0.319]	0.219 (0.118 SD)	0.17 [0.157 0.277]	0.221 (0.124 SD)	0.95

Table 7.3: *Comparison of physiological, ECG intervals, WIA-derived and vascular-derived parameters for TC3.*

CHAPTER 8

Discussion, Conclusion and Outlook

In this thesis, different algorithms have been implemented for the analysis of pulse wave and ECG recordings in mice. Thereafter, algorithms have been evaluated and applied to different groups of mice.

8.1 Discussion

The purpose of this thesis is to provide a solution that automatically calculates different cardiovascular parameters to be applied in mice. Therefore, one can compare different groups of mice in order to assess the influence of aging or to evaluate the effect of different diseases in the cardiovascular system.

In this section, results of applying the algorithms to the three different test cases are discussed in order to test changes due to age (TC1), assess the influence of atherosclerosis (TC2) and analyze the influence of diabetes in different parameters.

When comparing our results with values from N. D. Lascio et al. [6] in TC1, discrepancies can be due to the different numbers of mice involved. While N. D. Lascio et al. evaluates results from 16 wild type mice, for the present study, physiological data from only 11 mice was available. Besides, diameter and blood flow velocity recordings from 13 mice was available.

Changes in HR are not significant in TC1 and TC2. A similar heart rate between wild type and ApoE mice was already noticed by C. J. Hartley et al. [25], although comparing age matched groups of mice (13 weeks old). Heart rate is significanty lower in db/db mice. In humans, it has been demonstrated that individuals with increased heart rate are more likely to develop diabetes [158]. A similar behaviour has been observed in mice with a great level of developed atherosclerosis, dKO, which also present a significantly lower HR than WT mice [88]. However, the relationship of this parameter with diabetes remains unclear. Previous studies in db/db mice show controversial results, since it has been reported that HR increases [159], decreases

[160, 161], and stays unaltered [162] in diabetes mice in comparison to controls. Thus, it is not possible to establish further conclusions about this parameter.

Respiration rate shows a significant decrease with age for wild type mice. This behaviour is also noticeabe in human, for it is known that respiration rate decreases with age (from 20-40 bpm in infants to 12-20 bpm in adults) [163]. Despite being older, ApoE mice present a significantly higher RR, but since the relationship between respiratory function and arterial stiffness has not been deeply studied, further studies would be necessary before to draw conclusions. For db/db mice, changes in this parameter are not significant. Yet, since standard respiration rate in mice goes from 80-230 breaths per minute (bpm) [65], RR obtained for both groups of unhealthy mice can be considered normal.

Temperature shows a significant decrease with age in wild type mice. This behaviour has been observed previously in healthy mice [164, 165]. Temperature is again significantly lower in db/db mice in comparison to 5 weeks younger mice. However, this might not only be due to aging, since there is an established relationship between insulin and a low core body temperature [166], a sign of type 1 diabetes. Despite being much older, however, ApoE mice do not show a significant difference in this parameter in comparison to young wild type mice. Nevertheless, no relationship has been found between temperature and atherosclerosis disease.

Concerning the ECG intervals, there is a significant increase with age (TC1) in the qrs-complex and thus, in the qt-interval, despite the fact that the duration of the heart beat remains unchanged. Meanwhile, there is no significant difference between intervals from young wild type and ApoE mice. However, one can notice an increase in rr-interval for ApoE mice, which is not expected, since the heart rate calculated before was higher in these mice. Even if not significantly changed, the duration of a heart beat should be shorter for ApoE mice. This can be explained by the fact that the ECG algorithm does not work properly for every case. If this happens, data from a lower number of mice is used in the comparison, and therefore, results can show a different behaviour than one would expect. Diabetes mice, on the contrary, present a longer heart beat reflected in a higher rr-interval (in seconds) in comparison to wild type mice, related to the significantly lower HR in unhealthy ice. The change, however, only affects the duration of the T-wave, and not the qrs-complex.

While increase in PWV due to aging is not noticeable in relatively young healthy mice (TC1), it is significantly higher in old atherosclerosis mice in comparison to young mice (TC2). This behaviour was previously observed, for example, by Y.-X. Wang et al. (4 monts old WT mice verus 13 month old ApoE mice) [82] and by V. Herold et al. [34] (2 month old WT mice versus 8 month old fat diet ApoE mice). However, A. K. Reddy et al. did demonstrate the increase of arterial stiffness with age in much older wild type mice (i.e. 8 month old (WT) versus 29 month old (WT)) than ours [52]. This can be explained by the fact that ApoE is an atherosclerosis mouse model characterized with a high arterial stiffness and PWV being the gold standard

measure for arterial stiffness. Besides, in humans diabetes has been reported to be associated with a high arterial stiffness [167]. This explains the results from TC3, where old diabetes mice present a significantly higher PWV in comparison to young wild type mice.

In wild type mice, the lower magnitude of W1 in old mice suggests that the intensity of the forward wave, measured at the carotid artery, decreases with age. Experiments have shown that W1 is directly correlated with the maximum rate of LV pressure and can represent an index of LV myocardial contraction capability [168]. Therefore, this result indicates a reduction in the cardiac performance, as N. D. Lascio et al. stated [6]. In constrast to results from N. D. Lascio et al., p-values W2 are not significant, and changes in Wb are only borderline significant. An explanation can be an incomplete dataset (different numbers of mice, see coment above). The disminution of the amplitude of the forwarding component is responsible for the reduction of the magnitude of reflected waves coming from head and neck in older mice. The small change in Wb is enough to cause a significant decrease in the NA. For TC2, only changes in W2 are significant. This forward expansion wave, generated by the simultaneous decrease in pressure and flow velocity, is inversely correlated with the time constant of LV relaxation and can be associated with LV function during late systolic ejection [169]. An increase in its magnitude can result in an earlier closure of the aortic valve and the subsequent stop of the LV ejection. In TC3, wave intensity parameters are in general significantly lower for diabetes mice than for wild type mice. However, due to the simultaneous change in Wb and W1, RI remains unchanged. The W1 amplitude not only decreases with age, but is also significantly lower in diabetes mice.

For TC1, the high significant change in reID is mainly due to the difference in diastolic diameter (borderline significant). The increase in diastolic diameter while systolic diameter remains unchanged suggests that the carotid artery dilates with age, provoking a significant reduction of the distension capability of the artery. This behaviour was also observed in the study of N. D. Lascio et al. [6]. In TC2, for a similar diastolic diameter, systolic diameter is substantially smaller in ApoE mice. This might be due to the high arterial stiffness of these mice. Therefore, the distension capability is also lower in atherosclerosis mice than in young wild type mice. For diabetes mice, although differences in systolic and diastolic diameters are almost not noticeable, the lower systolic diameter in db/db mice is enough to be responsible of a significantly lower distension capability in comparison with wild type mice. One can notice that both groups, ApoE and db/db, show lower systolic diameter values in comparison to wild type mice. This can be related to the fact that a high level of atherosclerosis significantly decreases systolic blood pressure, demonstrated by A. Braun et al. [88].

Blood flow velocity is negatively influenced by wave reflection, as previously observed by Y.-X. Wang and C. J. Hartley et al. [25]. This behaviour can be observed in results from N. D. Lascio et al., where V_p is significantly lower in old wild type mice [6]. However, results in TC1 show similar Vp values for young and old mice. This is probably because of the small size of the sample. In the evaluated mice, reflected waves do not arrive early enough to cause a significant

decrease in the blood flow in old wild type mice. This can also be due to the fact that magnitude of reflections, measured by Wb, is similar between young and old mice. Besides, in TC2, diameterer is significantly smaller in artherosclerosis mice. This, together with the higher blood velocity, contributes to the high PWV observed in ApoE mice in comparison to wild type mice. High blood flow velocity peak in atherosclerosis mice was already observed by Y.-X. Wang et al. in 2005 [53]. In TC3, due to the high influence of reflected waves in early systole measured by PWV and AIx parameters, blood flow velocity decreases (although only borderline significantly), which corroborates the previous hypothesis: a decrease in blood flow due to backward components is only noticeable when these reflected waves are of high magnitude.

Regarding the change in augmentation index, this parameter mainly reflects an earlier arrival in systole of reflected waves. If more than one inflection point is detected, they probably show reflections coming from different bifurcations.

In TC1, although wild type mice at both ages show an early arrival of reflected waves (type B signals), the AIx is significantly higher in old mice. This behaviour was as well reported by C. J. Hartley et al.[133] and A. K. Reddy et al. [52]. In TC2, despite the fact that ApoE mice present higher arterial stiffness, AIx values from these mice are similar to those from young wild type mice. However, as one can see, AIx varies from lower values (near 0.1 %) to high values (near 0.25 %) in both samples of mice. On the contrary, for similar diameters, C. J. Hartley et al. observed a significatly higher AIx in ApoE mice. Besides, for a significantly lower diameter, the group observed similar AIx values between ApoE and old wild type mice [133]. In diabetes mice, where diameters of the artery are similar to the ones from young wild type mice, one can notice a correlation between AIx and PWV values, concluding that arterial stiffness is higher in db/db mice than in ApoE mice. In general, there are controversial discussion going on if AIx is a good measure of vascular stiffness and for the assessment of wave reflections [170–174].

An important limitation of the presented study is the lacking data of several mice in TC1 to allow for a precise comparison with results from N. D. Lascio et al. [6]. Finally, this thesis was limited by the age mismatch of ApoE and db/db mice in TC2 and TC3, respectively.

In conclusion, this thesis presents an algorithm for the automatic determination of various cardiovascular, hemodynamic parameters based on non-invasive recording in mice. Results are promising and allow further investigations.

8.2 Outlook

Along this thesis, four different groups of mice have been evaluated. However, to study more precisely the effect of aging, it would be optimal to have as well data from young ApoE and db/db mice (i.e., same age as WT controls).

The main application of the program is the examination and comparison of different kinds of mice in order to study the change in the properties of the vessels. For example, compliance of the vessels could be assessed in a further step, if data from α-SMA$^{(-/-)}$ mice was provided. Diameter changes and AIx values from these mice could be compared to values from C. J. Hartley et al. [133]. Other possible applications of the program are the testing of medical treatments and the early detection of a certain disease like Alzheimer, as well as the evaluation of its evolution, or the effect of exercise in specific groups of mice.

A possible improvement of the program would be to allow the multiple comparison of different groups of mice (for values see appendix B). Moreover, the assessment of other parameters as heart rate variability, input or characteristic impedance could be implemented. The assessment of the acceleration (A2/A1 ratio) could be of help to evaluate changes in blood flow velocity due to wave reflections. In the case of the AIx algorithm, a future improvement could be its adaptation to detect the inflection point in diameter signals of type C. This could be necessary in case of evaluating wild type mice younger than 8 weeks.

It is important to notice that the augmentation index does not take into account differences in the time till the left ventricular ejection reaches its maximum (maximum systolic diameter) for different kinds of mice. This fact hampers the detection of an earlier arrival of reflected waves in cases where AIx values were similar but mice presented a different ejection duration (ED). Thus, the augmentation index only allows to calculate the contribution of reflected waves to the total wave. To correctly identify high arterial stiffness measured by the augmentation index, the calculus of the ED could be of help in order to scale diameter or pulse wave signals from different kinds of mice.

Furthermore, a study could be carried out in order to assess the influence of blood pressure on the change of PWV, similarily to the one from Fitch et al. in 2001 [60]. However, we would evaluate the impact of diameter changes instead, as we are using diameter signals to calculate the PWV.

Appendices

APPENDIX A

Data for Algorithms Validation

Some of the implemented algorithms in this thesis were validated using alternative methods. Values obtained with these algorithms are presented here.

A.1 Heart Beat Duration

The heart rate algorithm was validated with the ECG murice algorithm. Heart beat (hb) duration values obtained with the HR algorithm for wild type mice at t0 and t2 are compared to the rr-interval obtained by the ECG murine algorithm in tables A.1 and A.2 respectively.

ID	HR alg.	ECG alg.
tm65_t0	0.156	0.156
tm66_t0	0.146	0.145
tm67_t0	0.143	0.143
tm68_t0	0.167	0.166
tm69_t0	0.157	0.157
tm70_t0	0.202	0.202
tm71_t0	0.172	0.172
tm72_t0	0.174	0.174
tm73_t0	0.188	0.188
tm76_t0	0.158	0.158
tm77_t0	0.096	NaN

Table A.1: *Heart beat duration, in seconds, for wild type mice at 8 weeks of age.*

ID	HR alg.	ECG alg.
tm65_t2	0.197	0.195
tm66_t2	0.135	0.135
tm67_t2	0.202	0.202
tm68_t2	0.140	NaN
tm69_t2	0.185	0.185
tm70_t2	0.174	0.174
tm71_t2	0.180	0.180
tm72_t2	0.185	0.184
tm73_t2	0.177	0.177
tm76_t2	0.161	NaN
tm77_t2	0.168	0.168

Table A.2: *Heart beat duration,, in seconds, for wild type mice at 25 weeks of age.*

As one can see, the ECG algorithm does not always provide a valid result. Figure A.1 shows an example where this occurs. The wild type mouse tm77 has been analyzed with the HR algorithm (figure A.1a) and the ECG algorithm (figure A.1b). These signals have been amplified in figure A.2. Probably, the high level of noise found in this case is responsible for the altered shape of

the ECG signal. It presents a J-peak sometimes of higher magnitude than the R-peak.

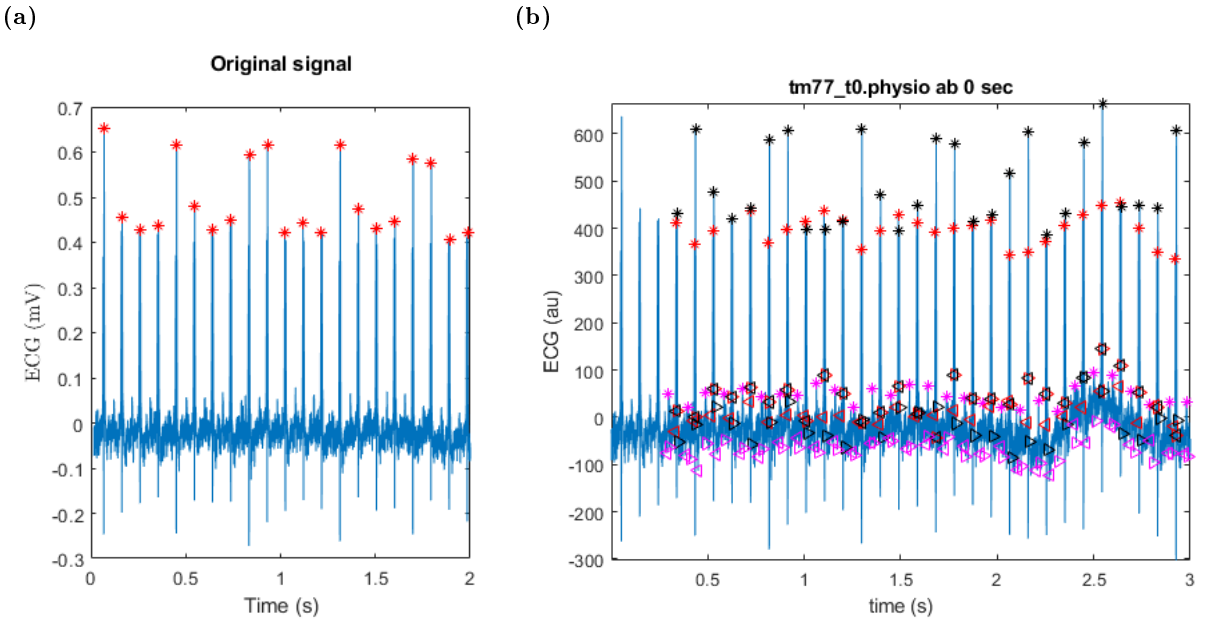

Figure A.1: *ECG signal of the wild type mouse tm77. R-peak detection by HR-algorithm (a) and by ECG murine algorithm (b).*

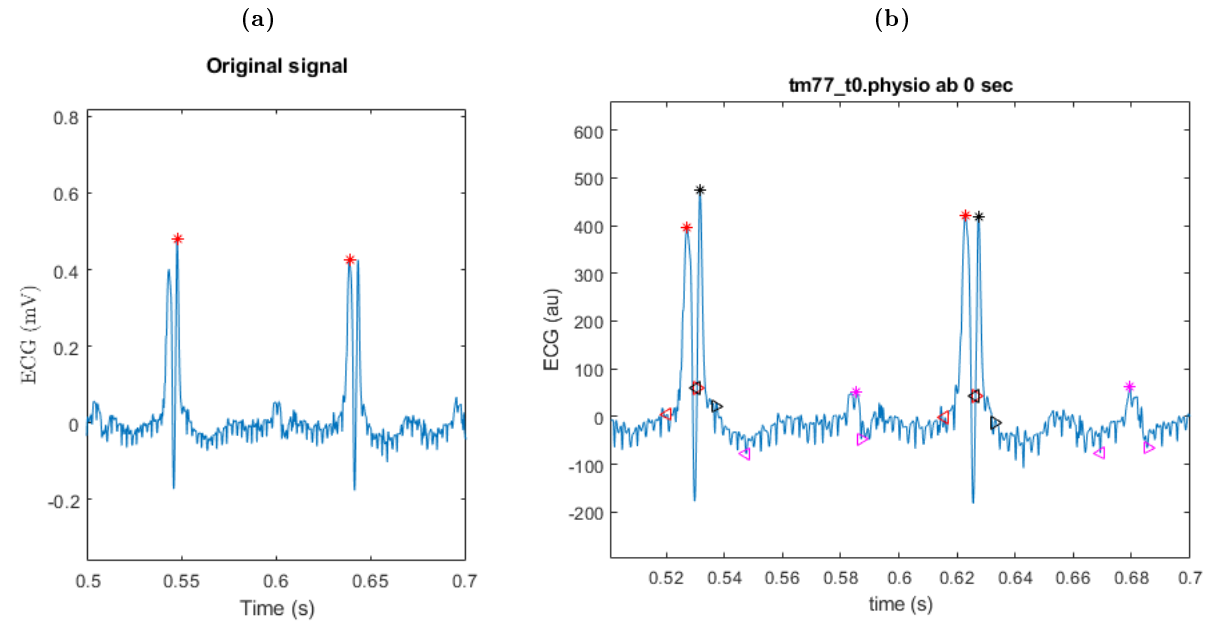

Figure A.2: *Amplified ECG signal of the wild type mouse tm77. R-peak detection by HR-algorithm (a) and by ECG murine algorithm (b).*

Table A.3 contains values from ApoE mice and table A.4, from db/db mice. Again, the case where the ECG murine algorithm returns NaN correspond to a signal with a high level of interference.

This only happens for the unhealthy ApoE mouse FF34, whose ECG is illustrated in figures A.3a and A.3b. This difficults the task of identifiying the R-peaks and thus, the rr-intervals.

ID	HR alg.	ECG alg.
FF12	0.178	0.178
FF16	0.165	0.166
FF17	0.151	0.151
FF18	0.168	0.170
FF24	0.176	0.172
FF26	0.127	0.127
FF33	0.126	0.126
FF34	0.140	NaN
FF35	0.16537	0.166
FF43	0.1275	0.128

Table A.3: *Heart beat duration, in seconds, for ApoE mice at 16 weeks of age.*

ID	HR alg.	ECG alg.
AS05	0.182	0.182
AS06	0.221	0.218
AS07	0.182	0.182
AS12	0.224	0.226
AS13	0.172	0.172
AS14	0.207	0.206
AS19	0.197	0.198
AS20	0.159	0.164
AS21	0.183	0.183

Table A.4: *Heart beat duration, in seconds, for db/db mice at 13 weeks of age.*

(a)

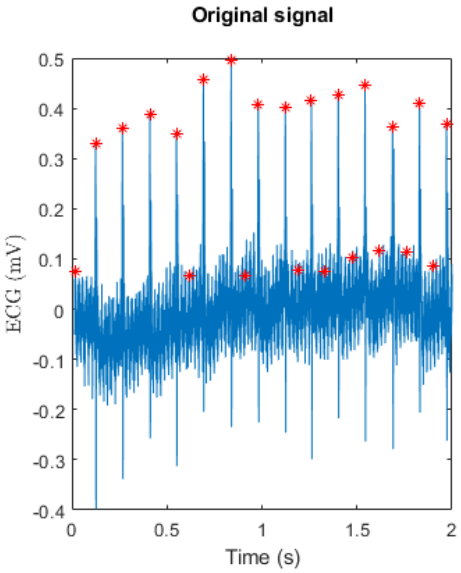

(b)

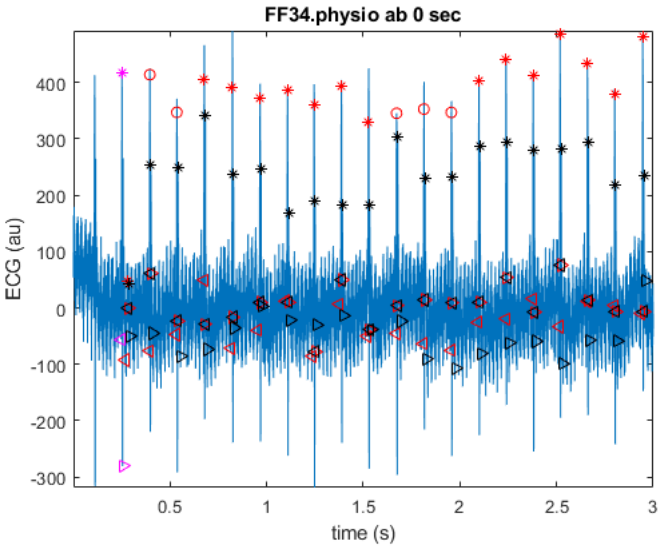

Figure A.3: *ECG signal of the ApoE mouse FF34. R-peak detection by HR-algorithm (a) and by ECG murine algorithm (b).*

As one can see, using the Matlab function *findpeaks* in the heart rate algorithm would also not provide a good result. Signals are too noisy and this causes a wrong identification of the R-peaks with this method. However, in this thesis the heart beat duration is calculated by means of the autocorrelation function.

A.2 Pulse Wave Velocity

The results of the pulse wave velocity algorithm were compared to those provided by N. D. Lascio. For wild type mice, values from two subjects were missing (wild type mice tm74 and tm75). However, PWV was calculated to be used in the comparison tests. Results from applying the PWV algorithm to the different groups of mice are shown in the following tables, together with the corresponding values from N. D. Lascio. Tables A.5 and A.6 contain PWV values from wild type mice at the age of 8 and 25 weeks, respectively. In table A.7, PWV values from ApoE mice and in table A.8, from db/db or diabetes mice are presented.

ID	PWV alg.	PWV N. D. Lascio
tm65_t0	1.0306	1.0306
tm66_t0	1.4386	1.4386
tm67_t0	1.0833	1.0833
tm68_t0	1.1702	1.1702
tm69_t0	1.2708	1.2708
tm70_t0	0.6499	0.6499
tm71_t0	1.1418	1.1418
tm72_t0	0.7483	0.7483
tm73_t0	1.1515	1.1515
tm74_t0	0.6540	-
tm75_t0	1.0422	-
tm76_t0	0.6350	0.6350
tm77_t0	1.2953	1.2953

Table A.5: *PWV values for wild type mice at 8 weeks of age.*

ID	PWV alg.	PWV N. D. Lascio
tm65_t2	0.6362	0.6362
tm66_t2	0.9418	1.0459
tm67_t2	1.1439	1.1439
tm68_t2	0.9227	0.9227
tm69_t2	1.3987	1.3987
tm70_t2	1.2353	1.2353
tm71_t2	0.9548	0.9548
tm72_t2	0.9998	0.9998
tm73_t2	0.8777	0.8777
tm74_t2	1.2625	-
tm75_t2	1.1083	-
tm76_t2	0.6231	0.6231
tm77_t2	1.5812	1.5812

Table A.6: *PWV values for wild type mice at 25 weeks of age.*

ID	PWV alg.	PWV N. D. Lascio
FF12	1.3695	1.4748
FF16	1.7022	1.7022
FF17	2.4110	2.411
FF18	1.3283	1.3727
FF24	1.9075	2.526
FF26	2.8478	2.8478
FF33	0.9142	1.1451
FF34	2.1690	2.1690
FF35	1.7305	1.7305
FF43	0.9437	1.1543

Table A.7: *PWV values for ApoE mice at 16 weeks of age.*

ID	PWV alg.	PWV N. D. Lascio
AS05	1.4732	1.4732
AS06	1.7005	1.5329
AS07	2.0134	2.0134
AS12	1.2176	1.2176
AS13	2.3146	2.3146
AS14	2.0372	2.0632
AS19	1.1500	1.1500
AS20	1.2863	1.2863
AS21	1.1938	1.1938

Table A.8: *PWV values for db/db mice at 13 weeks of age.*

For the ApoE mouse FF24, one can see that the PWV obtained with the implemented method differs from the value provided. This can be better observed in the Bland Altman plot used to validate this algorithm, in section 7.1.2. The first thought was that this was one of the

cases where the group of N. D. Lascio uses manual correction to choose the starting and ending points to calculate the slope of the lnD-V loop. However, one cannot get this value by manual correction. Automatic and manual PWV calculation is illustrated in figure A.4, where PWV has been calculate using automatic (A.4a) and correction (A.4b) PWV mode. The closest PWV value to the one from N. D. Lascio that one can get manually is 2.5187 (m/s).

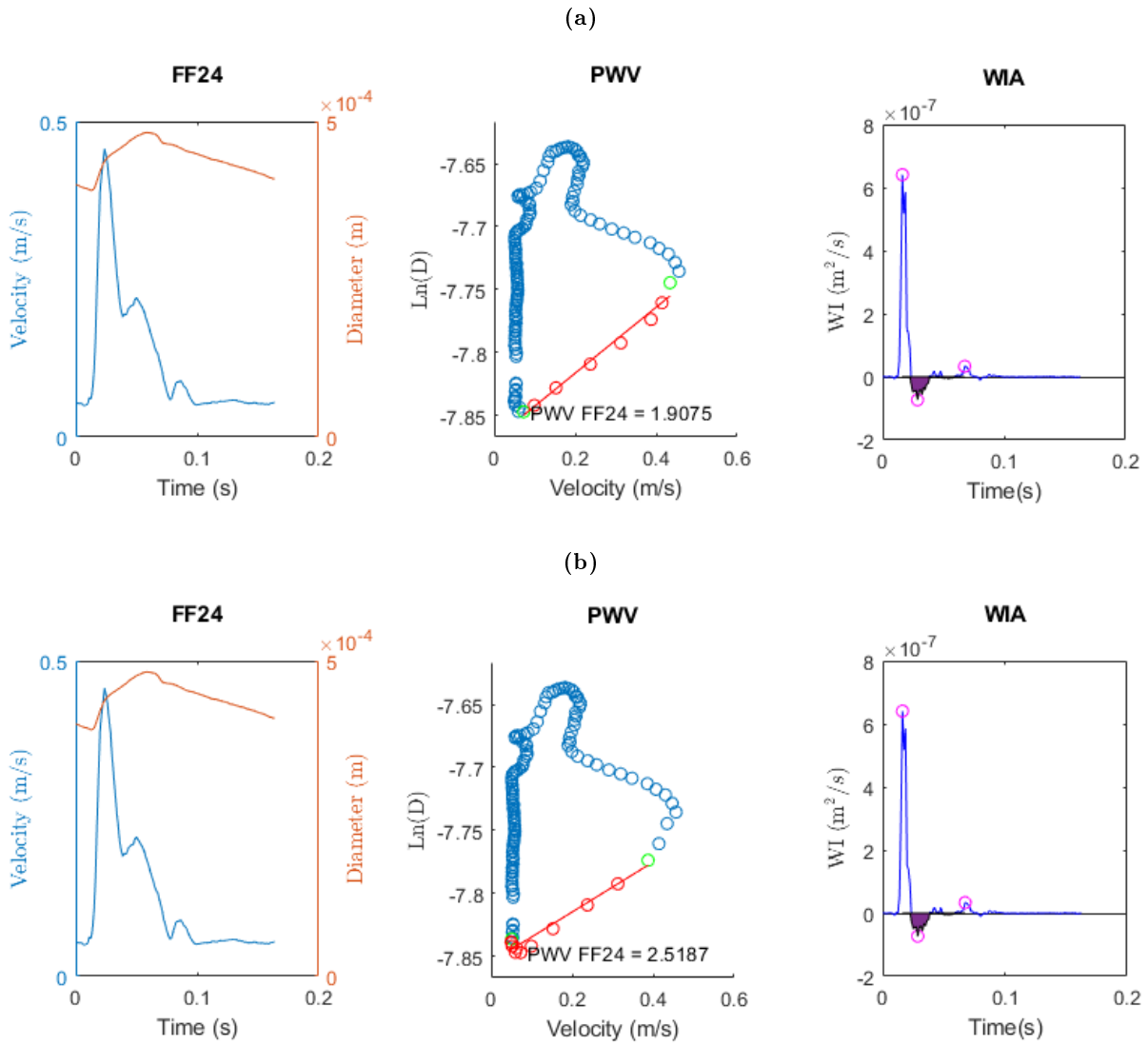

Figure A.4: *Pulse wave velocity calculation and wave intensity peaks detection for the ApoE mouse FF24 with the implemented algorithm for two different PWV modes: automatic (a) and correction (b).*

As one can see in figure A.4b, the starting point of the slope does not correspond to the begining of the linear phase of the loop. For this reason, it has not been corrected. Thus, the PWV value automatically calculated for mouse FF24 is used for calculating the rest of parameters from wave intensity analysis, later used in the TC2 comparison.

A.3 Augmentation Index

Tables A.9 and A.10 show AIx1 and AIx2 values for wild type young and old mice respectively. At the age of 8 weeks, AIx1 and AIx2 are the same for every mouse except for tm68 and tm77. At the age of 25 weeks, tm66, tm71 and tm77 also present a second notch. Exemplarily, one can see inflection points corresponding to both AIx values for mouse tm71 in figure A.5.

ID	AIx1	AIx2
tm65_t0	0.11026	0.11026
tm66_t0	0.10836	0.10836
tm67_t0	0.19181	0.19181
tm68_t0	0.21523	0.23244
tm69_t0	0.23898	0.23897
tm70_t0	0.18821	0.18821
tm71_t0	0.21704	0.21704
tm72_t0	0.28678	0.28678
tm73_t0	0.24425	0.24425
tm74_t0	0.21316	0.21316
tm75_t0	0.11661	0.11661
tm76_t0	0.14199	0.14199
tm77_t0	0.10061	0.11178

Table A.9: *Augmentation index values for wild type mice at 8 weeks of age.*

ID	AIx1	AIx2
tm65_t2	0.25479	0.25479
tm66_t2	0.26612	0.26612
tm67_t2	0.33548	0.35873
tm68_t2	0.32827	0.32827
tm69_t2	0.08807	0.08807
tm70_t2	0.24448	0.34809
tm71_t2	0.18256	0.32676
tm72_t2	0.31632	0.31632
tm73_t2	0.27690	0.27690
tm74_t2	0.31263	0.31263
tm75_t2	0.20458	0.20458
tm76_t2	0.32674	0.32674
tm77_t2	0.16665	0.16665

Table A.10: *Augmentation index values for wild type mice at 25 weeks of age.*

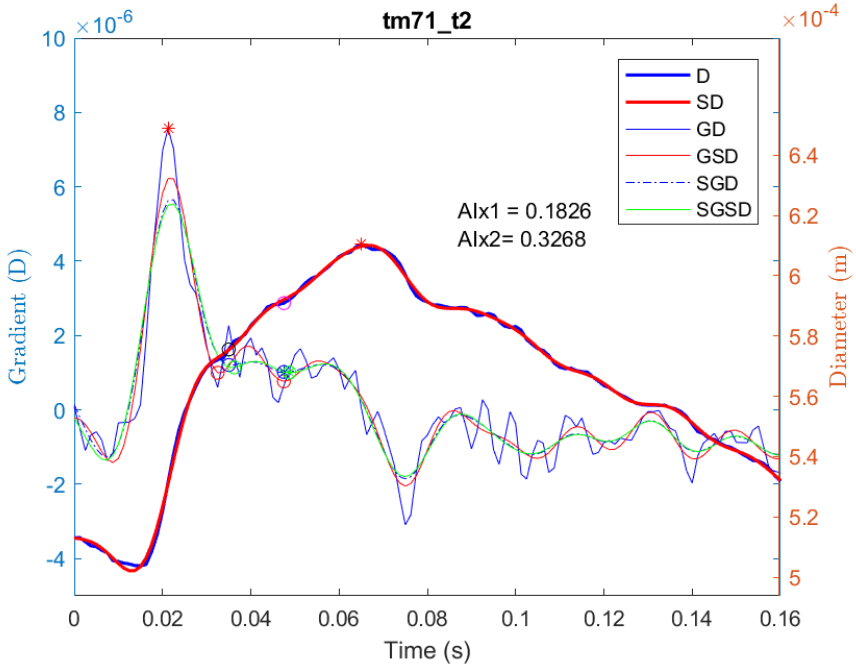

Figure A.5: *Augmentation index algorithm output figure for the wild type mouse tm71, 25 weeks old.*

Table A.11 and table A.12 contain AIx values for ApoE and diabetes mice, respectively.

ID	AIx1	AIx2
FF12	0.23029	0.23029
FF16	0.20683	0.20683
FF17	0.14546	0.14546
FF18	0.23335	0.23335
FF24	0.33385	0.33385
FF26	0.06225	0.21285
FF33	0.19607	0.19607
FF34	0.29403	0.29403
FF35	0.13782	0.13782
FF43	0.09238	0.09238

Table A.11: *Augmentation index values for ApoE mice at 16 weeks of age*

ID	AIx1	AIx2
AS05	0.31561	0.31561
AS06	0.36573	0.36573
AS07	0.43010	0.43010
AS12	0.34551	0.35608
AS13	0.43096	0.43096
AS14	0.25103	0.25103
AS19	0.21051	0.21051
AS20	0.33554	0.33554
AS21	0.27090	0.27090

Table A.12: *Augmentation index values for db/db mice at 13 weeks of age.*

APPENDIX B

Multiple Data Comparison

All cardiovascular parameters calculated for the four groups of mice are presented in table B.1.

Variables	WT_t0	WT_t2	ApoE	db_db
n	13	13	10	9
Age (weeks)	8	25	16	13
HR (bpm)	379 [346 405]	340 [324 369]	380 [357 471]	328 [285 335]
RR (bpm)	131 [111 156]	117 [95.8 133]	159 [141 172]	152 [139 166]
T (ºC)	35.5 [35.1 35.6]	34.8 [33.8 35.1]	35.7 [35.3 35.8]	34.2 [33.9 35]
qt (s)	0.0237 [0.0226 0.0273]	0.0291 [0.0272 0.0315]	0.0229 [0.0218 0.0245]	0.0284 [0.0268 0.0295]
qtc (s)	54.9 [50.4 61.1]	58.5 [56.4 63.4]	52.2 [50.1 54.5]	57.7 [53.8 60.2]
pq (s)	0.0404 [0.0347 0.0442]	0.0417 [0.0309 0.0453]	0.0413 [0.0347 0.0448]	0.0401 [0.0338 0.0447]
qrs (s)	0.0101 [0.0091 0.0112]	0.0113 [0.0108 0.0147]	0.00965 [0.00909 0.0112]	0.0113 [0.00962 0.0121]
rr (s)	0.162 [0.157 0.174]	0.18 [0.173 0.188]	0.166 [0.127 0.17]	0.183 [0.179 0.209]
Dm (mm)	0.463 [0.449 0.475]	0.472 [0.449 0.513]	0.42 [0.413 0.441]	0.428 [0.4 0.469]
Ds (mm)	0.516 [0.502 0.524]	0.511 [0.494 0.559]	0.461 [0.449 0.482]	0.476 [0.437 0.513]
Dd (mm)	0.394 [0.374 0.422]	0.428 [0.408 0.46]	0.38 [0.375 0.387]	0.384 [0.366 0.433]
reID (%)	25.2 [24 32.9]	21.1 [18.9 23.7]	23.5 [20.7 25.7]	18.6 [16.7 21.4]
Vp (cm/s)	21.3 [19 29.8]	19.5 [18.1 24]	36.7 [28 42.5]	16.7 [15.5 20]
Aix (%)	0.192 [0.115 0.223]	0.266 [0.199 0.319]	0.201 [0.138 0.233]	0.336 [0.266 0.382]
PWV (m/s)	1.08 [0.725 1.2]	1 [0.911 1.24]	1.72 [1.33 2.17]	1.47 [1.21 2.02]
W1 (m^2/s)	4.67e-07 [2.57e-07 7.09e-07]	2.57e-07 [1.74e-07 3.1e-07]	4.77e-07 [2.49e-07 5.52e-07]	1.57e-07 [1.26e-07 2.46e-07]
W2 (m^2/s)	2.58e-08 [1.77e-08 3.46e-08]	2.51e-08 [1.32e-08 3e-08]	3.89e-08 [3.34e-08 5.72e-08]	1.65e-08 [1.15e-08 2.58e-08]
Wb (m^2/s)	-7.71e-08 [-1.32e-07 -5.9e-08]	-5.29e-08 [-6.2e-08 -2.82e-08]	-7.81e-08 [-9.82e-08 -6.95e-08]	-2.67e-08 [-4.2e-08 -2.4e-08]
NA (m^2)	4.62e-10 [3.6e-10 7.56e-10]	2.78e-10 [2.12e-10 3.96e-10]	5.92e-10 [3.73e-10 6.66e-10]	2.36e-10 [1.97e-10 3e-10]
RI (%)	0.172 [0.126 0.319]	0.199 [0.148 0.237]	0.185 [0.152 0.221]	0.17 [0.157 0.277]

Table B.1: *Results of all groups of mice.*

Bibliography

[1] G. A. Roth, M. D. Huffman, A. E. Moran, et al., "Global and Regional Patterns in Cardiovascular Mortality From 1990 to 2013", *Circulation* **2015**, *132*, 1667–1678.

[2] C. Palombo, M. Kozakova, "Arterial stiffness, atherosclerosis and cardiovascular risk: Pathophysiologic mechanisms and emerging clinical indications", *Vascular Pharmacology* **2016**, *77*, 1 –7.

[3] D. K. Arnett, G. W. Evans, W. A. Riley, "Arterial Stiffness: A New Cardiovascular Risk Factor?", *American Journal of Epidemiology* **1994**, *140*, 669–682.

[4] C. J. Hartley, A. K. Reddy, S. Madala, et al., "Doppler velocity measurements from large and small arteries of mice", *American Journal of Physiology - Heart and Circulatory Physiology* **2011**, *301*, H269–H278.

[5] W. W. Nichols, M. F. O'Rourke, C. Hartley, et al., *McDonald's blood flow in arteries: theoretical, experimental, and clinical principles.* 4th ed., Arnold; Oxford University Press London: New York, **1998**.

[6] N. Di Lascio, C. Kusmic, F. Stea, et al., "Wave intensity analysis in mice: age-related changes in WIA peaks and correlation with cardiac indexes", *Heart and Vessels* **2017**, *32*, 474–483.

[7] K. H. Parker, C. J. H. Jones, "Forward and Backward Running Waves in the Arteries: Analysis Using the Method of Characteristics", *Journal of Biomechanical Engineering* **1990**, *112*, 322–326.

[8] E. Kaniusas, *Biomedical Signals and Sensors I: Linking Physiological Phenomena and Biosignals*, Springer Berlin Heidelberg, **2012**.

[9] C. Magg, *Development and Evaluation of a Murine ECG Annotation Algorithm*, Vienna, **2018**.

[10] S. Webb, N. Brown, R. H. Anderson, "The structure of the mouse heart in late fetal stages", **1996**, *194*, 37–47.

[11] A. Krishnan, R. Samtani, P. Dhanantwari, et al., "A Detailed Comparison of Mouse and Human Cardiac Development", *Pediatric research* **2014**, *76*, 500–507.

[12] Draw and label diagram of mammalian heart, Heart Anatomy, Science, Online; accessed 21 Aug 2018, **2018**, http://anatomyhumancharts.com/draw-and-label-diagram-of-mammalian-heart/draw-and-label-diagram-of-mammalian-heart-mouse-eye-anatomy-gallery-human-learni-image-organs-on-free-mouse/.

[13] M. Cook, *The anatomy of the laboratory mouse*, Academic Press, **1965**, http://www.informatics.jax.org/cookbook/figures/figure91.shtml.

[14] A. Wessels, D. Sedmera, "Developmental anatomy of the heart: a tale of mice and man", *Physiological genomics* **2003**, *15*, 165–176.

[15] P. A. Doevendans, M. J. Daemen, E. D. de Muinck, et al., "Cardiovascular phenotyping in mice", *Cardiovascular Research* **1998**, *39*, 34–49.

[16] C. G. Caro, T. J. Pedley, R. C. Schroter, et al., *The Mechanics of the Circulation*, Cambridge University Press, Cambridge, **2011**.

[17] D. A. McDonald, *Blood flow in arteries*, 2nd ed., Edward Arnold London, **1974**.

[18] Human abdominal arterial and venous tree tiagram. Major arteries in the human body. Online; accessed 29 March 2018, **2017**, https://humananatomyly.com/human-abdominal-arterial-and-venous-tree-diagram/human-abdominal-arterial-and-venous-tree-diagram-this-diagrams-shows-the-major-arteries-in-the-human-body-school.

[19] Mouse brain vessel anatomy, Online; accessed 29 March 2018, **2016**, http://geoface.info/aecd/e5578c708086/serotonin-and-blood-pressure-regul-025999.

[20] A. Feintuch, P. Ruengsakulrach, A. Lin, et al., "Hemodynamics in the mouse aortic arch as assessed by MRI, ultrasound, and numerical modeling", *American Journal of Physiology-Heart and Circulatory Physiology* **2007**, *292*, H884–H892.

[21] C. Casteleyn, B. Trachet, D. Van Loo, et al., "Validation of the murine aortic arch as a model to study human vascular diseases", *Journal of Anatomy* **2010**, *216*, 563–571.

[22] Advanced cardiovascular chysiology and hemodynamics, Online; accessed 27 February 2018, **2010**, http://www.dynapulse.com/educator/webcurriculum/Chapter%203/Chapter%203%20Hemodynamics.htm.

[23] M. Masuda, T. Emoto, A. Suzuki, et al., "Evaluation of blood flow velocity waveform in common carotid artery using multi-branched arterial segment model of human arteries", *Biomedical Signal Processing and Control* **2013**, *8*, 509 –519.

[24] L. Klabunde, A. Tajik, R. Wilkins, et al., *Cardiovascular Physiology Concepts 2nd Ed. + the Echo Manual, 3rd Ed.* 2nd edition, Lippincott Williams & Wilkins, Philadelphia, United States, **2013**.

[25] C. J. Hartley, A. K. Reddy, S. Madala, et al., "Hemodynamic changes in apolipoprotein E-knockout mice", *American Journal of Physiology-Heart and Circulatory Physiology* **2000**, *279*, H2326–H2334.

[26] L. C. Lotteraner, *Modeling aortic blood pressure with difference equations*, Vienna, **2018**.

[27] Pulse wave velocity, Online; accessed 03 April 2018, **2018**, `https://www.datasci.com/solutions/cardiovascular/pulse-wave-velocity-(pwv)`.

[28] What is blood pulse wave, Online; accessed 05 February 2018, **2018**, `https://biovotion.zendesk.com/hc/en-us/articles/213581765-What-is-Blood-Pulse-Wave-`.

[29] C. Borghi, M. C. Acelajado, Y. Gupta, et al., "Role of nebivolol in the control and management of central aortic blood pressure in hypertensive patients", *Journal Of Human Hypertension* **2017**, *31*, 605.

[30] J. Steppan, V. Barodka, D. E. Berkowitz, et al., "Vascular stiffness and increased pulse pressure in the aging cardiovascular system", *Cardiology research and practice* **2011**.

[31] I. Ikonomidis, G. Makavos, J. Lekakis, "Arterial stiffness and coronary artery disease", *Current Opinion in Cardiology* **2015**, *30*.

[32] C. Trivedy, M. Hall, H. Ellis, *Basic Sciences for MCEM*, Hodder Arnold, **2016**.

[33] A. Benetos, S. Laurent, A. P. Hoeks, et al., "Arterial alterations with aging and high blood pressure. A noninvasive study of carotid and femoral arteries.", *Arteriosclerosis Thrombosis and Vascular Biology* **1993**, *13*, 90–97.

[34] V. Herold, M. Parczyk, P. Mörchel, et al., "In vivo measurement of local aortic pulse-wave velocity in mice with MR microscopy at 17.6 tesla", *Magnetic Resonance in Medicine* **2009**, *61*, 1293–1299.

[35] X. Li, P. Lyu, Y. Ren, et al., "Arterial stiffness and cognitive impairment", *Journal of the Neurological Sciences* **2017**, *380*, 1 –10.

[36] T. T. van Sloten, G. F. Mitchell, S. Sigurdsson, et al., "Associations between arterial stiffness, depressive symptoms and cerebral small vessel disease: cross-sectional findings from the AGES-Reykjavik Study", *Journal of Psychiatry & Neuroscience* **2015**, *41*, 162–168.

[37] M. P. Pase, A. Pipingas, M. Kras, et al., "Healthy middle-aged individuals are vulnerable to cognitive deficits as a result of increased arterial stiffness", *Journal of Hypertension* **2010**, *28*.

[38] N. Saji, K. Toba, T. Sakurai, "Cerebral Small Vessel Disease and Arterial Stiffness: Tsunami Effect in the Brain?", *Pulse* **2016**, *3*, 182–189.

[39] A. E. Roher, C. Esh, T. A. Kokjohn, et al., "Circle of Willis Atherosclerosis Is a Risk Factor for Sporadic Alzheimer's Disease", *Arteriosclerosis Thrombosis and Vascular Biology* **2003**, *23*, 2055–2062.

[40] A. Serrano-Pozo, M. P. Frosch, E. Masliah, et al., "Neuropathological Alterations in Alzheimer Disease", *Cold Spring Harbor Perspectives in Medicine:* **2011**, *1*, a006189.

[41] S. E. Whitesall, J. B. Hoff, A. P. Vollmer, et al., "Comparison of simultaneous measurement of mouse systolic arterial blood pressure by radiotelemetry and tail-cuff methods", *American Journal of Physiology-Heart and Circulatory Physiology* **2004**, *286*, H2408–H2415.

[42] B. D. Hoit, R. A. Walsh, *Cardiovascular Physiology in the Genetically Engineered Mouse*, Springer US, **2002**.

[43] Anatomy and physiology II; Module 4: The cardiovascular system: blood vessels and circulation, Online; accessed 05 February 2018, **2018**, `https://courses.lumenlearning.com/suny-ap2/chapter/blood-flow-blood-pressure-and-resistance-no-content/`.

[44] F. N. Van de Vosse, N. Stergiopulos, "Pulse wave propagation in the arterial tree", *Annual Review of Fluid Mechanics* **2011**, *43*, 467–499.

[45] L. R. Hellevik, Cardiovascular biomechanics, Pressure and flow in the cardiovascular system, Online; accessed 21 August 2018, **2015**, `http://folk.ntnu.no/leifh/teaching/tkt4150/._main025.html`.

[46] W. H. Barry, "Heart Physiology From Cell to Circulation, 4th ed.", *Circulation* **2004**, *110*, e313–e313.

[47] Peripheral resistance, Online; accessed 03 April 2018, **2012**, `http://pie.med.utoronto.ca/CA/CA_content/CA_cardiacPhys_peripheralResistance.html`.

[48] S. J. Marchais, A. P. Guerin, B. Pannier, et al., "Arterial Compliance and Blood Pressure", *Drugs* **1993**, *46*, 82–87.

[49] L. J. S. da Fonseca, M. A. Mota-Gomes, L. A. Rabelo, "Radial applanation tonometry as an adjuvant tool in the noninvasive arterial stiffness and blood pressure assessment", *World Journal of Cardiovascular Diseases* **2014**, *04*, 11.

[50] R. Asmar, A. Rudnichi, J. Blacher, et al., "Pulse pressure and aortic pulse wave are markers of cardiovascular risk in hypertensive populations*", *American Journal of Hypertension* **2001**, *14*, 91–97.

[51] The Reference Values for Arterial Stiffness' Collaboration, "Determinants of pulse wave velocity in healthy people and in the presence of cardiovascular risk factors: 'establishing normal and reference values'", *European heart journal* **2010**, *31*, 2338–2350.

[52] A. K. Reddy, G. E. Taffet, S. Madala, et al., "Noninvasive blood pressure measurement in mice using pulsed Doppler ultrasound", *Ultrasound in Medicine & Biology* **2003**, *29*, 379 –385.

[53] Y.-X. Wang, "Cardiovascular functional phenotypes and pharmacological responses in apolipoprotein E deficient mice", *Neurobiology of Aging* **2005**, *26*, 309–316.

[54] I. Tan, M. Butlin, Y. Y. Liu, et al., "Heart Rate Dependence of Aortic Pulse Wave Velocity at Different Arterial Pressures in Rats Novelty and Significance", *Hypertension* **2012**, *60*, 528–533.

[55] H. Xiao, I. Tan, M. Butlin, et al., "Arterial viscoelasticity: role in the dependency of pulse wave velocity on heart rate in conduit arteries", *American Journal of Physiology-Heart and Circulatory Physiology* **2017**, *312*, H1185–H1194.

[56] D. Fatkin, R. P. Kelly, M. P. Feneley, "Relations between left atrial appendage blood flow velocity, spontaneous echocardiographic contrast and thromboembolic risk in vivo", *Journal of the American College of Cardiology* **1994**, *23*, 961–969.

[57] D. J. Farrar, H. D. Green, M. G. Bond, et al., "Aortic pulse wave velocity, elasticity, and composition in a nonhuman primate model of atherosclerosis.", *Circulation Research* **1978**, *43*, 52–62.

[58] T. W. Latson, W. C. Hunter, N Katoh, et al., "Effect of nitroglycerin on aortic impedance, diameter, and pulse-wave velocity.", *Circulation Research* **1988**, *62*, 884–890.

[59] J. Alastruey, A. A. E. Hunt, P. D. Weinberg, "Novel wave intensity analysis of arterial pulse wave propagation accounting for peripheral reflections", *International Journal for Numerical Methods in Biomedical Engineering* **2013**, *30*, 249–279.

[60] R. M. Fitch, R. Vergona, M. E. Sullivan, et al., "Nitric oxide synthase inhibition increases aortic stiffness measured by pulse wave velocity in rats", *Cardiovascular Research* **2001**, *51*, 351–358.

[61] Y.-H. Sun, T. J. Anderson, K. H. Parker, et al., "Wave-intensity analysis: a new approach to coronary hemodynamics", *Journal of Applied Physiology* **2000**, *89*, 1636–1644.

[62] A. Zambanini, S. L. Cunningham, K. H. Parker, et al., "Wave-energy patterns in carotid, brachial, and radial arteries: a noninvasive approach using wave-intensity analysis", *American Journal of Physiology-Heart and Circulatory Physiology* **2005**, *289*, H270–H276.

[63] N. D. Lascio, F. Stea, C. Kusmic, et al., "Non-invasive assessment of pulse wave velocity in mice by means of ultrasound images", *Atherosclerosis* **2014**, *237*, 31 –37.

[64] B. J. Boukens, M. R. Rivaud, S. Rentschler, et al., "Misinterpretation of the mouse ECG: 'musing the waves of Mus musculus'", *The Journal of Physiology* **2014**, *592*, 4613–4626.

[65] P. J. Danneman, M. A. Suckow, C. Brayton, *The Laboratory Mouse, Second Edition*, CRC Press, **2012**.

[66] A. J. Leloup, P. Fransen, C. E. Van Hove, et al., "Applanation Tonometry in MiceNovelty and Significance", *Hypertension* **2014**, *64*, 195–200.

[67] T. M. Donnelly, "The BSAVA Manual of Exotic Pets (4th edn.)", **2003**, *32*, 29–30.

[68] Pulse (Heart Rate), PubMed Health Glossary, Online; accessed 17 May 2018, `https://www.ncbi.nlm.nih.gov/pubmedhealth/PMHT0024325/`.

[69] U. R. Acharya, P. Joseph, N Kannathal, et al., "Heart rate variability: A review", *Medical & Biological Engineering & Computing* **2007**, *44*, 1031–51.

[70] A. Rawshani, Clinical ECG interpretation, From physiology to clinical management, Online; accessed 15 May 2018, https://ecgwaves.com/ecg-normal-p-wave-qrs-complex-st-segment-t-wave-j-point/.

[71] I. Mozos, A. Caraba, "Electrocardiographic Predictors of Cardiovascular Mortality", *Disease markers* **2015**.

[72] T. Speerschneider, M. B. Thomsen, "Physiology and analysis of the electrocardiographic T wave in mice", *Acta Physiologica* **2013**, *209*, 262–271.

[73] S. Kaese, S. Verheule, "Cardiac electrophysiology in mice: a matter of size", *Frontiers in Physiology* **2012**, *3*, 345.

[74] A. Atkielski Agateller, Schematic diagram of normal sinus rhythm for a human heart as seen on ECG, Wikimedia, Online; accessed 15 May 2018, https://commons.wikimedia.org/w/index.php?curid=1560893.

[75] D. Durrer, R. T. Van Dam, G. E. Freud, et al., "Total Excitation of the Isolated Human Heart", *Circulation* **1970**, *41*, 899–912.

[76] G. Liu, J. B. Iden, K. Kovithavongs, et al., "In vivo temporal and spatial distribution of depolarization and repolarization and the illusive murine T wave", *The Journal of Physiology* **2003**, *555*, 267–279.

[77] A. N. Goldbarg, H. K. Hellerstein, J. H. Bruell, et al., "Electrocardiogram of the normal mouse, Mus musculus: general considerations and genetic aspects", *Cardiovascular research* **1968**, *2*, 93–99.

[78] S. Danik, C. Cabo, C. Chiello, et al., "Correlation of repolarization of ventricular monophasic action potential with ECG in the murine heart", *American Journal of Physiology-Heart and Circulatory Physiology* **2002**, *283*, 372–381.

[79] H. Bazett, "An Analysis of the Time-Relations of Electrocardiograms.", *Heart* **1920**, *7*, 353–370.

[80] G. F. Mitchell, A. Jeron, G. Koren, "Measurement of heart rate and QT interval in the conscious mouse", *American Journal of Physiology-Heart and Circulatory Physiology* **1998**, *274*, H747–H751.

[81] A. Doyle, M. P. McGarry, N. A. Lee, et al., "The Construction of Transgenic and Gene Knockout/Knockin Mouse Models of Human Disease", *Transgenic research* **2011**, *21*, 327–349.

[82] Y.-X. Wang, H.-M. Meredith, V. Ro, et al., "Increased aortic stiffness assessed by pulse wave velocity in apolipoprotein E-deficient mice", *American Journal of Physiology-Heart and Circulatory Physiology* **2000**, *278*, H428–H434.

[83] M. Parczyk, V. Herold, G. Klug, et al., "Regional in vivo transit time measurements of aortic pulse wave velocity in mice with high-field CMR at 17.6 Tesla", *Journal of Cardiovascular Magnetic Resonance* **2010**, *12*, 72–72.

[84] Mouse strain datasheet, Online; accessed 04 April 2018, **2018**, https://www.jax.org/strain/003548.

[85] X.-F. Leong, C.-Y. Ng, K. Jaarin, Animal Models in Cardiovascular Research: Hypertension and Atherosclerosis, **2015**, http://dx.doi.org/10.1155/2015/528757.

[86] G. L. Sasso, W. K. Schlage, S. Boué, et al., "The Apoe-/- mouse model: a suitable model to study cardiovascular and respiratory diseases in the context of cigarette smoke exposure and harm reduction", *Journal of translational medicine* **2016**, *14*.

[87] A. Rigotti, H. E. Miettinen, M. Krieger, "The role of the high-density lipoprotein receptor SR-BI in the lipid metabolism of endocrine and other tissues", *Endocrine reviews* **2003**, *24*, 357–387.

[88] A. Braun, B. L. Trigatti, M. J. Post, et al., "Loss of SR-BI Expression Leads to the Early Onset of Occlusive Atherosclerotic Coronary Artery Disease, Spontaneous Myocardial Infarctions, Severe Cardiac Dysfunction, and Premature Death in Apolipoprotein E–Deficient Mice", *Circulation Research* **2002**, *90*, 270–276.

[89] J. E. Wagenseil, R. P. Mecham, "Elastin in large artery stiffness and hypertension", *Journal of Cardiovascular Translational Research* **2012**, *5*, 264–273.

[90] L. A. Schildmeyer, R. Braun, G. Taffet, et al., "Impaired vascular contractility and blood pressure homeostasis in the smooth muscle α-actin null mouse", *The FASEB Journal* **2000**, *14*, 2213–2220.

[91] C. J. Hartley, G. E. Taffet, A. K. Reddy, et al., "Noninvasive Cardiovascular Phenotyping in Mice", *ILAR Journal* **2002**, *43*, 147–158.

[92] P. Lacolley, P. Challande, S. Boumaza, et al., "Mechanical properties and structure of carotid arteries in mice lacking desmin", *Cardiovascular Research* **2001**, *51*, 178–187.

[93] S. Ishibashi, M. S. Brown, J. L. Goldstein, et al., "Hypercholesterolemia in low density lipoprotein receptor knockout mice and its reversal by adenovirus-mediated gene delivery.", *Journal of Clinical Investigation* **1993**, *92*, 883–893.

[94] J. W. Knowles, N. Maeda, "Genetic Modifiers of Atherosclerosis in Mice", *Arteriosclerosis Thrombosis and Vascular Biology* **2000**, *20*, 2336–2345.

[95] G. Luo, P. Ducy, M. D. McKee, et al., "Spontaneous calcification of arteries and cartilage in mice lacking matrix GLA protein", *Nature* **1997**, *386*, 78–81.

[96] B. L. Lima, E. J. C. Santos, G. R. Fernandes, et al., "A New Mouse Model for Marfan Syndrome Presents Phenotypic Variability Associated with the Genetic Background and Overall Levels of Fbn1 Expression", *PLOS ONE* **2010**, *5*, 1–9.

[97] L. Lee, J. Z. Cui, M. Cua, et al., "Aortic and Cardiac Structure and Function Using High-Resolution Echocardiography and Optical Coherence Tomography in a Mouse Model of Marfan Syndrome", *PLOS ONE* **2016**, *11*, e0164778.

[98] K. Kazama, G. Wang, K. Frys, et al., "Angiotensin II attenuates functional hyperemia in the mouse somatosensory cortex", *American Journal of Physiology-Heart and Circulatory Physiology* **2003**, *285*, H1890–H1899.

[99] M. Wiesmann, M. Roelofs, R. van der Lugt, et al., "Angiotensin II, hypertension and angiotensin II receptor antagonism: Roles in the behavioural and brain pathology of a mouse model of Alzheimer's disease", *J Cereb Blood Flow Metab* **2016**, *37*, 2396–2413.

[100] B. A. Couch, M. E. Kerrisk, A. C. Kaufman, et al., "Delayed amyloid plaque deposition and behavioral deficits in outcrossed AβPP/PS1 mice", *Journal of Comparative Neurology* **2013**, *521*, 1395–1408.

[101] D. Cifuentes, M. Poittevin, E. Dere, et al., "Hypertension Accelerates the Progression of Alzheimer-Like Pathology in a Mouse Model of the DiseaseNovelty and Significance", *Hypertension* **2015**, *65*, 218–224.

[102] P. Bogdanov, L. Corraliza, J. A. Villena, et al., "The db/db Mouse: A Useful Model for the Study of Diabetic Retinal Neurodegeneration", *PLOS ONE* **2014**, *9*, 1–18.

[103] M. J. Orland, M. A. Permutt, "Quantitative Analysis of Pancreatic Proinsulin mRNA in Genetically Diabetic (db/db) Mice", *Diabetes* **1987**, *36*, 341–347.

[104] J. E. Wagenseil, C. H. Ciliberto, R. H. Knutsen, et al., "Reduced Vessel Elasticity Alters Cardiovascular Structure and Function in Newborn Mice", *Circulation research* **2009**, *104*, 1217–1224.

[105] A. J. A. Leloup, C. E. Van Hove, A. Kurdi, et al., "A novel set-up for the ex vivo analysis of mechanical properties of mouse aortic segments stretched at physiological pressure and frequency", *The Journal of Physiology* **2016**, *594*, 6105–6115.

[106] J. C. Kohn, A. Chen, S. Cheng, et al., "Mechanical heterogeneities in the subendothelial matrix develop with age and decrease with exercise", *Journal of biomechanics* **2016**, *49*, 1447–1453.

[107] S. Vulliémoz, N. Stergiopulos, R. Meuli, "Estimation of local aortic elastic properties with MRI", *Magnetic Resonance in Medicine* **2002**, *47*, 649–654.

[108] G. F. Mitchell, M. A. Pfeffer, P. V. Finn, et al., "Comparison of techniques for measuring pulse-wave velocity in the rat", *Journal of Applied Physiology* **1997**, *82*, 203–210.

[109] J. Fox, S. Barthold, M. Davisson, et al., *The Mouse in Biomedical Research: Normative Biology, Husbandry, and Models*, Elsevier Science, **2006**.

[110] A. Reddy, C. Hartley, T. Pham, et al., *Young Little Mice Express a Premature Cardiovascular Aging Phenotype*, *Vol. 69*, **2013**.

[111] J. Malkoff, "Non-invasive blood pressure for mice and rats", *Animal Lab News Kent Scientific Corporation* **2005**, 1–12.

[112] Y. Wang, Zhen ans Yang, L.-j. Yuan, J. Liu, et al., "Noninvasive Method for Measuring Local Pulse Wave Velocity by Dual Pulse Wave Doppler: In Vitro and In Vivo Studies", *PLOS ONE* **2015**, *10*, 1–13.

[113] Magnetic resonance imaging (MRI), National Institute of Biomedical Imaging and Bioengineering (NIBIB), Online; accessed 09 April 2018, `https://www.nibib.nih.gov/science-education/science-topics/magnetic-resonance-imaging-mri`.

[114] C. J. Hartley, H. G. Hanley, R. M. Lewis, et al., "Synchronized pulsed Doppler blood flow and ultrasonic dimension measurement in conscious dogs", *Ultrasound in Medicine & Biology* **1978**, *4*, 99–110.

[115] H. Miyashita, "Clinical Assessment of Central Blood Pressure", *Current Hypertension Reviews* **2012**, *8*, 80–90.

[116] B. A. Haluska, L. Jeffriess, P. M. Mottram, et al., "A new technique for assessing arterial pressure wave forms and central pressure with tissue Doppler", *Cardiovascular Ultrasound* **2007**, *5*, 6.

[117] Z. Chen, T. E. Milner, S. Srinivas, et al., "Noninvasive imaging of in vivo blood flow velocity using optical Doppler tomography", *Opt. Lett.* **1997**, *22*, 1119–1121.

[118] J. C. Bramwell, A. V. Hill, "Velocity of transmission of the pulse-wave", *The Lancet*, *199*, 891–892.

[119] C. J. Hartley, G. E. Taffet, L. H. Michael, et al., "Noninvasive determination of pulse-wave velocity in mice", *American Journal of Physiology-Heart and Circulatory Physiology* **1997**, *273*, H494–H500.

[120] S. I. Rabben, N. Stergiopulos, L. R. Hellevik, et al., "An ultrasound-based method for determining pulse wave velocity in superficial arteries", *Journal of Biomechanics*, *37*, 1615–1622.

[121] A. Gotschy, W. R. Bauer, P. Winter, et al., "Local versus global aortic pulse wave velocity in early atherosclerosis: An animal study in ApoE-/-mice using ultrahigh field MRI", *PLOS ONE* **2017**, *12*, 1–14.

[122] Y. Li, A. W. Khir, "Determination of wave speed and distensibility of flexible tubes using diameter and velocity", **2009**, 1796–1799.

[123] V. Herold, S. Herz, P. Winter, et al., "Assessment of local pulse wave velocity distribution in mice using k-t BLAST PC-CMR with semi-automatic area segmentation", *Journal of Cardiovascular Magnetic Resonance* **2017**, *19*, 77.

[124] T. Hirai, S. Sasayama, T. Kawasaki, et al., "Stiffness of systemic arteries in patients with myocardial infarction. A noninvasive method to predict severity of coronary atherosclerosis.", **1989**, *80*, 78–86.

[125] J. E. Barbato, E. Tzeng, "Nitric oxide and arterial disease", *Journal of Vascular Surgery* **2004**, *40*, 187 –193.

[126] A. K. Reddy, Y.-H. Li, T. T. Pham, et al., "Measurement of aortic input impedance in mice: effects of age on aortic stiffness", *American Journal of Physiology-Heart and Circulatory Physiology* **2003**, *285*, H1464–H1470.

[127] A. K. Reddy, Y.-H. Li, T. T. Pham, et al., *Indices of aortic stiffness in mice*, *Vol. 1*, **2003**, pp. 276–278.

[128] C. Iadecola, F. Zhang, K. Niwa, et al., "SOD1 rescues cerebral endothelial dysfunction in mice overexpressing amyloid precursor protein", *Nature Neuroscience* **1999**, *2*, 157–161.

[129] P. B. Gorelick, A. Scuteri, S. E. Black, et al., "Vascular contributions to cognitive impairment and dementia: a statement for healthcare professionals from the american heart association/american stroke association.", *Stroke* **2011**, *42 9*, 2672–713.

[130] P. W. Pires, C. M. Dams Ramos, N. Matin, et al., "The effects of hypertension on the cerebral circulation", *American Journal of Physiology - Heart and Circulatory Physiology* **2013**, *304*, H1598–H1614.

[131] K. Matsushita, Y. Kuriyama, K. Nagatsuka, et al., "Periventricular white matter lucency and cerebral blood flow autoregulation in hypertensive patients.", *Hypertension* **1994**, *23*, 565–568.

[132] H. Ito, I. Kanno, M. Ibaraki, et al., "Changes in human cerebral blood flow and cerebral blood volume during hypercapnia and hypocapnia measured by positron emission tomography", *Journal of Cerebral Blood Flow & Metabolism* **2003**, *23*, 665–670.

[133] C. J. Hartley, A. K. Reddy, S. Madala, et al., "Noninvasive ultrasonic measurement of arterial wall motion in mice", **2004**, *2*, 3688–3691.

[134] H. Jick, G. Zornberg, S. S. Jick, et al., "Statins and the Risk of Dementia", *Obstetric and Gynecologic Survey* **2000**, *56*.

[135] A. K. Reddy, G. E. Taffet, Y.-H. Li, et al., "Pulsed Doppler signal processing for use in mice: applications", *IEEE Transactions on Biomedical Engineering* **Oct. 2005**, *52*, 1771–1783.

[136] G. S. Ajith Kumar, B. Raj, S. Santhosh Kumar, et al., "Ascending Aortic Constriction in Rats for Creation of Pressure Overload Cardiac Hypertrophy Model", *Journal of Visualized Experiments* **2014**, 50983.

[137] K. Niki, M. Sugawara, D. Chang, et al., "A new noninvasive measurement system for wave intensity: evaluation of carotid arterial wave intensity and reproducibility", *Heart and Vessels* **2002**, *17*, 12–21.

[138] A. Harada, T. Okada, K. Niki, et al., "On-line noninvasive one-point measurements of pulse wave velocity", *Heart and Vessels* **2002**, *17*, 61–68.

[139] R. M. Weisbrod, T. Shiang, L. A. Sayah, et al., "Arterial Stiffening Precedes Systolic Hypertension in Diet-induced Obesity", *Hypertension* **2013**, *62*, 1105–1110.

[140] N. Sadekova, D. Vallerand, E. Guevara, et al., "Carotid Calcification in Mice: A New Model to Study the Effects of Arterial Stiffness on the Brain", *Journal of the American Heart Association* **2013**, *2*, e000224.

[141] R. D. Terry, P. Davies, "Dementia of the Alzheimer type", *Annual review of neuroscience* **1980**, *3*, 77–95.

[142] I Grundke-Iqbal, J Fleming, Y.-C. Tung, et al., "Ferritin is a component of the neuritic (senile) plaque in Alzheimer dementia", *Acta neuropathologica* **1990**, *81*, 105–110.

[143] J. M. Bland, D. G. Altman, et al., "Statistical methods for assessing agreement between two methods of clinical measurement", *The Lancet* **1986**, *1*, 307–310.

[144] M. Bachler, C. Mayer, B. Hametner, et al., *Online and Offline Determination of QT and PR Interval and QRS Duration in Electrocardiography*, Springer Berlin Heidelberg, **2013**, pp. 1–15.

[145] C. R. Vázquez-Seisdedos, J. E. Neto, E. J. Marañón Reyes, et al., "New approach for T-wave end detection on electrocardiogram: Performance in noisy conditions", *BioMedical Engineering OnLine* **2011**, *10*, 77.

[146] J. M. Bland, D. G. Altman, "Comparing methods of measurement: why plotting difference against standard method is misleading", *The lancet* **1995**, *346*, 1085–1087.

[147] E. Whitley, J. Ball, "Statistics review 6: Nonparametric methods", *Critical Care* **2002**, *6*, 509–513.

[148] C. J Armitage, M. Conner, "Efficacy of the theory of planned behaviour: A meta-analytic review", *British journal of social psychology* **2001**, *40*, 471–499.

[149] W. J. Conover, R. L. Iman, "Rank transformations as a bridge between parametric and nonparametric statistics", *The American Statistician* **1981**, *35*, 124–129.

[150] I. S. Pearsall, "Paper 2: The Velocity of Water Hammer Waves", **1965**, *180*, 12–20.

[151] A. W. Khir, A. O'Brien, G. J. S. R., et al., "Determination of wave speed and wave separation in the arteries", *Journal of Biomechanics* **2001**, *34*, 1145 –1155.

[152] A. W. Khir, A Zambanini, K. H. Parker, "Local and regional wave speed in the aorta: effects of arterial occlusion", *Medical Engineering & Physics* **2004**, *26*, 23 –29.

[153] A. W. Khir, M. J. P. Swalen, J Feng, et al., "Simultaneous determination of wave speed and arrival time of reflected waves using the pressure-velocity loop", *Medical & biological engineering & computing* **2007**, *45*, 1201–1210.

[154] N. Di Lascio, C. Kusmic, F. Stea, et al., "Ultrasound-based Pulse Wave Velocity Evaluation in Mice", **2017**, e54362.

[155] K. H. Parker, "An introduction to wave intensity analysis", *Medical & Biological Engineering & Computing* **2009**, *47*, 175.

[156] J. P. Murgo, N. Westerhof, J. P. Giolma, et al., "Aortic input impedance in normal man: relationship to pressure wave forms.", *Circulation* **1980**, *62*, 105–116.

[157] P. Boutouyrie, S. Laurent, A. Benetos, et al., "Opposing effects of ageing on distal and proximal large arteries in hypertensives.", *Journal of hypertension. Supplement: official journal of the International Society of Hypertension* **1992**, *10*, S87–91.

[158] E. B. Schroeder, L. E. Chambless, D. Liao, et al., "Diabetes, Glucose, Insulin, and Heart Rate Variability", *Diabetes Care* **2005**, *28*, 668–674.

[159] A. C. da Costa Goncalves, J. Tank, A. Diedrich, et al., "Diabetic hypertensive leptin receptor–deficient db/db mice develop cardioregulatory autonomic dysfunction", *Hypertension* **2009**, *53*, 387–392.

[160] S. Park, B. J. Bivona, Y. Feng, et al., "Intact renal afferent arteriolar autoregulatory responsiveness in db/db mice", *American Journal of Physiology - Renal Physiology* **2008**, *295*, F1504–F1511.

[161] C. L. Stables, D. S. Auerbach, S. E. Whitesall, et al., "Differential Impact of Type-1 and Type-2 Diabetes on Control of Heart Rate in Mice", *Autonomic neuroscience: basic & clinical* **2015**, *194*, 17–25.

[162] W. Su, Z. Guo, D. C. Randall, et al., "Hypertension and disrupted blood pressure circadian rhythm in type 2 diabetic db/db mice", *American Journal of Physiology-Heart and Circulatory Physiology* **2008**, *295*, H1634–H1641.

[163] W. Q. Lindh, M. Pooler, C. D. Tamparo, et al., *Delmar's Comprehensive Medical Assisting: Administrative and Clinical Competencies*, Cengage Learning, **2009**.

[164] D. Ogilvie, R. Stinson, "The effect of age on temperature selection by laboratory mice (Mus musculus)", *Canadian Journal of Zoology* **1966**, *44*, 511–517.

[165] M. Talan, "Body temperature of C57BL/6J mice with age", *Experimental gerontology* **1984**, *19*, 25–29.

[166] G. P. Kenny, R. J. Sigal, R. McGinn, "Body temperature regulation in diabetes", *Temperature: Multidisciplinary Biomedical Journal* **2015**, *3*, 119–145.

[167] R. de Oliveira Alvim, P. C.J. L. Santos, M. M. Musso, et al., "Impact of diabetes mellitus on arterial stiffness in a representative sample of an urban Brazilian population", *Diabetology & Metabolic Syndrome* **2013**, *5*, 45–45.

[168] D. J. Penny, J. P. Mynard, J. J. Smolich, "Aortic Wave Intensity Analysis of Ventricular-Vascular Interaction During Incremental Dobutamine Infusion in Adult Sheep", *Heart Lung and Circulation* **2007**, *16*, S170.

[169] N. Ohte, H. Narita, M. Sugawara, et al., "Clinical usefulness of carotid arterial wave intensity in assessing left ventricular systolic and early diastolic performance", *Heart and Vessels* **2003**, *18*, 107–111.

[170] R. R Townsend, "Arterial stiffness: recommendations and standardization", *Pulse* **2016**, *4*, 3–7.

[171] A. D Hughes, C. Park, J. Davies, et al., "Limitations of augmentation index in the assessment of wave reflection in normotensive healthy individuals", *PLOS ONE* **2013**, *8*, e59371.

[172] M. Sakurai, T. Yamakado, H. Kurachi, et al., "The relationship between aortic augmentation index and pulse wave velocity: an invasive study", *Journal of hypertension* **2007**, *25*, 391–397.

[173] F. Fantin, A. Mattocks, C. J. Bulpitt, et al., "Is augmentation index a good measure of vascular stiffness in the elderly?", *Age and ageing* **2006**, *36*, 43–48.

[174] L.-T. Cheng, L.-J. Tang, L. Cheng, et al., "Limitation of the augmentation index for evaluating arterial stiffness", *Hypertension Research* **2007**, *30*, 713.